Microtraps and Waveguides for Bose-Einstein Condensates

by

Aaron E. Leanhardt

Submitted to the Department of Physics
in partial fulfillment of the requirements for the degree of

Doctor of Philosophy

at the

MASSACHUSETTS INSTITUTE OF TECHNOLOGY

September 2003

Author .....
Department of Physics
August 29, 2003

Certified by .....
David E. Pritchard
Cecil and Ida Green Professor of Physics
Thesis Supervisor

Certified by .....
Wolfgang Ketterle
John D. MacAurthur Professor of Physics
Thesis Supervisor

Accepted by .....
Thomas J. Greytak
Professor of Physics, Associate Department Head for Education

Microtraps and Waveguides for Bose-Einstein Condensates

by

Aaron E. Leanhardt

Submitted to the Department of Physics
on August 29, 2003, in partial fulfillment of the
requirements for the degree of
Doctor of Philosophy

Abstract

Gaseous Bose-Einstein condensates containing up to 3×10^6 ^{23}Na atoms were loaded into magnetic microtraps and waveguides on a microfabricated "atom chip" using optical tweezers. Single-mode propagation was observed along the waveguide. Closer to the microfabricated surface, perturbations to the waveguide potential spatially modulated the condensate density. The condensate lifetime was ≥ 20 s and independent of the atom-surface separation, for separations ≥ 70 μm.

Condensates were coherently split by deforming an optical single-well potential into a double-well potential. The relative phase between the two resulting condensates was determined from the matter wave interference pattern formed upon releasing the atoms from the separated potential wells. Coherent phase evolution was observed for condensates held separated by 13 μm for ≤ 5 ms and was controlled by applying AC Stark shifts to either condensate. This demonstrated a trapped-atom interferometer.

Vortices and spin textures were imprinted in spinor condensates using topological phases. The order parameter of condensates held in a Ioffe-Pritchard magnetic trap was manipulated by adiabatically varying the magnetic bias field along the trap axis. Fully inverting the axial bias field imprinted vortices in $F = 1$ and $F = 2$ condensates with $2\hbar$ and $4\hbar$ of angular momentum per particle, respectively. Reducing the axial bias field to zero distributed the condensate population across its $2F + 1$ spin states, each with a different phase winding, and created a spin texture.

Partially condensed atomic vapors were confined by a combination of gravitational and magnetic forces. They were adiabatically decompressed, by weakening the gravito-magnetic trap to a mean frequency of 1 Hz, then evaporatively reduced in size to 2500 atoms. This lowered the peak condensate density to 5×10^{10} atoms/cm^3 and cooled the entire cloud in all three dimensions to a kinetic temperature of 450 ± 80 pK.

Thesis Supervisor: David E. Pritchard
Title: Cecil and Ida Green Professor of Physics

Thesis Supervisor: Wolfgang Ketterle
Title: John D. MacAurthur Professor of Physics

To my family,

Dale, Sharon, and Wendi

Acknowledgments

An African proverb states that *it takes a whole village to raise a child*. It has been my experience that earning a Ph.D. requires a similar level of support. While it is inevitable that only my name will appear on this thesis and the corresponding doctorate degree, I would like to acknowledge several important contributions to my growth and development as a physicist, my experiences in the laboratory, and my general survival at MIT.

Dave Pritchard and Wolfgang Ketterle deserve far more than the traditional obligatory "thanks" given to most thesis supervisors. Dave always found ways to challenge me, and while the warmth with which I accepted the challenges varied wildly, I certainly benefited from facing each one. Wolfgang always found ways to encourage me, even in the midst of my many failures. In general, I would like to thank Dave and Wolfgang for allowing me to explore ideas that often led the lab astray, or at least off the beaten path, but in the end helped to develop my physical intuition.

I owe much gratitude to the people ahead of me in the lab. In particular, I thank Axel Görlitz for teaching me the ways of MIT's original Bose-Einstein condensation (BEC) apparatus, the nuances of dye lasers, and quite generally how to be a physicist. However, all of the work in this thesis was performed on MIT's third generation BEC apparatus, a.k.a. *the science chamber*. Todd Gustavson, Ananth Chikkatur, Axel Görlitz, and Deep Gupta were instrumental in making the science chamber a reality, without which much of this thesis would not exist. I am indebted to Todd for his attention to detail, Ananth for his upbeat leadership, and Deep for his laid-back mentoring.

More recently, it has been a privilege to work with Yong-Il Shin, Tom Pasquini, Michele Saba, and Andre Schirotzek. All of the experiments described in this thesis were performed in collaboration with Yong. He has been both a selfless wingman and a determined leader. I thank him for supporting my ideas (as random as they were) and teaching me his own. Tom has been a wonderful officemate with whom I have enjoyed many spontaneous discussions, Michele's contributions to the lab make me

wish he had become our post-doc two years earlier, and Andre has brought enthusiasm to our late night data runs. Collectively, I thank Yong, Tom, Michele, and Andre for being great labmates and scientific companions.

MIT's atomic physics program certainly has strength in numbers. Over the years I have greatly benefited from interactions with James Anglin, Micah Boyd, Gretchen Campbell, Zoran Hadzibabic, Shin Inouye, Dan Kleppner, Roberto Onofrio, Chandra Raman, Till Rosenband, Dominik Schneble, Dan Stamper-Kurn, Johnny Vogels, Kaiwen Xu, and Martin Zwierlein.

Lab productivity would have been greatly reduced without the aid of Mara Prentiss, Mukund Vengalattore, and MIT's Microsystems Technology Laboratories, who helped our research group enter the field of miniaturized atom optics, Edem Tsikata, who provided experimental assistance and supported our lab infrastructure, and Carol Costa, who handled our administrative needs.

While laboratory research is all that is included in this thesis, it is far from all that is required to graduate. My early years at MIT were filled with coarse work and exams, none of which I could have survived without the help and tutelage of Jamil Abo-Shaeer, Lia Matos, and Kendra Vant. Jamil's "yo-man" attitude, Lia's ability to rewrite any equation in terms of a complex plane integral that I could not evaluate, and Kendra's meticulous organization helped to keep me sane, humble, and on-track at a time when I needed it most.

Jamil has been a true friend and confidante ever since I arrived at MIT, and I will continue to seek his advice even after we go our separate ways. His unwavering support inside and outside of lab has been invaluable. Together, he and Kate DuBose have been caring and generous roommates.

I would not be a physicist today without the guidance that I received while an undergraduate at the University of Michigan from Jean Krisch, Dave Gidley, and Rich Vallery.

Finally, I thank my father Dale, my late mother Sharon, and my sister Wendi for providing me with inspiration. Rather than trying to describe the totality of their contributions to my life, I simply dedicate my work at MIT to them.

Contents

List of Figures

Chapter 1

Introduction

The phenomenon of Bose-Einstein condensation (BEC) underlies our understanding of superfluid liquid helium and superconducting electron pairs. However, the strength and complexity of particle-particle interactions in these systems makes controlling, manipulating, and characterizing their condensate phases difficult. It was only after 1995, when the BEC phase transition was observed in dilute atomic vapors [40, 110], that many fundamental properties of Bose-Einstein condensates were addressed.

In the following years, the field of quantum degenerate gases has grown to include eight species of atomic Bose-Einstein condensates, ^{87}Rb [6], ^{23}Na [46], ^{7}Li [21, 22], ^{1}H [63], ^{85}Rb [41], ^{4}He* [167, 182], ^{41}K [151], ^{133}Cs [217], and ^{174}Yb [207] and two species of quantum degenerate Fermi gases, ^{40}K [48] and ^{6}Li [213]. The field developed experimentally and theoretically in parallel, with theoretical predictions leading to experimental discovery and experimental observations producing theoretical understanding equally often. Much of this development can be found in the multitude of review articles, conference proceedings, and textbooks currently available, of which Refs. [42, 94, 128, 166, 169] are a small subset.

This chapter introduces the concept of Bose-Einstein condensation as relevant for the experiments presented in this thesis. For clarity, the presentation assumes a three-dimensional gas in thermal equilibrium.

1.1 BEC Phase Transition

The Bose-Einstein condensation phase transition corresponds to a macroscopic occupation of the quantum mechanical ground state of the system[1]. For N particles at a temperature T, the critical point for condensation corresponds to all thermally accessible being occupied, i.e. the number of quantum states with energy $E \leq k_B T$ equals the number of particles in the system, where k_B is Boltzmann's constant. At the critical point, the gas is referred to as a quantum saturated thermal vapor.

An alternative, but equivalent, description of the BEC phase transition can be given in terms of matter wave overlap. For a gas at number density[2] n, matter wave overlap occurs when the interparticle spacing, $n^{-1/3}$, equals the thermal deBroglie wavelength, λ_T, of the atoms. At this point the atoms lose their individual identities and begin to behave as a unified ensemble. This criteria can be written as $n\lambda_T^3 \approx 1$, where $n\lambda_T^3$ is the phase space density of the gas[3]. Thus, the BEC phase transition occurs at a phase space density near unity meaning that all thermally accessible states are occupied.

Once all thermally accessible states are occupied, adding more particles to the ensemble results in a macroscopic occupation of the ground state (according to Bose statistics) and Bose-Einstein condensation. Thus, a gas cooled below the BEC phase transition temperature consists of two components: a thermal (normal) fraction that occupies many quantum states and a condensed (superfluid) fraction that occupies a single quantum state.

The number of thermally accessible states below a given temperature depends on the excitation spectrum of the system. Free particles have a continuum of excitation energies $\epsilon(p) = p^2/2m$, where p and m are the momentum and mass of the particles, respectively. Confinement modifies the excitation spectrum. The experiments de-

[1] More generally, the BEC phase transition can be thought of as the macroscopic occupation of a single quantum state, often occurring in long-lived metastable states rather than the absolute ground state of the system.

[2] All densities described in this thesis are number densities, not mass densities.

[3] A phase space cell has position and momentum dimensions $\Delta q = n^{-1/3}$ and $\Delta p = h/\lambda_T$, respectively. The normalized volume of such a cell is $(\Delta q \Delta p/h)^3 = 1/n\lambda_T^3$, where h is Planck's constant.

scribed in this thesis were performed with harmonically trapped atoms. Such particles have excitation energies $\epsilon(n_x, n_y, n_z) = (n_x+1/2)\hbar\omega_x+(n_y+1/2)\hbar\omega_y+(n_z+1/2)\hbar\omega_z$, where ω_x, ω_y, and ω_z are the trap frequencies and $\hbar = h/2\pi$.

The density, n_{th}, or number, N_{th}, of thermally excited atoms is found by integrating or summing the Bose-Einstein distribution,

$$\langle n(\epsilon)\rangle = \frac{1}{e^{(\epsilon-\mu)/k_BT}-1}, \tag{1.1}$$

where $\langle n(\epsilon)\rangle$ gives the number of particles occupying a state of energy ϵ such that $N = \int d\epsilon\langle n(\epsilon)\rangle$, ϵ is the appropriate excitation spectrum, and μ is the chemical potential of the gas. For free particles this results in

$$n_{th} = \zeta(3/2)\frac{\sqrt{2\pi m k_B T}}{h} \Rightarrow k_B T_c = \frac{h^2}{2\pi m}\left(\frac{n}{\zeta(3/2)}\right)^{2/3}, \tag{1.2}$$

where T_c is the BEC phase transition temperature and $\zeta(3/2) \approx 2.612$ is the Riemann Zeta function.

Likewise, for harmonically confined atoms

$$N_{th} = \zeta(3)\left(\frac{k_B T}{\hbar\bar{\omega}}\right)^3 \Rightarrow k_B T_c = \hbar\bar{\omega}\left(\frac{N}{\zeta(3)}\right)^{1/3}, \tag{1.3}$$

where $\zeta(3) \approx 1.202$ and $\bar{\omega} = (\omega_x\omega_y\omega_z)^{1/3}$. Typical experimental parameters fall in the range $10^4 < N < 10^7$ and 1 Hz $< \bar{\omega}/2\pi <$ 100 Hz such that 1 nK $< T_c <$ 1 μK and 10^{11} atoms/cm^3 $< n < 10^{15}$ atoms/cm^3.

1.2 Macroscopic Order Parameter

The above discussion was for an ideal (non-interacting) Bose gas. Atom-atom interactions are essential for thermalization and efficient cooling to quantum degeneracy. They are manifestly present under typical experimental conditions. While such interactions shift the BEC phase transition temperature by only a few percent, they typically dominant the ground state properties of the condensate.

1.2.1 Density Distribution

The $N_0 = N - N_{th}$ atoms in the condensate are all described by a single order parameter (wavefunction), $\Psi(\vec{r},t)$, that represents the ground state of the many-body system. The usual Schrödinger equation is modified to include a nonlinear term that accounts for atom-atom interactions, and $\psi(\vec{r})$ is an eigenstate of the resulting Gross-Pitaevskii equation,

$$\left(-\frac{\hbar^2}{2m}\nabla^2 + V(\vec{r}) + \frac{4\pi\hbar^2 a}{m}|\psi(\vec{r})|^2\right)\psi(\vec{r}) = \mu\psi(\vec{r}), \tag{1.4}$$

where $V(\vec{r})$ is the external potential, a is the s-wave scattering length for a binary collision, and the time evolution of the wavefunction is given by the chemical potential, $\Psi(\vec{r},t) = \psi(\vec{r})e^{-i(\mu/\hbar)t}$.

In the Thomas-Fermi limit, the atom-atom interaction energy dominates the kinetic energy $[(-\hbar^2/2m)\nabla^2\psi(\vec{r})]$ associated with the condensate wavefunction, and the ground state condensate density is

$$n(\vec{r}) = |\psi(\vec{r})|^2 = \frac{m}{4\pi\hbar^2 a}[\mu - V(\vec{r})]. \tag{1.5}$$

Since the chemical potential is a constant throughout the gas, the condensate wavefunction has the inverted shape of the trapping potential. For harmonically confined atoms $V(\vec{r}) = (1/2)m(\omega_x x^2 + \omega_y y^2 + \omega_z z^2)$, and the chemical potential can be expressed as

$$\mu = \frac{1}{2}\hbar\bar{\omega}\left(15N\frac{a}{a_{HO}}\right)^{2/5}, \tag{1.6}$$

$$= \frac{1}{2}m\omega_i^2 R_i^2, \tag{1.7}$$

where $a_{HO} = \sqrt{\hbar/m\bar{\omega}}$ and R_i is the Thomas-Fermi size of the condensate along the $i = x, y, z$ axis.

More generally, taking the trap center to be the zero of energy, the chemical potential can be expressed as $\mu = (4\pi\hbar^2 a/m)n_0$, where n_0 is the condensate density

at the trap center. The local mean field interaction energy is often referred to a the local chemical potential and is written as $\mu(\vec{r}) = (4\pi\hbar^2 a/m)n(\vec{r})$. For ^{23}Na atoms in the $|F = 1, m_F = -1\rangle$ state, $a \approx 53a_0 \approx 2.8$ nm, where a_0 is the Bohr radius[4]. Thus, $\mu \approx k_B \times 66 \times 10^{-14}$ nK-cm^3 $\approx h \times 1.4 \times 10^{-14}$ kHz-cm^3.

Briefly a word about energy units. Throughout this thesis energy will be quoted in temperature, frequency, and occasionally magnetic field units. The conversions are $k_B \times 1\ \mu$K $\approx h \times 21$ kHz $\approx (\mu_B/2) \times 30$ mG, where 1 G $= 10^{-4}$ T, μ_B is the Bohr magneton, and atoms in the $|1, -1\rangle$ state have a magnetic moment of $\mu_B/2$.

The treatment presented in this section is valid provided the gas is sufficiently dilute, $na^3 \ll 1$, which is satisfied in all of the experiments presented in this thesis. Two important energy scales for partially condensed atomic vapors are the thermal kinetic energy (temperature) and chemical potential of the sample. Quite generally, $\mu/k_B T_c \propto (na^3)^x$ where $x = 1/3$ for free particles and $x = 1/6$ for harmonically confined atoms in the Thomas-Fermi limit. Thus, the mean field interaction energy experienced by atoms in the condensate fraction is typically less than the kinetic energy of atoms in the thermal fraction.

1.2.2 Phase Coherence

The condensate order parameter can be written in terms of an amplitude and phase, $\psi(\vec{r}) = \sqrt{n(\vec{r})}e^{iS(\vec{r})}$. Associating a single phase with the condensate gives rise to its laser-like coherence [9, 25, 107, 113] and superfluid [133, 134, 210] properties. These phase coherence properties can be destroyed in very anisotropic systems at finite temperature [50, 83, 181] and in the presence of potential corrugations such as optical lattices [70, 164], where localized regions of the gas have independent phases. However, the experiments described in this thesis were performed in a regime where a single phase accurately described the condensate.

[4]For ^{23}Na atoms in the $|F = 2, m_F = +2\rangle$ state, $a \approx 63a_0 \approx 3.3$ nm. In general, a can be tuned with an externally applied magnetic field at a Feshbach resonance [95]. The values quoted for a are those far from any such resonance.

1.3 Contributions and Collaborations

My first two years at MIT were divided between contributing to the construction of a new BEC apparatus[5] and collaborating on experiments running on an existing one. Aside for the usual gamut of tasks given to the youngest graduate student (electronics assembly, computer programming, etc...), my main contribution to the new BEC apparatus was designing and building a Ioffe-Pritchard, cloverleaf style magnetic trap [68, 147, 174]. In parallel, I was given the opportunity to collaborate on two experiments performed on MIT's original BEC apparatus. The first realized Bose-Einstein condensates in lower dimensions [67], and the second transferred sodium condensates between the lower ($F = 1$) and upper ($F = 2$) hyperfine levels [66].

While these construction and experimental efforts were invaluable in teaching me the methods of atom cooling and condensate manipulation, they will not be described in any detail in this thesis. Instead, I will focus on the scientific results produced in my final two years at MIT. The title *Microtraps and Waveguides for Bose-Einstein Condensates* reflects an ongoing effort in the lab to design and implement new devices to confine and manipulate Bose-Einstein condensates, and much of the work presented in this thesis reflects that effort. In addition, the phase coherence properties of the condensate are emphasized with respect to atom interferometry and superfluidity.

Appendices A-F contain reprints of publications covering the main achievements of my graduate work. This thesis aims to motivate, contextualize, summarize, and supplement the content of these publications. General results and trends will be emphasized and discussed based on the current state of the field.

1.4 Outline

Sodium condensates were produced by a novel BEC apparatus described in Ch. 2, without which many of the following experiments would not have been possible. This includes the trapping and guiding of condensates with magnetic potentials generated by microfabricated current-carrying wires described in Ch. 3. A major long term

[5]This was MIT's third BEC apparatus and would become known as *the science chamber* (Ch. 2).

goal of this effort is to build a trapped-atom interferometer. To this end, we identified several limitations of magnetic microtraps and worked in parallel to develop such an interferometer using optical potentials. Chapter 4 reports on the successful demonstration of trapped-atom interferometry in an optical double-well potential. Chapter 5 delves into the superfluid nature of Bose-Einstein condensates and describes vortices and spin textures imprinted onto the condensate wavefunction using topological phases. Chapters 4 and 5 are complementary in the sense that Ch. 4 demonstrates our ability to write and read uniform condensate phases, while in Ch. 5 we imprint and detect phase windings. Finally, Ch. 6 describes the cooling of partially condensed atomic vapors to picokelvin temperatures at peak densities $< 10^{11}$ atoms/cm^3. Such low temperature and low density samples are important for spectroscopy, metrology, and atom optics. Some concluding remarks and perspective are included in Ch. 7. Appendices A-F include publications directly related to the chapters of this thesis.

Chapter 2

Bose-Einstein Condensate Production and Transport

All of the experiments described in this thesis were performed on MIT's third generation sodium BEC apparatus, BEC-III, commonly referred to as *the science chamber* for reasons that will be made obvious below. The apparatus is described briefly in Ref. [74] and thoroughly in Ref. [33]. The aim of this chapter is to fall somewhere in between.

2.1 The Science Chamber Apparatus

The design goal for this novel apparatus was to separate the job of producing condensates from the task of studying them. In short, we wanted to create a condensate beamline such that every $20 - 30$ s a fresh condensate would be delivered to an experimental platform for examination. Figure 2-1 shows our realization of this goal.

2.1.1 Condensate Production

A thermal atomic beam escapes through a 4 mm aperture in an effusive oven containing liquid sodium heated to 260 C. The atomic beam is slowed by radiation pressure in a spin-flip Zeeman slower to a mean velocity ~ 30 m/s. The slow atom flux exiting

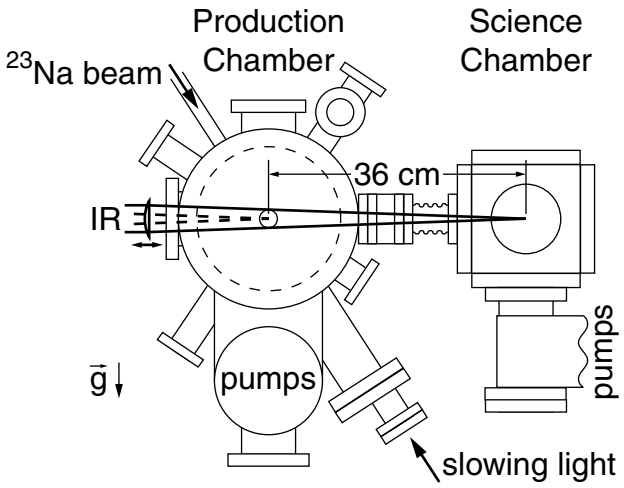

Figure 2-1: The science chamber apparatus. Gaseous Bose-Einstein condensates of sodium atoms are created through a combination of laser and evaporative cooling in the production chamber. Subsequently, they are captured in the focus of an infrared (IR) optical tweezers beam and transported into the auxiliary science chamber. The acceleration due to gravity, $\vec{g}$, points down the page. Drawn to scale.

the Zeeman slower is $\sim 10^{11}$ atoms/s. The circularly polarized slowing laser beam contains ~ 50 mW of power and is tuned 1000 MHz below the $F = 2 \rightarrow F' = 3$ cycling transition (Fig. 2-2). 10% of the slowing laser power is transferred into repumping sidebands near the $F = 1 \rightarrow F' = 2$ transition by an electro-optic modulator (EOM) driven near[1] 1743 MHz. The Zeeman slower consists of three separately powered tapered solenoids running currents between 16 A and 105 A and produces magnetic fields up to 700 G.

The slowed atomic beam is continuously loaded into a dark spontaneous force optical trap (dark-SPOT [111]) type magneto-optical trap (MOT [177]) for 1 s. The MOT consists of a spherical quadrupole magnetic field with a maximum gradient of 11 G/cm and three orthogonal pairs of counter propagating laser beams detuned 20 MHz below the $F = 2 \rightarrow F' = 3$ cycling transition. The total power in all six MOT beams is ~ 100 mW. A ~ 25 mW repumping beam resonant with the $F = 1 \rightarrow F' = 2$

[1]Empirically, this frequency can be varied over tens of megahertz without degrading the Zeeman slower performance. This is because the magnetic field profile of the Zeeman slower is designed to keep the $F = 2 \rightarrow F' = 3$ cycling transition on resonance, but not the $F = 1 \rightarrow F' = 2$ repumping transition.

transition is applied to the edge of the cloud such that the atoms in the center of the MOT remain in the (dark) $F = 1$ state, while the hotter atoms near the edge are cooled and transferred into the central $F = 1$ cloud.

Weak field seeking $|F = 1, m_F = -1\rangle$ atoms cooled by the MOT to ~ 100 μK are loaded into a Ioffe-Pritchard, cloverleaf style magnetic trap [68, 147, 174]. No intermediate sub-doppler cooling is performed although some polarization gradient cooling takes place in the MOT itself[2]. One half of the magnetic trap is shown in Ch. 3, Fig. 3-1(a). The two halves are identical and mounted outside the ultrahigh vacuum chamber, symmetrically about the atoms. The trapping coils generate an axial magnetic field curvature of 1 G/cm^2/A and a radial magnetic field gradient of 0.6 G/cm/A. The magnetic trap runs currents between 200 A and 500 A and dissipates 15 kW of power. Typical trapping parameters are an axial bias field of 1.4 G and axial and radial trap frequencies $\omega_{||} = 2\pi \times 20$ Hz and $\omega_{\perp} = 2\pi \times 200$ Hz, respectively.

Forced radio frequency evaporation is used to cool the magnetically trapped atoms to Bose-Einstein condensation. The radio frequency drive uses ~ 1 W of power and its frequency[3] is ramped from 30 MHz to ~ 1 MHz in 20 s. This procedure produces Bose-Einstein condensates containing $> 10^7$ atoms.

2.1.2 Condensate Transport

After production, the condensates are loaded into the focus of an optical tweezers laser beam. The optical tweezers consist of a 1064 nm laser focused to a $1/e^2$ radius of 26 μm, such that ~ 50 mW of power produces axial and radial trap frequencies $\omega_{||} = 2\pi \times 4$ Hz and $\omega_{\perp} = 2\pi \times 440$ Hz, respectively, and a trap depth of $k_B \times 3$ μK. The focus is generated by passing a collimated beam through a 50 mm diameter, 500 mm focal length lens mounted on an air bearing translation stage. Translating this lens moves the position of the focus and hence the atoms as well. Using the optical tweezers, condensates are transported ~ 36 cm in 2 s into an auxiliary "science"

[2]For ^{23}Na, the doppler cooling limit is $T_D = 240$ μK.
[3]1 MHz corresponds to a 1.4 G magnetic field.

chamber. Upon arrival in the science chamber the condensates contain up to 3×10^6 atoms.

The optical power for the tweezers beam is raised by a factor of $5 - 10$ during translation to prevent atom loss, but it is lowered again as the atoms near their final destination. The $1/e$ lifetime of condensates in the optical tweezers is 20 s. This is most likely limited by vibrations, since the background vapor pressure ($\sim 10^{-11}$ torr) and photon scattering rate (0.01 Hz) are sufficiently low not to cause problems.

The condensate production chamber and the science chamber are separated by a gate value. This allows for the science chamber to be vented and reconfigured while maintaining ultrahigh vacuum in the condensate production region. In addition, the science chamber is free from the many constraints of producing a condensate (laser cooling optics, Zeeman slower, magnetic trap, etc...) and thus has better experimental access than the production chamber. Since the first condensates arrived in the science chamber two years ago, we have used this flexibility to demonstrate miniaturized magnetic traps [74], a continuous source of Bose-Einstein condensed atoms [35], microfabricated magnetic traps and waveguides [122, 126], topological defects such as vortices [123] and spin textures [126], a trapped-atom interferometer [199], and a weakly confining gravito-magnetic trap with picokelvin temperature condensates [124].

2.2 Magnetic and Optical Confinement

^{23}Na has a $3S_{1/2}$ ground state with $F = 1$ and $F = 2$ hyperfine levels (Fig. 2-2). At low magnetic fields ($|\vec{B}| < 100$ G), F and m_F are good quantum numbers and the atomic states can be described in a basis $|F, m_F\rangle$. The interaction energy of these states with a magnetic field is

$$V_B = g_F m_F \mu_B |\vec{B}|, \tag{2.1}$$

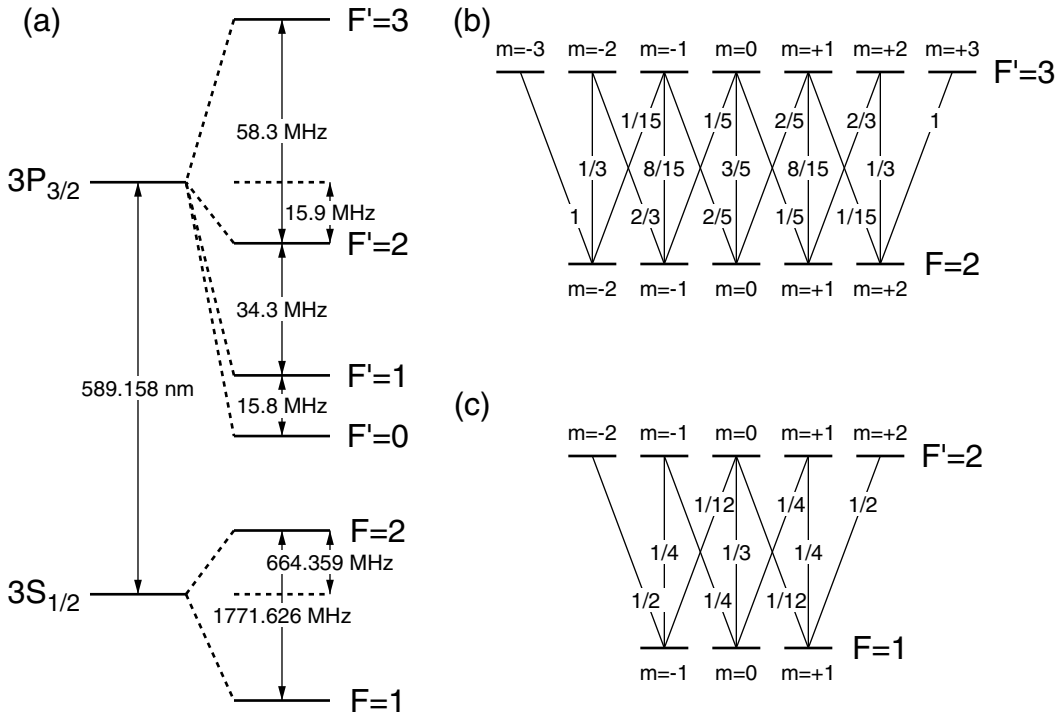

Figure 2-2: ^{23}Na energy levels. (a) The D_2 line used for laser cooling and optical imaging. Relative strength of the (b) $F = 2 \rightarrow F' = 3$ and (c) $F = 1 \rightarrow F' = 2$ electric dipole transitions [146].

where g_F is the Landé g-factor, μ_B is the Bohr magneton, and the direction of $\vec{B}$ has been taken as the quantization axis. For ^{23}Na, $g_{F=1} = -1/2$ and $g_{F=2} = 1/2$.

Since Maxwell's equations allow (prohibit) magnetic field minima (maxima) in free space, only the weak field seeking states $|1, -1\rangle$, $|2, +1\rangle$, and $|2, +2\rangle$ can be magnetically trapped [148][4]. Their magnetic moments are $\mu_B/2$, $\mu_B/2$, and μ_B, respectively.

In contrast, all spin states may be optically confined and experience the same

[4]Spin exchange collisions between atoms in the $|2, +1\rangle$ state severely limit trap lifetimes such that magnetically trapped sodium condensates have been realized in the $|1, -1\rangle$ [46] and $|2, +2\rangle$ [123] states only. In principle, atoms in the $|2, 0\rangle$ can be magnetically trapped due to the quadratic Zeeman effect. However, they would also suffer from inelastic spin exchange collisions.

trapping potential[5,6]. The interaction of a two-level atom with an optical field of intensity $I(\vec{r})$ and frequency ω can be described by the optical dipole potential [10, 38]

$$V_{op} = \frac{\hbar\Delta\omega}{2} \ln\left(1 + \frac{I(\vec{r})}{I_s} \frac{(\Gamma/2)^2}{\Delta\omega^2 + (\Gamma/2)^2}\right), \tag{2.2}$$

where $\Delta\omega = \omega - \omega_0$ is the detuning from the atomic resonance of width (FWHM) Γ and I_s is the saturation intensity of the transition. In writing Eq. 2.2, the rotating wave approximation was made and saturation effects were neglected[7]. From Eq. 2.2 it is evident that atoms are attracted to high intensity regions of red-detuned radiation ($\Delta\omega < 0$). Thus, a focused red-detuned laser beam can trap atoms [38]. Conversely, atoms are repealed from high intensity regions of blue-detuned radiation ($\Delta\omega > 0$).

2.3 Optical Imaging

The ^{23}Na D_2 line is used for laser cooling and optical imaging. It has wavelength $\lambda = 589.158$ nm and linewidth (FWHM) $\Gamma = 2\pi \times 10$ MHz. While non-destructive, dispersive imaging is possible, all of the data presented in this thesis was acquired through destructive, absorption imaging. The cross section for scattering photons is maximal on the $F = 2,\ m_F = \pm 2 \rightarrow F' = 3,\ m'_F = \pm 3$ cycling transitions and has the value $\sigma_0 = 3\lambda^2/2\pi$ on resonance. The relative scattering cross sections for other transitions are displayed in Figs. 2-2(b) and 2-2(c).

Absorption imaging of condensates in the $F = 1$ ($F = 2$) hyperfine level is performed on the $F = 1 \rightarrow F' = 2$ ($F = 2 \rightarrow F' = 3$) electric dipole transition. Condensates in the $F = 1$ hyperfine level may be optically pumped into the $F = 2$ hyperfine level and subsequently imaged on the $F = 2 \rightarrow F' = 3$ transition. The absorption imaging process integrates the atomic density along the axis of the probe

[5]Spin exchange collisions between atoms in the $|F = 2, m_F = +1, 0, -1\rangle$ states severely limit trap lifetimes such that optically confined sodium condensates have been realized in the $|F = 1, m_F = +1, 0, -1\rangle$ [202], $|2, -2\rangle$ [66], and $|2, +2\rangle$ [123] states only.

[6]For laser detunings large compared to the fine structure splitting of the electronic excited state, the multi-level nature of the atom and the polarization of the light field are unimportant.

[7]For the optical tweezers described above, the counter-rotating term contributes an additional 30% to the trap depth in Eq. 2.2 [74, 202].

beam allowing only the column density of the cloud to be extracted [112]. Spatial images are focused onto a CCD camera using pairs of lenses. The effective pixel size of the camera is typically ≥ 3 μm, and condensate dimensions during the imaging process range from a few microns to a few millimeters.

Trapped condensates often contain features too small to be optically resolved. Suddenly switching off the trapping potential allows the mean field energy, μ, to be converted to kinetic energy, and the condensate wavefunction expands ballistically. For prolate (cigar-shaped) condensates, the expansion is anisotropic with most of the mean field energy transferred into radial kinetic energy [28]. As a result, prolate condensates imaged during ballistic expansion have their radial features magnified by $\sqrt{1+\omega_\perp^2\tau^2}$, where $\omega_\perp$ is the radial frequency of the trap from which they were released and τ is the duration of the ballistic expansion process. This allows for small radial features, such as vortex cores, to be optically imaged. In contrast, negligible axial expansion occurs leading to unit magnification of axial features.

Since $\mu/k_BT_c \ll 1$, when released from the trap the condensate fraction expands slower than the thermal fraction and the two components can be easily distinguished.

Chapter 3

Magnetic Microtraps and Waveguides

The field of atom optics relies on bright sources of matter waves and techniques to coherently manipulate them. Pioneering experiments with thermal atomic beams and vapors have demonstrated precision atom interferometry [73, 219], high resolution atom lithography [142, 209], quantum reflection from material surfaces [3, 14, 198], and strong coupling with microwave and optical cavities [15, 136]. Significant improvements to these experiments may be realized with more coherent atomic wavepackets and advanced control over them. This invites the use of Bose-Einstein condensates, which are well-established as fully coherent ensembles of matter waves [9, 25, 107, 113]. Likewise, microtraps and waveguides have the fine manipulation capabilities necessary to build trapped-atom and guided-atom interferometers, bring atoms near material surfaces for deposition purposes or interaction studies, and couple atoms into high finesse cavities.

To emphasize the power of miniaturization, the two magnetic traps shown in Fig. 3-1 are capable of producing harmonic confining potentials with nearly equal frequencies[1]. However, the macroscopic cloverleaf trap [Fig. 3-1(a)] requires currents ~ 500 A to duplicate the performance of the microfabricated trap [Fig. 3-1(b)] running

[1]The trap depth and trap volume of the macroscopic cloverleaf trap [Fig. 3-1(a)] are substantially larger than those of the microfabricated trap [Fig. 3-1(b)].

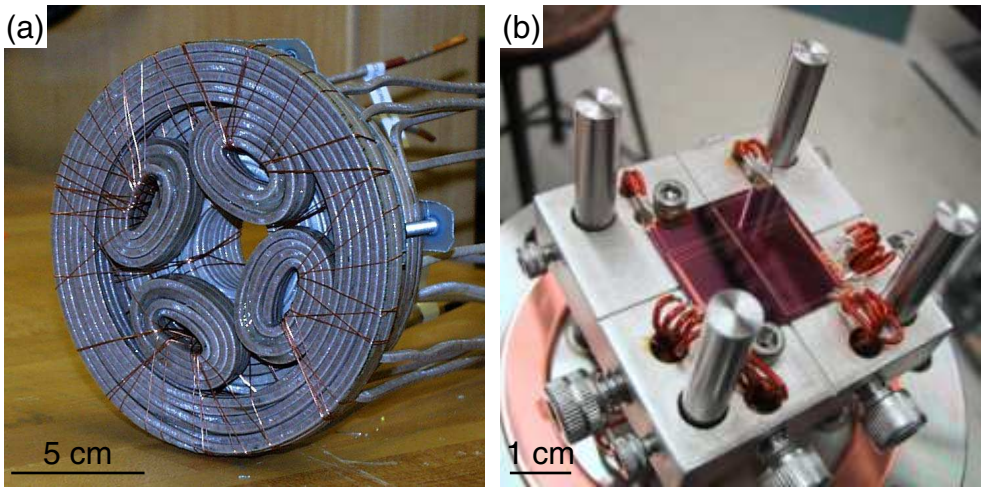

Figure 3-1: (Color) Macroscopic and microscopic magnetic traps. (a) One half of the cloverleaf trap used for condensate production (Ch. 2). (b) Microtrap used for waveguiding (Ch. 3). To produce nearly identical harmonic confinement frequencies, the cloverleaf trap must dissipate $\sim 10,000$ times more power than the microtrap.

$\sim$ 1 A. The difference is that in the microtrap the atoms are only a few hundred microns away from a 50 μm wide current-carrying wire, while in the macroscopic cloverleaf trap they are a few centimeters away from $\sim$ 10 cm diameter coils.

In general terms, given a confining potential with characteristic magnitude V_0 and length scale D, dimensional analysis reveals that the force on an atom in this potential scales as V_0/D. Accordingly, reducing D increases the confinement strength of the potential. For electromagnetic potentials, typically V_0 is proportional to the field generated at the location of the atoms and D is set by the size of the field generating elements or the distance between them and the atoms, whichever is larger. Thus, bringing atoms closer to smaller field generating elements inherently increases the forces acting on them[2]. To date, microtrap frequencies $>$ 1 MHz have been demonstrated [58].

Since the first magnetic microtrap proposal [218], several research groups have been active in the field of miniaturized atom optics (for an overview of the field see Refs. [61, 89, 194, 208]). Thermal clouds have been trapped [60, 81, 180] and

[2]In practice, reducing D also increases V_0 if the power driving the field generating elements is kept constant. This further enhances the confinement strength of the potential.

guided [47, 154, 155] using atom chips[3], and incoherent atomic beam splitters have been demonstrated [27, 156].

The successful union of Bose-Einstein condensates with microfabricated devices [80, 122, 165, 195] represents a significant advance for the field of atom optics. This chapter describes our contributions to this effort and expands on the work presented in Refs. [122] (App. A) and [125] (App. B).

We have demonstrated that Bose-Einstein condensates transported with optical tweezers can be transferred into a magnetic microtrap fabricated on a substrate. Our condensates contained over five times more atoms than other microchip-based experiments [80, 165, 195]. Condensates were released from the microtrap into a single-wire magnetic waveguide and propagated 12 mm before exiting the field of view of our imaging system. The waveguide center was 450 μm below the microfabricated surface.

Single-mode (excitation-less) propagation was observed along homogeneous segments of the waveguide in a regime where the center-of-mass kinetic energy (velocity) of the condensate exceeded its transverse confinement energy (speed of sound). Transverse excitations were created in condensates that propagated through perturbations in the guiding potential. These perturbations resulted from geometric deformations of the current-carrying wires on the substrate.

The behavior of Bose-Einstein condensates near a microfabricated surface was studied for atom-surface separations in the range $70-500$ μm. The condensates were confined at the same position relative to the surface by either a magnetic microtrap or an optical dipole trap. Since the two traps operated on different principles and the electromagnetic fields for each had different sources, this study provided a unique examination of the interaction between Bose-Einstein condensates and a microfabricated surface. For example, while condensates confined near the surface in a magnetic microtrap were found to fragment longitudinally [62, 102, 122], the clouds remained intact under optical confinement. The measured condensate lifetime in either the

[3]The term "atom chip" generally refers to a microfabricated device used to confine and manipulate ultracold atoms.

magnetic microtrap or the optical dipole trap was independent of the atom-surface separation and $\geq$ 20 s, an order of magnitude longer than results reported elsewhere [62, 80, 195]. Radio frequency technical noise was directly observed to drive spin-flip transitions in optically confined condensates near the atom chip. The rate of such transitions increased strongly as the atom-surface separation was reduced.

3.1 Magnetic Micropotentials

Typical magnetic waveguides are cylindrically symmetric, Ioffe-Pritchard style potentials formed by a two-dimensional quadrupole field and a uniform bias field, $B_{||}$, along the guide axis [68, 174]. The two fields add in quadrature to produce a waveguide with harmonic radial confinement at a frequency $\omega_{\perp} \propto B'/\sqrt{B_{||}}$, where B' is the radial magnetic field gradient associated with the two-dimensional quadrupole field. The axial bias field also provides a non-zero magnetic field minimum to prevent non-adiabatic spin-flip transitions (Majorana flops).

The simplest configuration for generating a magnetic waveguide consists of a single microfabricated wire carrying current I and a uniform bias field, $B_{\perp}$, orthogonal to the path of the wire but parallel to the surface of the microchip (Fig. 3-2). The magnetic field due to the wire has magnitude $B_{wire} = \mu_0 I/2\pi r$ that decays with distance, r, from its center, where μ_0 is the permeability of free space. As a result, close to the wire $B_{wire} > B_{\perp}$ but far from the wire $B_{wire} < B_{\perp}$. Directly beneath the wire at $r_0 = \mu_0 I/2\pi B_{\perp}$ the two fields exactly cancel and a two-dimensional quadrupole field is formed along the entire length of the wire. The radial magnetic field gradient associated with the two-dimensional quadrupole field is $B' = B_{\perp}/r_0 = 2\pi B_{\perp}^2/\mu_0 I = \mu_0 I/2\pi r_0^2$.

The equations and scaling arguments presented thus far have assumed a circular wire cross section. However, most microfabricated wires have rectangular cross sections, characterized by a width along the microchip surface, W, and a height perpendicular to the microchip surface, H. The geometry of the wire only becomes relevant for atom-surface separations of order W or H, whichever is larger (Fig. 3-3).

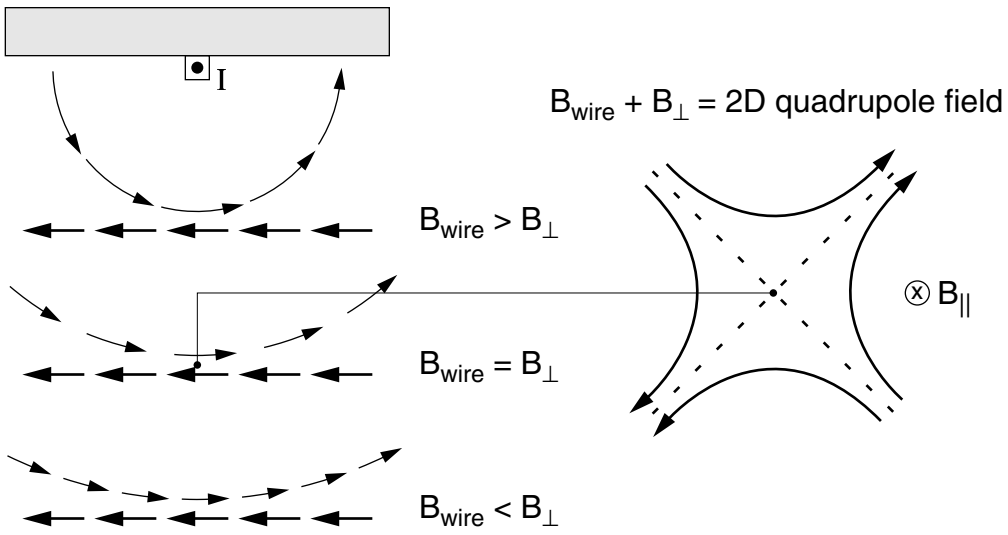

Figure 3-2: Single-wire magnetic waveguide. The magnetic field generated by a microfabricated current-carrying wire, B_{wire} (thin arrows), exactly cancels an externally applied bias field, $B_\perp$ (thick arrows), at one point in space, about which a two-dimensional quadrupole field is formed. This creates a magnetic waveguide. The distance between the waveguide axis and the wire scales as $I/B_\perp$, where I is the current in the wire. An axial bias field, $B_{||}$, is applied parallel/antiparallel to the wire to prevent non-adiabatic spin-flips at the waveguide center and to make the radial confinement harmonic.

A uniform bias field is added along the waveguide axis to create harmonic confinement and prevent non-adiabatic spin-flip transitions as discussed above. To first order, a uniform bias field applied perpendicular to the surface of the microchip (and hence orthogonal to both $B_{||}$ and $B_\perp$) shifts the waveguide axis in a plane parallel to the surface of the microchip.

Stable three-dimensional confinement is possible by adding a small amount of curvature to the axial bias field. This can be accomplished by running current in microfabricated wire segments perpendicular to the waveguide axis (Fig. 3-4). This style of three-dimensionally confining microtrap is referred to as a Z-wire trap due to the shape of the three wire segments [180].

Figure 3-5 shows a schematic of the microfabricated atom chip used for the experiments described in this thesis. The microchip was mounted in a horizontal plane in the science chamber such that the trapped condensates hung vertically below the

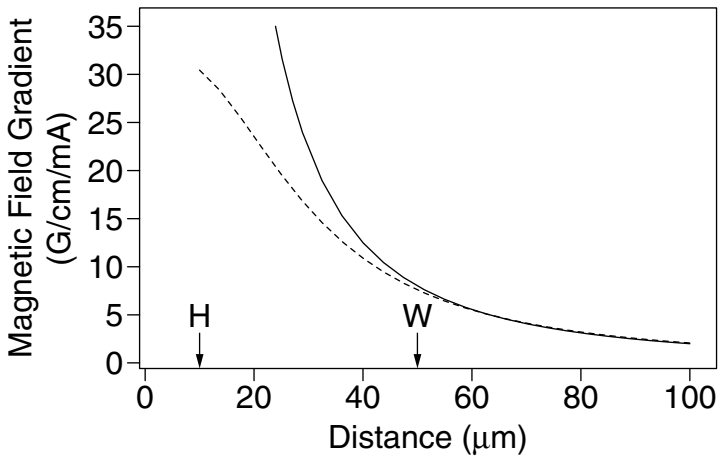

Figure 3-3: Circular vs rectangular wire cross section. The magnetic field gradient per unit current generated by a circular (solid line) and rectangular (dashed line) cross section wire is plotted as a function of distance from the wire. The rectangular wire has a width $W = 50$ μm and height $H = 10$ μm, identical to those shown in Fig. 3-5.

device. The wires were microfabricated on a 600 μm thick silicon substrate mounted on an aluminum block. They were 50 μm wide and electroplated with copper to a height of 10 μm. The minimum separation distance between wires was 50 μm (100 μm center-to-center). See Sec. 3.5 for additional technical details.

Condensates in the $|F = 1, m_F = -1\rangle$ state containing up to 3×10^6 atoms were delivered to the atom chip using optical tweezers (Ch. 2) and loaded into the Z-wire trap formed by currents I_1 and I_2 along with an orthogonal magnetic bias field $B_\perp$. An axial bias field, $B_{||}$, was applied to make the radial confinement harmonic and prevent non-adiabatic spin-flip transitions as discussed above. Transfer efficiency from the optical tweezers to the Z-wire trap was near unity.

3.2 Propagation in Magnetic Waveguides

The Z-wire trap was operated with $I_1 = I_2 = 1200$ mA, $B_\perp = 5.4$ G, and 3.0 G $\leq B_{||} \leq$ 3.6 G, corresponding to a separation of 450 μm between the condensate and the microchip surface. The measured axial trap frequency was $\omega_{||} = 2\pi \times 6.0$ Hz and the measured radial trap frequencies were $\omega_\perp = 2\pi \times (97.0,\ 91.1,\ 84.5)$ Hz for

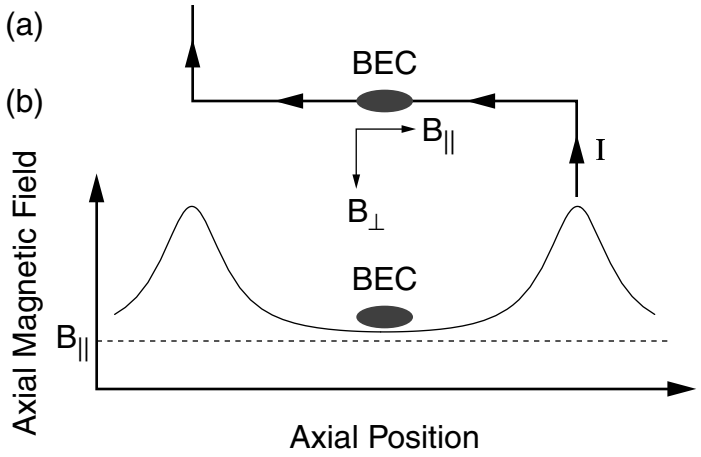

Figure 3-4: Z-wire magnetic trap. (a) The axis of the microtrap is horizontal. Radial confinement is provided by the horizontal wire segment and the external bias field, $B_\perp$ (Fig. 3-2). Axial confinement is provided by the magnetic field curvature created by the vertical wire segments that adds constructively with the applied axial bias field, $B_{||}$. The current, I, flows in the direction of the arrowheads. (b) Axial magnetic field profile.

$B_{||} = (3.0,\ 3.3,\ 3.6)$ G.

The condensate was transferred into the single-wire magnetic waveguide formed by I_1 and $B_\perp$ by ramping $I_2 \to 0$. The atoms were accelerated into the waveguide by the remaining endcap of the Z-wire trap. Sufficiently far downstream ($\sim$ 4 mm for $I_1 = 1200$ mA), the effect of this endcap was negligible and the condensate propagated at a constant velocity of 3.0 cm/s. Further control over its propagation velocity was possible by applying an external axial magnetic field gradient[4]. With gradients of $0 - 0.6$ G/cm, the atomic velocity (kinetic energy) was varied over the range $3.0 - 6.6$ cm/s [$h \times (25 - 121)$ kHz].

Single-mode (excitation-less) propagation was observed along homogeneous segments of the waveguide [Fig. 3-7(a)]. The condensates propagated with kinetic energies [$h\times(25-121)$ kHz] exceeding their transverse confinement energies ($\sim h\times 100$ Hz) and velocities ($3.0 - 6.6$ cm/s) exceeding the speed of sound ($c \approx 7$ mm/s) within the

[4]The uniform axial bias field, $B_{||}$, was applied with a pair of Helmholz coils co-axial with the waveguide. The axial field gradient was applied by running extra current through only one of these coils.

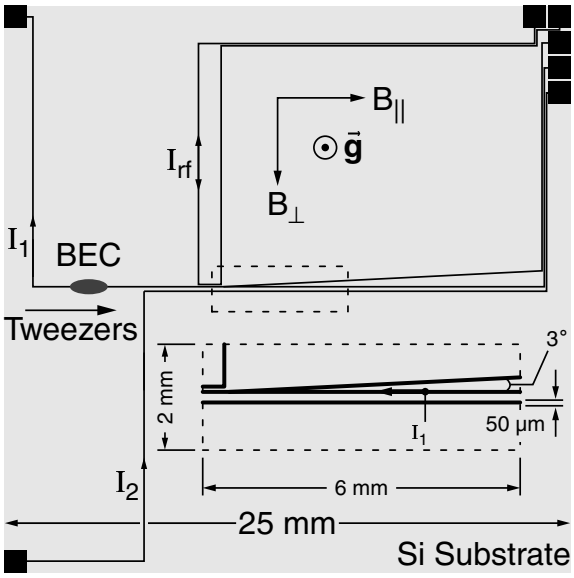

Figure 3-5: Microfabricated atom chip. Optical tweezers loaded Bose-Einstein condensates into the Z-wire trap (Fig. 3-4) formed by currents I_1 and I_2 in conjunction with the magnetic bias field $B_\perp$. Lowering I_2 to zero released the condensates into a single-wire magnetic waveguide. Atom flow was from left to right. The inset (dashed box) shows the widening of the waveguide wire in the region where another wire merges with it at a small angle. The only current flowing in the inset is I_1. Spatial variations in the axial magnetic field were measured by driving radio frequency spin-flip transitions with I_{rf}. The condensate was trapped above the plane of the page and the acceleration due to gravity, $\vec{g}$, points out of the page. All microfabricated features are drawn to scale.

gas[5]. Therefore, the atoms had enough kinetic energy to excite radial oscillations, and perturbations propagating through the condensate above a critical velocity, $v_c \leq c$, typically generate excitations [24, 34, 96, 163, 178]. Thus, excitation-less propagation along the waveguide was a noteworthy achievement.

3.2.1 Origins of Waveguide Perturbations

In a single-wire magnetic waveguide, anything that causes the current path to deviate from a straight line along the substrate generates perturbations to the waveguide potential. Possible origins of such deviations include geometric deformations of the wire, variations in resistivity over the cross section of the wire, current leakage into

[5]The condensate speed of sound, c, is given by $\mu = mc^2$, where μ is the chemical potential and m is the atomic mass. Typical condensate densities were $\sim 10^{14}$ atoms/cm^3.

the substrate, and instabilities due to high current density [121].

The inset to Fig. 3-5 shows a large geometric deformation to the microfabricated current-carrying wire. To zeroth order, such a deformation causes the waveguide axis to bend in a plane parallel to the surface of the microchip making an angle, θ, with respect to its nominal trajectory along which $B_{||}$ and $B_{\perp}$ are aligned parallel and perpendicular, respectively. This bend in the waveguide axis is capable of radially exciting propagating condensates in a plane parallel to the surface of the microchip.

With respect to the new waveguide axis, effective parallel, $B'_{||}$, and perpendicular, $B'_{\perp}$, magnetic fields are found by the rotation

$$B'_{||} = B_{||}\cos\theta - B_{\perp}\sin\theta, \tag{3.1}$$

$$B'_{\perp} = B_{\perp}\cos\theta + B_{||}\sin\theta, \tag{3.2}$$

where $-\pi/2 \leq \theta \leq \pi/2$. θ is taken to be a positive (negative) angle for the specific case of atoms entering (exiting) the waveguide perturbation depicted in the inset to Fig. 3-5.

Since the potential along the waveguide axis is determined by the local axial magnetic field (due to the Zeeman interaction) and the vertical position of the guide center (due to the gravitational interaction), changes in the effective parallel and perpendicular magnetic fields produce variations in the potential experienced by the propagating atoms. Variations in the effective parallel magnetic field are given by (for small angles)

$$\Delta B'_{||} = -B_{\perp}\sin\theta. \tag{3.3}$$

Thus, atoms entering (exiting) the perturbed guiding region will encounter a magnetic potential well (barrier). Furthermore, changes in the effective perpendicular magnetic field cause the atom-substrate distance, r, to vary by (for small angles)

$$\Delta r = -r\frac{\Delta B'_{\perp}}{B_{\perp}} = -r\frac{B_{||}}{B_{\perp}}\sin\theta. \tag{3.4}$$

Thus, the guide center entering (exiting) the perturbed guiding region will shift to-

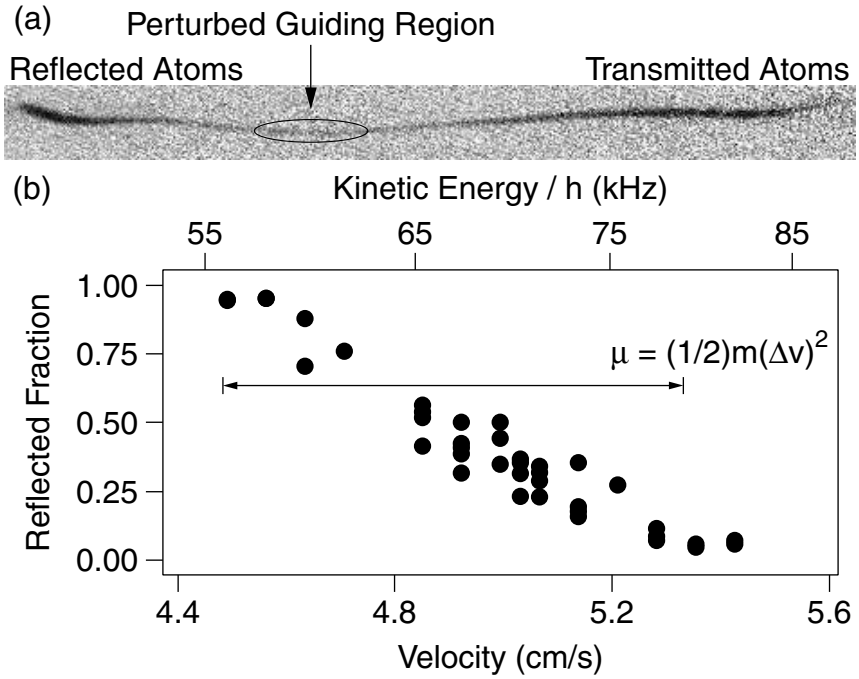

Figure 3-6: Scattering from waveguide perturbations. (a) Absorption image after 8 ms ballistic expansion of a condensate scattered from the waveguide perturbation shown in the inset to Fig. 3-5. The imaging light propagated parallel to the microchip surface and perpendicular to the waveguide axis. The incident velocity of the condensate was 5.0 cm/s. (b) The fraction of atoms reflected as a function of incident velocity. The velocity spread expected due to axial mean field expansion is indicted by the solid line (Eq. 3.5). Waveguide parameters for all data were $I_1 = 1200$ mA, $B_\perp = 5.4$ G, $B_{||} = 3.6$ G, and $\omega_\perp = 2\pi \times 84.5$ Hz. The field of view in (a) is 0.35 mm $\times$ 4.00 mm.

wards (away from) the surface of the microchip and atoms will encounter a gravitational potential barrier (well).

For ^{23}Na atoms in the $|1, -1\rangle$ state, the Zeeman interaction energy is $h \times 700$ Hz/mG and the gravitational interaction energy is $h \times 560$ Hz/μm. For the waveguide perturbation depicted in the inset to Fig. 3-5, the change in gravitational potential energy is negligible compared to the change in Zeeman interaction energy. However, the shift in atom-surface separation (Eq. 3.4) is capable of radially exciting propagating condensates in a plane normal to the surface of the microchip.

3.2.2 Reflections from Waveguide Perturbations

Equation 3.3 indicates that we should expect a large variation in the effective axial bias field for the waveguide perturbation depicted in the inset to Fig. 3-5. The local magnetic field in the perturbed guiding region was measured by driving radio frequency spin-flip transitions that removed atoms from the guide. It was found that upon entering (exiting) the perturbed region the magnetic bottom of the guiding potential decreased (increased) by $h \times (50 \pm 10)$ kHz. The signs of these shifts are consistent with those predicted by Eq. 3.3. The magnitude of the shift in the Zeeman energy upon exiting the guide is also consistent with the onset of transmission through the perturbed guiding region[6] [Fig. 3-6(b)]. From Eq. 3.3 with $B_\perp = 5.4$ G, the maximum angular deviation, θ_m, of the waveguide trajectory necessary to produce a $h \times 50$ kHz perturbation to the Zeeman energy is $\theta_m = 13$ mrad. The corresponding vertical displacement of the guide center from Eq. 3.4 with $B_\perp = 5.4$ G, $B_{||} = 3.6$ G, and $\theta_m = 13$ mrad is 4 μm. This yields a gravitational potential variation of $h \times 2.2$ kHz, which is small compared to the Zeeman energy shifts associated with the perturbation.

Figure 3-6(a) shows that the reflected atoms propagated slower than the transmitted atoms, i.e. they are closer the the perturbed guiding region. The center-of-mass velocity range over which partial reflection/transmission occurred indicates the axial velocity spread, Δv, of the propagating condensate. This spread can be accounted for by axial expansion due to mean field repulsion [173, 205, 214], which is approximately

$$\mu \approx \frac{1}{2} m (\Delta v)^2, \tag{3.5}$$

where μ is the atomic mean field energy and m is the atomic mass. For our conditions ($\mu \approx k_B \times 100$ nK $\approx h \times 2$ kHz), $\Delta v \approx 0.85$ cm/s.

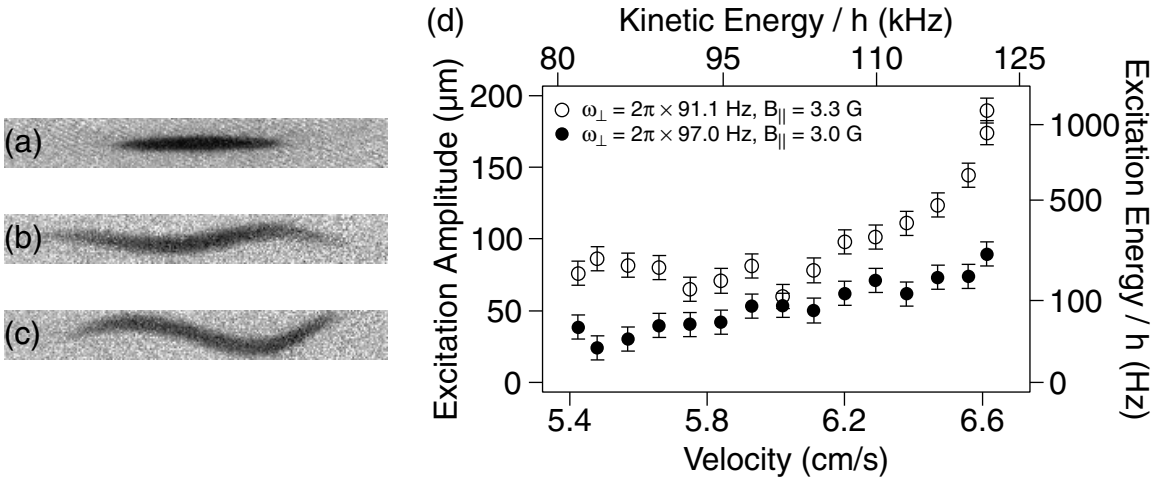

Figure 3-7: Propagation in a magnetic waveguide. Absorption images of condensates (a) entering and (b),(c) exiting the waveguide perturbation depicted in the inset to Fig. 3-5. The imaging light propagated parallel to the microchip surface and perpendicular to the waveguide axis. The waveguide potential was turned off and the condensates were allowed to expand ballistically for (a) 10 ms and (b),(c) 15 ms prior to imaging. (a) Condensate containing 2×10^6 atoms and accelerated to a velocity $v = 6.3$ cm/s. It propagated over 5 mm without excitation in a waveguide with $\omega_\perp = 2\pi \times 84.5$ Hz and $B_{||} = 3.6$ G. Condensates transmitted through the perturbed guiding region with $v = 6.5$ cm/s for (b) $\omega_\perp = 2\pi \times 97.0$ Hz and $B_{||} = 3.0$ G and (c) $\omega_\perp = 2\pi \times 91.1$ Hz and $B_{||} = 3.3$ G. (d) Peak-to-peak amplitudes of condensate excitations after 15 ms ballistic expansion vs velocity. For all data $I_1 = 1200$ mA and $B_\perp = 5.4$ G. All transmitted condensates propagated 4 mm beyond the perturbed guiding region before being imaged. The field of view in (a)-(c) is 0.26 mm × 2.00 mm.

3.2.3 Excitations due to Waveguide Perturbations

Condensates transmitted through the waveguide perturbation depicted in the inset to Fig. 3-5 were radially excited (Fig. 3-7). The imaging axis only provided sensitivity to transverse excitations in a plane normal to the surface of the microchip. Larger excitations are expected in a plane parallel to the surface of the microchip.

The nearly sinusoidal nature of the condensate excitations shown in Figs. 3-7(b) and 3-7(c) indicates that the dipole mode of the condensate was primarily excited for $B_{||} \leq 3.6$ G. Further evidence for this comes from the fact that little variation in the excitation amplitude as a function of the propagation time after exiting the

[6] A 4.2 cm/s atomic velocity corresponds to a kinetic energy shift of $h \times 50$ kHz.

perturbed guiding region was observed. Conversely, transmitted condensates showed strong signs of higher order excitations when $B_{||}$ was increased beyond 3.6 G corresponding to $\omega_{\perp} \leq 2\pi \times 84.5$ Hz. The absorption images deviated visibly from a smooth sinusoidal shape. In addition, the measured excitation amplitude depended strongly on propagation time indicting the phasing and dephasing of several excitation modes.

Figure 3-7(d) shows a clear increase in the excitation amplitude for increasing velocity at fixed $B_{||}$ and $\omega_{\perp}$ as well as for increasing $B_{||}$ (decreasing $\omega_{\perp}$) at fixed velocity. Both trends are consistent with the expectation of increased excitations for an increased ratio of atomic center-of-mass kinetic energy to transverse confinement energy. The latter trend is also consistent with the expectation of increased excitations for an increased perturbation size since, from Eq. 3.4, the vertical displacement of the guide center is proportional to $B_{||}$.

3.3 Microfabricated Surface Effects

As emphasized above, bringing atoms closer to smaller current-carrying wires inherently increases the magnetic forces acting on them. This implies that finer coherent control is possible, but it also means that atoms confined in magnetic microtraps and waveguides will be more sensitive to perturbations and noise emanating from the microfabricated surface.

3.3.1 Fragmentation

While single-mode waveguiding was possible 450 μm away from the microfabricated surface, condensates confined in the Z-wire trap were observed to fragment longitudinally when the atom-surface separation was reduced to < 200 μm (Fig. 3-8). The axial location of the fragments was reproduced on each realization of the experiment, and more fragments appeared as the condensates were brought closer to the microfabricated surface. This prevented smooth propagation along the waveguide close to the microfabricated surface. While perturbations to the waveguide potential are detrimental for atom optical applications such as interferometry, the disordered po-

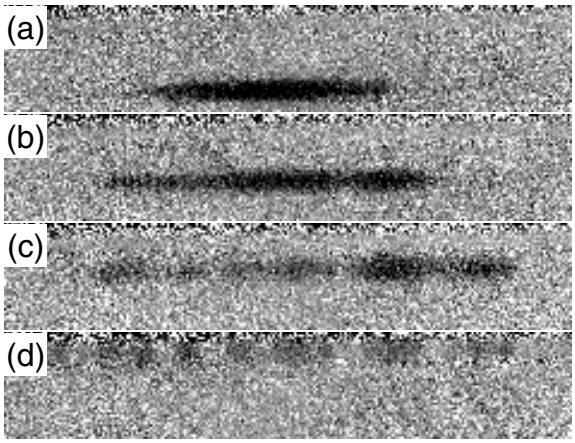

Figure 3-8: Fragmentation in a magnetic microtrap. Absorption images of condensates after 5 ms ballistic expansion from the magnetic microtrap (Fig. 3-5). The imaging light propagated parallel to the microchip surface and perpendicular to the microtrap axis. The atom-substrate separation was (a) 190 μm, (b) 145 μm, (c) 100 μm, and (d) 55 μm. For all images, the condensate started in a trap with $I_1 = I_2 = 540$ mA, $B_\perp = 5.4$ G, and $B_{||} = 0.3$ G corresponding to an atom-substrate separation of 200 μm. The condensate was translated towards the substrate by lowering the wire currents linearly over 500 ms. The atoms were held at their final position for 100 ms prior to trap shut off. The field of view in (a)-(d) is 0.37 mm $\times$ 2.00 mm.

tential along the waveguide axis might be used to study superfluid-insulator (Bose glass) transitions [45, 59, 64, 216].

As shown above, variations in the current path along the microfabricated wires led to perturbations in the guiding potential. Finer variations in the current path are expected to become evident as the microtrap/waveguide center approaches the microfabricated surface. To test if irregular current flow in the microfabricated wires caused the observed condensate fragmentation, as opposed to magnetic dopants/impurities for example, condensates were confined in an optical dipole trap at the same location relative to the microfabricated surface (Fig. 3-9). The magnetic and optical trapping parameters were made nominally identical (same atom-surface separation, axial bias field, and radial trap frequencies) such that any surface contaminants (magnetic dopants/impurities, etc...) would perturb the clouds identically. No fragmentation was observed for optically confined condensates. The lack of condensate fragmentation in the optical dipole trap confirms that the longitudinal potential corrugations

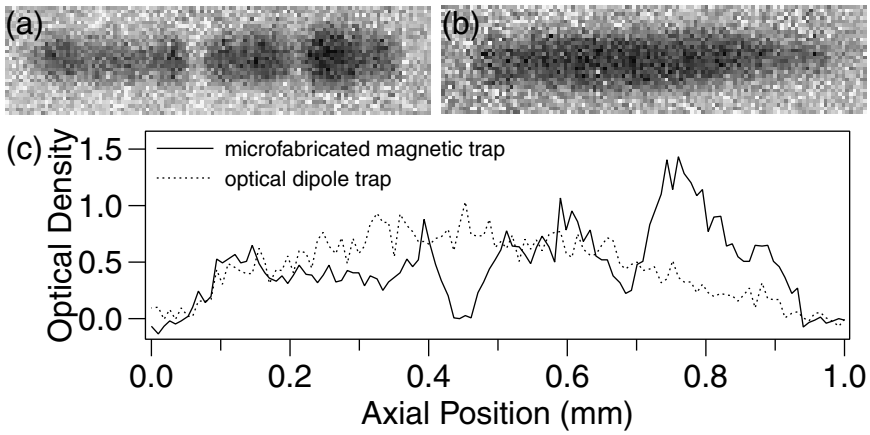

Figure 3-9: Lack of fragmentation in an optical dipole trap. Absorption images after 10 ms ballistic expansion of condensates containing $\sim 10^6$ atoms held at a distance of 85 μm from the microfabricated surface for 15 s in the (a) magnetic microtrap and (b) optical dipole trap. The imaging light propagated parallel to the microchip surface and perpendicular to the microtrap/optical trap axis. (c) Radially averaged optical density vs axial position for condensates shown above. Longitudinal fragmentation occurred for condensates held in the magnetic microtrap, but not for those confined optically at the same location with the magnetic trap off. The magnetic trap was operated with $I = 130$ mA, $B_\perp = 3.2$ G, and $B_{||} = 1.4$ G yielding a radial trap frequency $\omega_\perp = 2\pi \times 450$ Hz. The optical dipole trap had a radial trap frequency $\omega_\perp = 2\pi \times 425$ Hz and was operated with $B_{||} = 1.8$ G. For both condensates, the chemical potential was $\mu \approx k_B \times 120$ nK. The field of view in (a) and (b) is 0.25 mm $\times$ 1.00 mm.

observed in the magnetic microtrap arose due to the presence of irregular current flow in the microfabricated wires. This is in agreement with conclusions reached in Refs. [101, 121].

For the data shown in Figs. 3-8 and 3-9, the condensate chemical potential was $\mu \approx k_B \times 100$ nK. This implies that a ~ 3 mG "bump" in the axial magnetic field is sufficient to cut the condensate into fragments. It should not be surprising that milligauss level axial magnetic field variations exist over length scales comparable to the atom-surface separation. The magnetic field generated by the microfabricated wires is typically a few gauss ($B_{wire} = B_\perp = 5.4$ G in Fig. 3-8 and $B_{wire} = B_\perp = 3.2$ G in Fig. 3-9). Thus, 1 mrad angular deviations of the waveguide axis (Eq. 3.3) will produce axial magnetic field variations capable of breaking the condensate into fragments.

Figure 3-8(d) shows that for an atom-surface separation of 55 μm, the trapping potential developed axial variations with a characteristic length scale of $100-150$ μm. Resoundingly periodic fragmentation has been observed elsewhere with a similar period [62, 101]. Theoretical calculations have revealed that aperiodic fluctuations in the current path along the substrate can produce quasi-periodic perturbations to the waveguide potential with a length scale set by the atom-surface separation [216].

A microchip similar to that depicted in Fig. 3-5 was fabricated with conductors 50 μm wide and evaporated with gold to a height of 1.25 μm. Condensates confined near its surface were observed to fragment also. To date, condensate fragmentation has been observed near copper [62, 122], gold [125], and aluminum [102] conductors.

3.3.2 Trap Lifetimes

Confined atoms with non-zero magnetic moment are sensitive to mechanical and magnetic field noise at multiples of their trap frequencies and magnetic field noise at their Zeeman splitting frequency [82, 84, 85, 86, 87, 88, 102, 132]. Noise at the trap frequency leads to heating and subsequent trap loss after the atoms acquire an energy greater than the trap depth. Spin-flip transitions driven by radio frequency noise at the atomic Zeeman splitting frequency distribute the atomic population across magnetically confinable and unconfinable states. This causes atom loss for clouds held in magnetic traps. However, all spin states are confined by optical dipole traps and atoms undergoing spin-flip transitions have been directly observed (Sec. 3.3.3).

The lifetime of condensates confined in either the magnetic microtrap or optical dipole trap at distances ≥ 70 μm from the microfabricated surface was measured to be ≥ 20 s and independent of the atom-surface separation (Fig. 3-10).

Several experimental details altered the measured condensate lifetime. Excitations created during the magnetic microtrap loading were found to shorten the measured lifetime, and care had to be taken to overlap the optical and magnetic traps during transfer to minimize such excitations. Translating the condensate either towards or away from the microfabricated surface by adiabatically varying I_1, I_2, and $B_\perp$ to shift the trap center while maintaining a constant radial trap frequency was found to

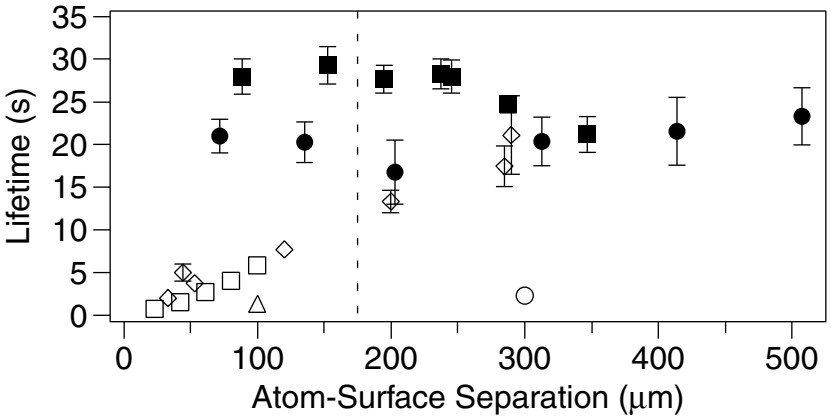

Figure 3-10: Lifetime near a microfabricated surface. The $1/e$ lifetime of condensates confined in the magnetic microtrap (solid squares) and optical dipole trap (solid circles) is shown to be independent of distance from the microfabricated surface. I_1, I_2, and $B_\perp$ were varied with distance to maintain the radial magnetic trap frequency at $\omega_\perp = 2\pi \times 450$ Hz with $B_{||} = 1.4$ G. The vertical dashed line indicates the onset of longitudinal condensate fragmentation in the magnetic trap. In the optical dipole trap, the condensate was held directly below the microfabricated wire used to form the magnetic trap with $B_{||} = 1.8$ G. No external connections were made to the microchip. The optical dipole trap had axial and radial trap frequencies $\omega_z = 2\pi \times 4$ Hz and $\omega_\perp = 2\pi \times 425$ Hz, respectively. Only atoms remaining in the $|1, -1\rangle$ state were resonant with the absorption imaging light. For comparison, the distance dependence of thermal cloud lifetimes measured in Ref. [62] is shown for atoms confined magnetically by a microstructure (open squares) and copper wire (open diamonds). Error bars smaller than the symbol size are not included. Also, magnetically confined condensate lifetimes reported in Ref. [80] (open triangle) and Ref. [62] (open circle) are shown for comparison.

decrease the condensate lifetime. This presumably resulted from excitations induced by irregular current changes due to technical limitations in controlling the power supplies connected to the microchip. As a result, microfabricated magnetic trap lifetime data is only presented for atom-surface separations ≥ 70 μm, where the atoms were loaded into their final position directly from the optical tweezers[7].

Occasionally, heating was observed for atoms in both the microfabricated magnetic trap and optical dipole trap due to technical noise at the trap frequency, even with care taken to eliminate ground loops and minimize cable lengths[8]. Connecting a

[7]The optical tweezers beam began to clip on the support structures for the microchip when placed within 70 μm of the microfabricated surface.

[8]The current supply for the microfabricated wire and the wire itself were grounded to the vacuum

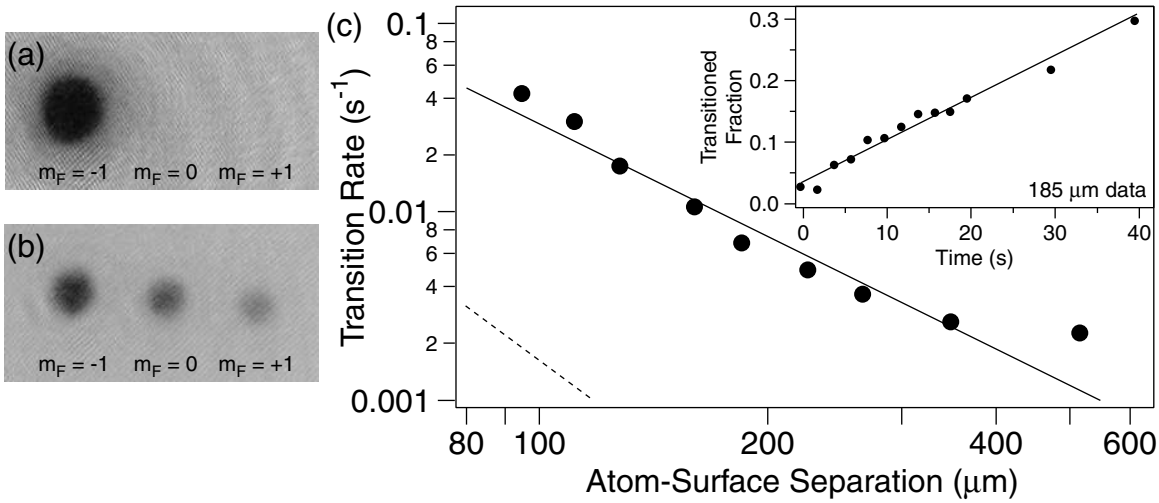

Figure 3-11: Radio frequency spin-flip transitions. Axial absorption images after 22 ms ballistic expansion of condensates held in the optical dipole trap at a distance of 185 μm from the microfabricated surface for (a) 0 s and (b) 40 s. A magnetic field gradient was applied during ballistic expansion to separate the different spin states. (c) Spin-flip transition rate, Γ, vs distance, r, from the microfabricated surface on a log-log scale. A solid line $\Gamma \propto 1/r^2$ is provided as a guide for technical noise driven spin-flip transitions. A dashed line $\Gamma \propto 1/r^3$ gives an upper limit for thermal noise driven spin-slip transitions (Sec. 3.3.4). The inset shows the fraction of the total atoms in the $m_F = 0$ state with the transition rate being defined as the initial slope of the data (before any atoms in the $m_F = +1$ state were detected). For all data, $B_{||} = 1.8$ G yielding a Zeeman splitting frequency of 1.26 MHz. The absorption imaging light propagated parallel to the optical trap axis and was resonant with the $F = 2 \rightarrow F' = 3$ transition. The atoms were optically pumped into the $F = 2$ hyperfine level with a pulse resonant with the $F = 1 \rightarrow F' = 2$ transition. This provided equal imaging sensitivity to each magnetic sublevel. The field of view in (a) and (b) is 1.0 mm $\times$ 2.0 mm.

10 mF capacitor in parallel with the 2 Ω microfabricated wire ($1/RC = 2\pi \times 8$ Hz) eliminated such effects. Thereafter, applying radio frequency power to the microchip at a frequency chosen to limit the trap depth for magnetically confined atoms did not consistently alter the condensate lifetime.

3.3.3 Radio Frequency Spin-Flip Transitions

Weak radio-frequency noise in the microfabricated wires was observed to drive spin-flip transitions. Optically confined condensates initially in the $|1,-1\rangle$ state [Fig. 3-11(a)] were found to make transitions to other magnetic sublevels [Fig. 3-11(b)]. Such transitions would act as a loss mechanism for magnetically confined clouds. The transition rate was found to decrease as the square of the atom-surface separation distance, r. Since the magnetic field of a straight wire decays as $1/r$, and the power scales as the square of the field, the $1/r^2$ dependence of the spin-flip transition rate is expected for atoms in the near field ($r \ll \lambda$) of the wire, where $\lambda \approx 300$ m is the wavelength of ~ 1 MHz radiation. The transition rate at large r may fall above the above the $1/r^2$ decay due to low level radio frequency noise from other sources.

The transition rate vs distance data presented in Fig. 3-11(c) was taken with all connections necessary to run the microfabricated magnetic trap made to the microchip, but with no current flowing in the microfabricated wires. The atoms were exposed to an axial bias field $B_{||} = 1.8$ G to simulate the field configuration in the microfabricated magnetic trap. This also maximized their sensitivity to fluctuating fields generated by wire currents since $\Delta m_F = \pm 1$ radio frequency transitions are only driven by magnetic fields oscillating orthogonal to a static bias field. Spin-flip transitions were suppressed by exposing the optically confined atoms to a bias field, $B_{\perp}$, perpendicular (parallel) to the microfabricated wire (surface).

The radio frequency driven spin-flip transition rate depended strongly on experimental details, suggesting that antenna effects coupled radio frequency noise into the system. The rate was measured to be ~ 100 times higher if care was not taken to carefully eliminate ground loops and use minimal cable lengths. Also, with no connections to the microchip, spin-flip transitions were not detectable for condensates held up to 60 s. The spin-flip rate presented in Fig. 3-11(c) became comparable to the measured condensate decay rate displayed in Fig. 3-10 for atom-surface separations < 100 μm. Thus, extending long condensate lifetimes much closer to the surface will

chamber at the location of the electrical feedthrough for the microchip connections. The total length of all (unshielded) current-carrying cables was ~ 1 m.

require further radio frequency shielding and/or filtering.

3.3.4 Thermal Noise

Confining and manipulating ultracold atomic vapors with electromagnetic fields allows for the microkelvin [37, 39, 172], nanokelvin [40, 110], and even picokelvin [124] temperature clouds to remain thermally isolated from their 300 K laboratory environment. Such thermal isolation is noteworthy in microtrap configurations where ultracold atoms are confined within a few microns of room temperature material surfaces, establishing temperature gradients $> 10^8$ K/m.

For neutral atoms with a non-zero magnetic moment, limitations to this temperature gradient arise from fluctuating magnetic fields generated by thermal noise in the material surfaces. These fluctuating magnetic fields may cause heating, spin-flip transitions, and decoherence in condensates trapped near conducting surfaces [82, 84, 85, 86, 87, 88, 102]. Spin-flip transitions driven by thermally induced radio frequency magnetic field noise have been observed in atomic vapors confined within ~ 100 μm of from macroscopic structures well approximated by conducting planes of infinite thickness [82, 102] and within ~ 10 μm of thinner conducting planes [132]. Typical microfabricated devices (Fig. 3-5) have feature sizes smaller than the skin depth of radio frequency radiation. This reduces the power of emitted radiation and suppresses spin-flip transitions as compared to macroscopic conductors.

Near a conducting plane of infinite thickness, thermally induced radio frequency noise drives the $|1,-1\rangle \rightarrow |1,0\rangle$ transition at a rate [82, 87]

$$\Gamma = \frac{9}{256\pi}\frac{\mu_B^2 k_B T}{\epsilon_0^2 \hbar^2 c^2 \rho}\frac{1}{r}\frac{\delta^3}{3\delta^3 + 2r^3}, \tag{3.6}$$

where the conducting material has resistivity ρ and temperature T, r is the atom-surface separation, ϵ_0 is the permittivity of free space, c is the speed of light, and

$$\delta = \sqrt{\frac{2\epsilon_0 c^2 \rho}{\omega_L}} \tag{3.7}$$

is the skin depth for radiation at the Zeeman splitting (Larmor) frequency ω_L.

For $r \ll \delta$, Eq. 3.6 can be approximated by

$$\Gamma = \frac{3}{256\pi} \frac{\mu_B^2 k_B T}{\epsilon_0^2 \hbar^2 c^2 \rho} \frac{1}{r}. \tag{3.8}$$

In comparison, the spin-flip transition rate near a conducting plane of finite thickness H is [86]

$$\Gamma = \frac{3}{256\pi} \frac{\mu_B^2 k_B T}{\epsilon_0^2 \hbar^2 c^2 \rho} \frac{1}{r} \frac{H}{r+H}, \tag{3.9}$$

and near a circular wire of radius R is [86]

$$\Gamma = \frac{3}{512} \frac{\mu_B^2 k_B T}{\epsilon_0^2 \hbar^2 c^2 \rho} \frac{R^2}{r^3}. \tag{3.10}$$

Typical Zeeman splitting frequencies are $\omega_L \approx 2\pi \times 1$ MHz corresponding to a skin depth $\delta = 66$ μm for $\rho = 1.7 \times 10^{-6}$ Ω-cm (the bulk resistivity of copper[9]). Using Eqs. 3.8-3.10 for $r \approx \delta$ gives an upper limit for the thermally induced spin-flip transition rate near a conducting surface. At a distance $r = \delta = 66$ μm from room temperature ($T = 300$ K) copper conductors, Eqs. 3.8-3.10 predict $\Gamma \approx 200$ mHz, $\Gamma \approx 20$ mHz, and $\Gamma \approx 2$ mHz for an infinitely thick plane, a plane of thickness $H = 10$ μm, and a wire of radius $R = 5$ μm, respectively. This demonstrates the strong suppression of thermal noise radiated from microfabricated devices due to geometrical considerations. The thermally induced spin-flip transition rate is expected to approach $\Gamma = 1$ Hz at distances ~ 10 μm away from microfabricated devices with ~ 10 μm features.

3.4 Waveguide Beam Splitters

Section 3.1 described a single magnetic waveguide created by a single current-carrying wire and bias field. A pair of waveguides can be generated by running parallel currents in two microfabricated wires with the same bias field still applied. The separation

[9]Often microfabricated conductors have resistivities up to a factor of ten higher than the bulk resistivity of the material.

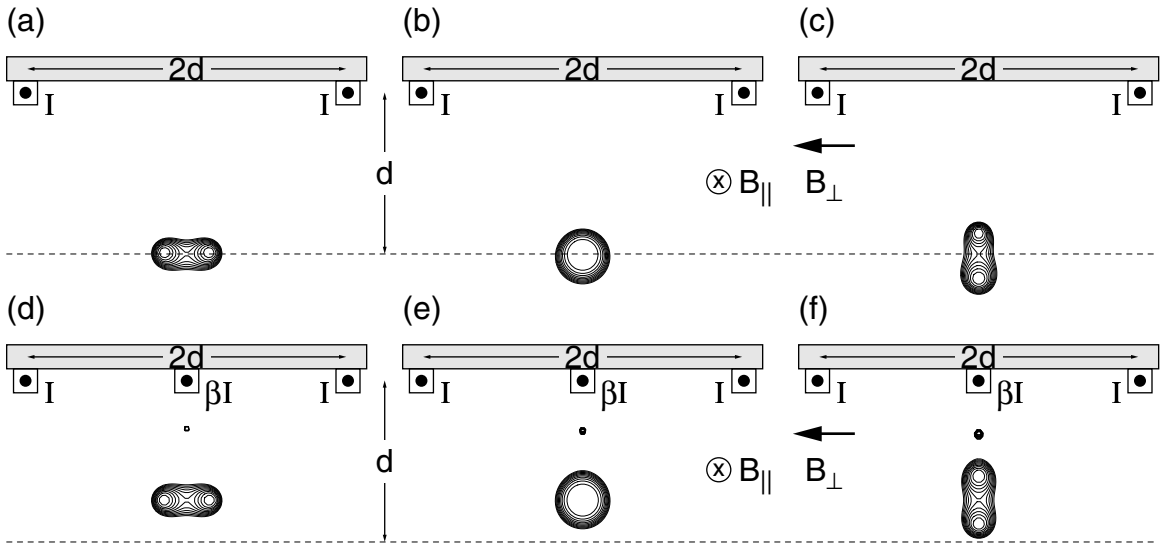

Figure 3-12: Waveguide beam splitter. Contours of constant magnetic field for two wires running current I separated by a distance $2d$ with (a) $B_\perp = 0.990 \times \mu_0 I/2\pi d$, (b) $B_\perp = 1.000 \times \mu_0 I/2\pi d$, and (c) $B_\perp = 1.010 \times \mu_0 I/2\pi d$. Adding a central wire running current βI, $\beta = (\sqrt{2}-1)/2 \approx 0.207$ symmetrizes the potential wells split perpendicular to the surface [(c) compared to (f)]. It also creates an extraneous third well. (d) $B_\perp = 1.226 \times \mu_0 I/2\pi d$, (e) $B_\perp = 1.236 \times \mu_0 I/2\pi d$, and (f) $B_\perp = 1.246 \times \mu_0 I/2\pi d$. In (a)-(f), $B_{||} = 0.1 \times \mu_0 I/2\pi d$ and the magnetic field contours are spaced in increments of $10^{-4} \times \mu_0 I/2\pi d$ above $B_{||}$. In (b) and (e), the merged potential is quartic because the radial magnetic field profile has a hexapole symmetry.

between the guide centers is a function of the applied bias field, $B_\perp$, wire separation, $2d$, and wire currents, I (Fig. 3-12). Merging and splitting guide centers is possible by varying these parameters and can act as a beam splitter for atomic wavepackets. Such beam splitters form the basis of existing microchip-based atom interferometry proposals [8, 81, 90].

Condensates split by varying I and/or $B_\perp$ in a double waveguide geometry (Fig. 3-12) were heated into thermal clouds due to technical limitations (Fig. 3-13). As an alternative, we have demonstrated coherent condensate beam splitting using optical potentials (Ch. 4).

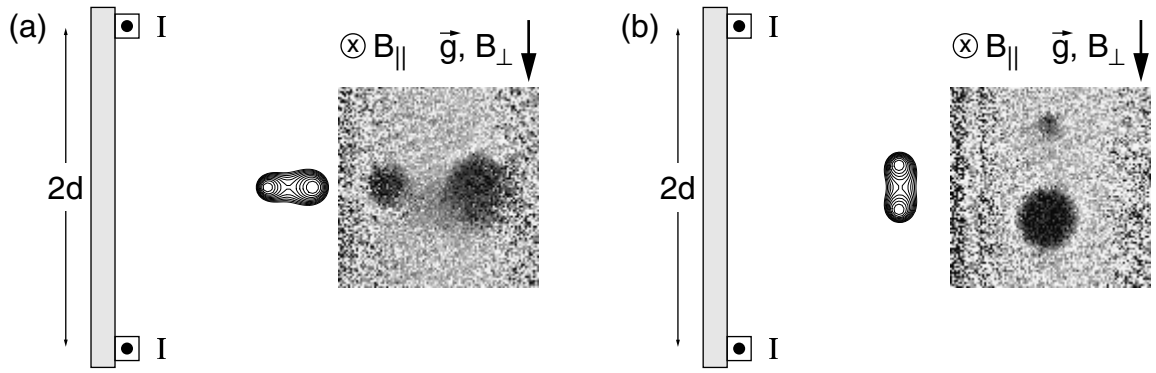

Figure 3-13: Atomic wavepacket division. Axial absorption images of thermal clouds split (a) horizontally and (b) vertically in a magnetic double-well potential. $I = 300$ mA, $B_{||} = 1$ G, $2d = 600$ μm, and (a) $B_{\perp} < 2$ G and (b) $B_{\perp} > 2$ G. The acceleration due to gravity, $\vec{g}$, points down the page. The field of view for the absorption images is 650 μm $\times$ 650 μm.

3.5 Microfabrication Procedures

The microchip in Fig. 3-5 was fabricated by MIT's Microsystems Technology Laboratories. Their fabrication procedure is outlined here.

A 600 μm thick silicon wafer was used as a substrate to support the microfabricated wires. A $\sim$ 200 nm thick SiO_2 layer was deposited on top of the silicon wafer to electrically isolate the microfabricated wires from the substrate. Next a photoresist layer was added. The microfabricated wire pattern was imaged onto the photoresist with ultraviolet light. The photoresist was then developed such that the photoresist was removed from the surface of the chip only where the wires were to be fabricated. The remainder of the chip remained coated in photoresist. A $\sim$ 20 nm chrome adhesion layer was deposited over the wafer followed by a $\sim$ 200 nm copper layer. These metal layers coated the entire wafer, but only reached the Si/SiO_2 substrate where the photoresist had been removed in the pattern of the microfabricated wires. Next, the remaining photoresist was removed leaving a bare Si/SiO_2 wafer with Cr/Cu microfabricated wires. These wires were electroplated with copper to a thickness of 10 μm.

The 50 μm $\times$ 10 μm cross section wires were $\sim$ 35 mm long and had a resistance of $\sim$ 2 Ω. The wires could withstand currents of 1.2 A steady-state, but burnt out

instantly when we tried to run 1.4 A through them. The microfabricated wires were connected to macroscopic copper leads with a thin gold ribbon. The gold ribbon was bonded to the microchip and macroscopic copper leads by gap welding with a short current pulse. The microchip was clamped to an aluminium block by overhanging screw heads.

Once installed in the science chamber, the microchip was baked at 150 C for five days in order to achieve the necessary ultrahigh vacuum pressure ($\sim 10^{-11}$ torr). After baking, several of the microfabricated wires were no longer connected to their leads. After removing the microchip from the chamber, many of the gold ribbons were found to be broken.

Other fabrication techniques are currently being tested. We are testing wires up to 2 μm thick made from evaporated gold rather than electroplated copper. Also, we are connecting the microchip to macroscopic leads with mechanical clamps. However, the electrical isolation provided by the silicon substrate seems to degrade under mechanical stress after baking.

Chapter 4

Trapped-Atom Interferometry in an Optical Double-Well Potential

Demonstrating atom interferometry [16] with particles confined by magnetic [80, 122, 165, 195] and optical [52, 53] microtraps and waveguides would realize the matter wave analog of optical interferometry using fiber-optic devices. Current proposals for confined-atom interferometers rely on the merger and separation of two potential wells to coherently divide atomic wavepackets [8, 81, 90]. This type of division differs from previously demonstrated atomic beam splitters. To date, atomic beams and vapors have been coherently diffracted into different momentum states by mechanical [26, 72, 109] and optical [72, 105] gratings, and Bose-Einstein condensates have been coherently delocalized over multiple sites in optical lattices [5, 30, 69, 70, 138, 164]. Atom interferometers utilizing these beam splitting elements have been used to sense accelerations [5, 105, 168] and rotations [73, 129], monitor quantum decoherence [31], characterize atomic and molecular properties [56], and measure fundamental constants [71, 168, 219].

It is difficult to compare atom interferometers and optical interferometers because they are typically sensitive to different forces and potentials. However, one common comparison is their rotation sensitivity. For this purpose, atom interferometers have an inherent advantage over their optical counterparts. The Sagnac phase shift of a

gyroscope enclosing an area $\vec{A}$ and undergoing rotation at a rate $\vec{\Omega}$ is

$$\Delta\phi_{rot} = \frac{4\pi}{\lambda v}\vec{\Omega}\cdot\vec{A}, \tag{4.1}$$

where λ and v are the wavelength and velocity of the interfering particles, respectively. For atoms of mass m and photons of frequency ω, matter wave interferometers [73, 129] can outperform optical gyroscopes [36] by a factor of $mc^2/\hbar\omega \sim 10^{10}$, where c is the speed of light. This is provided that both devices enclose the same area, which at present is not possible. Current atom interferometers enclose far less area than optical gyroscopes such that in practice their rotation sensitivities are nearly equal [73]. Guided-atom interferometers have the potential to enclose large areas and therefore to increase the ultimate rotation sensitivity of matter wave gyroscopes.

The work presented in Ch. 3 was largely motivated by the goal of creating a miniaturized atom interferometer. However, technical limitations have currently prevented us from coherently splitting condensates with our magnetic microtraps and waveguides (Ch. 3, Fig. 3-13). This chapter describes our parallel efforts to implement a trapped-atom interferometer using optical potentials and expands on the work presented in Ref. [199] (App. C).

We have demonstrated a trapped-atom interferometer with gaseous Bose-Einstein condensates confined in an optical double-well potential. Condensates were coherently split by deforming an initially single-well potential into two wells separated by 13 μm. The relative phase between the two condensates was determined from the spatial phase of the matter wave interference pattern formed upon releasing the atoms from the separated potential wells [9, 138]. This recombination method avoids deleterious mean field effects [201, 206] and yields an accurate measurement of applied phase shifts on a single realization of the experiment, unlike in-trap recombination schemes [8, 81, 90].

The large separation between the split potential wells allowed the phase of each condensate to evolve independently and either condensate to be addressed individually. An ac Stark phase shift was applied to either condensate by temporarily turning

off the optical fields generating its potential well. The spatial phase of the resulting matter wave interference pattern shifted linearly with the applied phase shift and was independent of the time of its application. This verified the phase sensitivity of the interferometer and the independent phase evolution of the separated condensates. The measured coherence time of the separated condensates was 5 ms.

This chapter describes a trapped-atom interferometer with two interfering paths. The two-path geometry has the flexibility to measure either highly localized potentials or uniform potential gradients, such as those arising from atom-surface interactions or the Earth's gravitational field, respectively. In contrast, multiple-path interferometers demonstrated in optical lattice systems are restricted to measurements of the latter [5, 138].

4.1 Optical Double-Well Potential

Condensates in the $|F = 1, m_F = -1\rangle$ state containing up to 3×10^6 atoms were delivered to the science chamber using optical tweezers (Ch. 2) and loaded into a secondary optical trap formed by a counter-propagating, orthogonally-polarized 1064 nm laser beam shifted in frequency from the tweezers by ~ 100 MHz to avoid interference effects.

The secondary optical trap was formed by a collimated laser beam that passed through an acousto-optic modulator (AOM) and was focused onto the condensate with a lens [Fig. 4-1(a)]. The AOM was driven simultaneously by two radio frequency (rf) signals to tailor the shape the potential from single-well [Fig. 4-1(b)] to double-well [Fig. 4-1(c)]. The separation between the potential wells was controlled by the frequency difference between the rf drives. The $1/e^2$ radius of each focused beam was 5 μm. For typical optical powers, this resulted in a single beam trap depth $U_0 = h \times 5$ kHz and a radial (axial) trap frequency $\omega_r = 2\pi \times 615$ Hz ($\omega_z = 2\pi \times 30$ Hz).

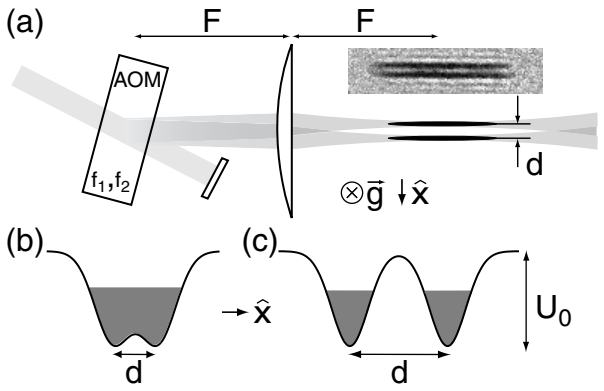

Figure 4-1: Optical double-well potential. (a) Schematic diagram of the optical setup for the double-well potential. An acousto-optic modulator (AOM) was driven simultaneously by two frequencies, f_1 and f_2, and diffracted a collimated beam into two beams. The AOM was placed in the focal plane of a lens of focal length F so that the two beams propagated parallel to each other. The radial separation of the potential wells, d, was controlled by the frequency difference, $\Delta f = |f_1 - f_2|$. The acceleration due to gravity, $\vec{g}$, points into the page. The absorption image shows two well-separated condensates confined in the double-well potential diagramed in (c). The field of view is 70 μm $\times$ 300 μm. Energy diagrams for (b) initial single-well trap with $d = 6$ μm and (c) final double-well trap with $d = 13$ μm. In both (b) and (c), $U_0 = h \times 5$ kHz and the peak atomic mean field energy was $\sim h \times 3$ kHz. The potential "dimple" in (b) was $< h \times 500$ Hz which was much less than the peak atomic mean field energy allowing the trap to be characterized as a single-well. The potential "barrier" in (c) was $h \times 4.7$ kHz which was larger than the peak atomic mean field energy allowing the resulting split condensates to be characterized as independent.

4.2 Matter Wave Interference

Condensates were initially loaded from the tweezers into a single-well trap [Fig. 4-1(b)]. After holding the cloud in this trap for 15 s to damp excitations, the condensate contained $\sim 10^5$ atoms with a peak atomic mean field energy $\mu \approx h \times 3$ kHz. The single-well trap was deformed into a double-well potential [Fig. 4-1(c)] by linearly increasing the frequency difference between the rf signals driving the AOM over 5 ms. The amplitude of the rf signals were tailored during the splitting process to guarantee an even division of the condensate atoms and nearly equal trap depths after splitting.

Releasing the condensates from the double-well potential allowed them to ballistically expand, overlap, and interfere (Fig. 4-2). Each realization of the experiment

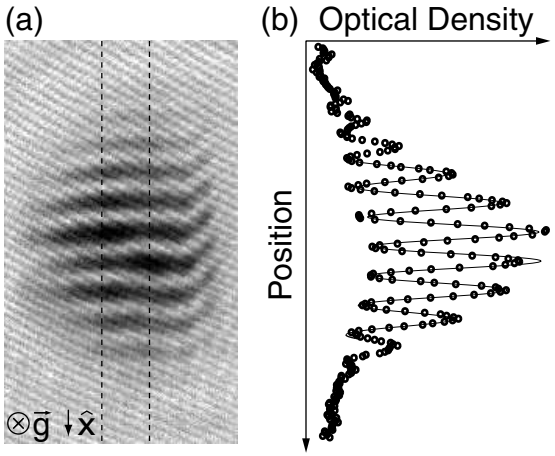

Figure 4-2: Matter wave interference. (a) Absorption image of condensates released from the double-well potential in Fig. 4-1(c) and allowed to overlap during 30 ms ballistic expansion. The imaging axis was parallel to the direction of gravitational acceleration, $\vec{g}$. The field of view is 600 μm $\times$ 350 μm. (b) Radial density profiles were obtained by integrating the absorption signal between the dashed lines. Typical images gave $>$ 60% contrast. The solid line is a fit to a sinusoidally-modulated Gaussian curve from which the phase of the interference pattern was extracted (see text). This figure presents data acquired in a single realization of the experiment, i.e. a single shot.

produced a matter wave interference pattern with the same spatial phase. This reproducibility demonstrated that deforming the optical potential from a single-well into a double-well coherently split the condensate into two clouds with deterministic relative phase, i.e. the relative phase between the two condensates was the same from shot-to-shot.

This experiment derived its double-well potential from a single laser beam passing through an AOM. Thus, vibrations and fluctuations of the laser beam were common mode to both wells, and a clean and rapid trap turn off was achieved by switching off the rf power driving the AOM. In contrast, past experiments created a double-well potential by splitting a magnetically trapped condensate with a blue-detuned laser beam [9]. This previous work was unable to observe a reproducible relative phase between the split condensates. This was attributed to an unstable potential barrier separating the two condensates due to pointing fluctuations in the blue-detuned laser beam and irreproducible turn off of the high current magnetic trap that initiated

ballistic expansion.

4.2.1 Relative Phase

The relative phase between the two separated condensates was determined by the spatial phase of their matter wave interference pattern. For a ballistic expansion time $t \gg 1/\omega_r$, each condensate had a quadratic phase profile [42],

$$\psi_{\pm}(\vec{r},t) = \sqrt{n_{\pm}(\vec{r},t)}\ e^{i\frac{m}{2\hbar t}|\vec{r}\pm\vec{d}/2|^2+\phi_{\pm}}, \tag{4.2}$$

where $\pm$ denotes one well or the other, $n_{\pm}$ is the condensate density, m is the atomic mass, $\vec{d}$ is a vector connecting the two wells, and $\phi_{\pm}$ is the condensate phase. Interactions between the two condensates during ballistic expansion have been neglected.

The total density profile for the matter wave interference pattern takes the form

$$n(\vec{r},t) = \left[n_+ + n_- + 2\sqrt{n_+ n_-}\cos\left(\frac{md}{\hbar t}x + \phi_r\right)\right], \tag{4.3}$$

where $\phi_r = \phi_+ - \phi_-$ is the relative phase between the two condensates and $\vec{d} = d\hat{x}$. To extract ϕ_r, an integrated cross section of the matter wave interference pattern [Fig. 4-2(b)] was fit with a sinusoidally-modulated Gaussian curve,

$$G(x) = Ae^{-(x-x_c)^2/\sigma^2}\left[1 + B\cos\left(\frac{2\pi}{\lambda}(x-x_0) + \phi_f\right)\right], \tag{4.4}$$

where ϕ_f is the phase of the interference pattern with respect to a chosen fixed x_0. Ideally, if x_0 was set at the center of the two wells, then $\phi_r = \phi_f$. However, misalignment of the imaging axis with the direction of gravitational acceleration created a constant offset, $\phi_f = \phi_r + \delta\phi$. With $t = 30$ ms the measured fringe period, $\lambda = 41.5$ μm, was within 4% of the point source formula prediction (Eq. 4.3), $ht/md = 39.8$ μm.

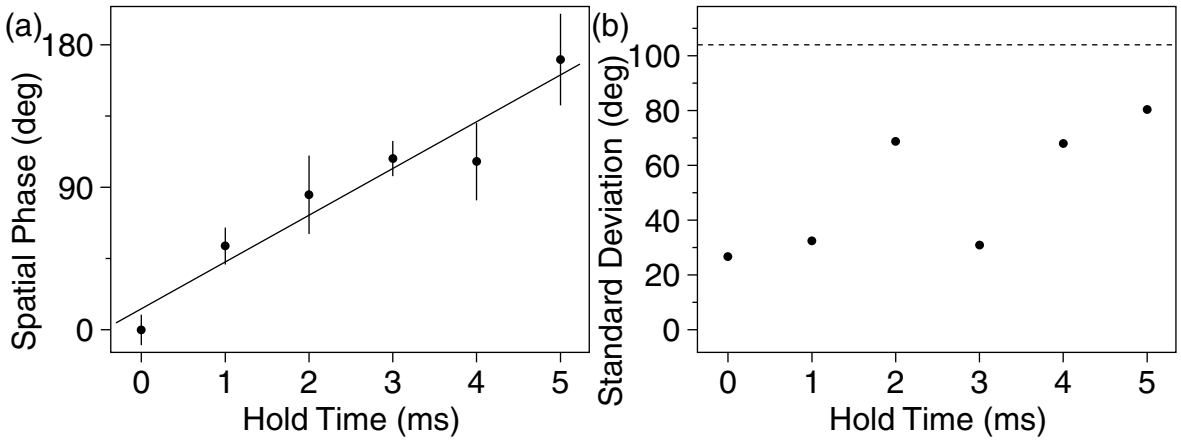

Figure 4-3: Phase coherence of separated condensates. (a) The spatial phase of the matter wave interference pattern is plotted vs hold time after splitting. Each data point represents the average of eight measurements. The phase evolution was due to unequal trap depths for the two wells, which was determined from the linear fit to be $h \times 70$ Hz or $\sim 1\%$ of the trap depth. (b) The standard deviation of the eight measurements averaged in (a) is plotted vs hold time after splitting. This represents the uncertainty in a single phase measurement. The error bars in (a) are $\sqrt{8}$ times smaller. A random distribution of phases between -180 and $+180$ degrees would have a standard deviation of ~ 104 degrees (dashed line).

4.2.2 Phase Coherence

The relative phase between the separated condensates was observed to evolve linearly in time [Fig. 4-3(a)]. This evolution was mainly caused by a difference in trap depths between the two wells, although a slight mean field energy difference between the two condensates contributed also.

The standard deviation of eight measurements of ϕ_r was < 90 degrees for condensates split then held separated for up to 5 ms [Fig. 4-3(b)]. Furthermore, for hold times up to 1 ms, the standard deviation was substantially smaller, < 40 degrees. Since a random distribution of phases between -180 and $+180$ degrees would have a standard deviation of ~ 104 degrees, the measured results quantitatively confirm the reproducible nature of the splitting process and the coherent evolution of the separated condensates.

Fundamental limits on the phase coherence between isolated condensates arise due to Poissonian number fluctuations associated with the splitting process and the

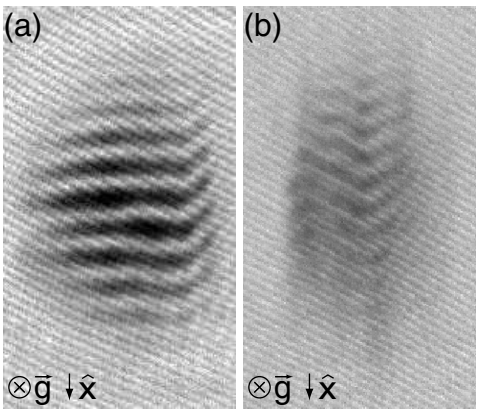

Figure 4-4: Decoherence. Absorption images of condensates released from the double-well potential and allowed to overlap during 30 ms ballistic expansion. After splitting, the condensates were held separated for (a) 0 ms [Fig. 4-2(a)] and (b) 8 ms. The spatial phase of the matter wave interference pattern could be reliably extracted from (a) but not (b). The imaging axis was parallel to the direction of gravitational acceleration, $\vec{g}$. The field of view in (a) and (b) is 600 μm $\times$ 350 μm.

coherent state description of the condensate [100, 131, 143]. For condensate number fluctuations $\Delta N = \sqrt{N}$, the corresponding variation in the atomic mean field energy is

$$\Delta\mu = \frac{2}{5}\frac{\mu}{\sqrt{N}} \tag{4.5}$$

where $\mu \propto N^{2/5}$ in the Thomas-Fermi limit (Ch. 1, Eq. 1.6). For our parameters ($N \approx 10^5$ and $\mu \approx h \times 3$ kHz), $\Delta\mu \approx h \times 4$ Hz. This sets the times scale for phase diffusion to be ~ 250 ms.

Repulsive atom-atom interactions may lead to relative number squeezing between the condensates in the two wells and extend the phase diffusion time [222, 223]. Also, weak Josephson coupling between the two wells may counteract phase diffusion (Sec. 4.4).

The uncertainty in determining ϕ_r at hold times > 5 ms was attributed to axial and breathing-mode excitations created during the splitting process. These excitations led to interference fringes that were angled and had substantial curvature, rendering a determination of ϕ_r impossible (Fig. 4-4). Splitting the condensate more slowly in an effort to minimize excitations, but still fast compared to the phase diffusion time,

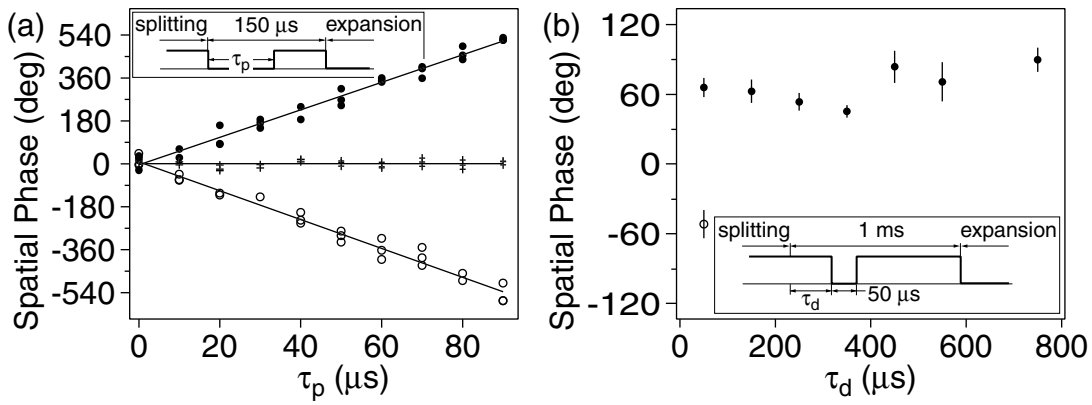

Figure 4-5: Trapped-atom interferometry. (a) ac Stark phase shifts were applied to either well exclusively (solid circles and open circles) or both wells simultaneously (crosses) by turning off the corresponding rf signal(s) driving the AOM for a duration τ_p. The resulting spatial phase of the matter wave interference pattern scaled linearly with τ_p and hence the applied phase shift. Applying the ac Stark shift to the opposite well (solid vs open circles) resulted in an interference pattern phase shift with opposite sign. Applying ac Stark shifts to both wells (crosses) resulted in no phase shift for the interference pattern. This data was taken with a slightly modified experimental setup such that the trap depth of the individual potential wells was $U_0 = h \times 17$ kHz. (b) A 50 μs pulse induced a ~ 70 degree shift independent of the pulse position. The experimental setup was as described in Fig. 4-1. Solid and open circles have the same meaning as in (a). The insets show the time sequence of the optical intensity for the well(s) temporarily turned off.

did not improve the measured stability of ϕ_r. Since controlling axial excitations appears critical for maintaining phase coherence, splitting condensates that are freely propagating in a waveguide potential may be more promising (Ch. 3). In addition, propagating the separated condensates along a waveguide prior to phase readout would create an atom interferometer with an enclosed area, and hence with rotation sensitivity.

4.3 Trapped-Atom Interferometry

The phase sensitivity of the trapped-atom interferometer was demonstrated by applying ac Stark phase shifts to either (or both) of the two separated condensates. Phase shifts were applied to individual condensates by pulsing off the optical power

generating the corresponding potential well for a duration $\tau_p \ll 1/\omega_r$. The spatial phase of the matter wave interference pattern shifted linearly with the pulse duration [Fig. 4-5(a)]. Due to the inhomogeneous optical potential, $U(\vec{r})$, the applied ac Stark phase shifts varied across the condensate as $\Delta\phi(\vec{r}) = -U(\vec{r})\tau_p/\hbar$. Averaging this phase shift over the inhomogeneous condensate density, $n(\vec{r})$, approximates the expected spatial phase shift of the matter wave interference pattern as

$$\Delta\bar{\phi} = \frac{1}{N}\int d^3\vec{r}\; n(\vec{r})\Delta\phi(\vec{r}), \tag{4.6}$$

$$= \left(U_0 - \frac{2}{7}\mu\right)\tau_p/\hbar, \tag{4.7}$$

where $N = \int d^3\vec{r}\; n(\vec{r})$ is the number of condensate atoms, U_0 is the potential well depth, and μ is the atomic mean field energy. The measured phase shifts yielded $U_0 = h \times 5$ kHz [Fig. 4-5(b)], which was consistent with calculations based on the measured trap frequencies.

4.4 Josephson Coupling

The condensates were sufficiently separated that their phases evolved independently of each other to the extent that no coupling between the potential wells could be detected. This claim is supported qualitatively by our ability to cleanly resolve the separated, trapped condensates with absorption imaging techniques [Fig. 4-1(a)] and by the observation of high-contrast matter wave interference patterns that penetrated the full atomic density profile with uniform spatial period and no thick central fringe [Fig. 4-2(a)] [183].

Estimating the expected Josephson coupling between the two separated wells is difficult because tunnelling depends exponentially on the barrier height and well separation [44]. In the weak coupling limit, we expect a small population imbalance between the two wells to oscillate at the Josephson plasma frequency $\omega_{JP} = \sqrt{\omega_J\mu/\hbar}$, where ω_J is the single particle tunnelling rate and μ is the atomic mean field energy [201, 220]. The maximum population imbalance can be estimated as the total

number of particles that tunnel between the two wells in one Josephson period [220]:

$$\Delta N \approx \frac{N\omega_J}{\omega_{JP}} \approx N\sqrt{\frac{\omega_J}{\mu/\hbar}}. \tag{4.8}$$

The single particle tunnelling rate is given by

$$\omega_J = \omega_r e^{-\int dx \sqrt{\frac{2m[U(x)-\mu]}{\hbar^2}}}, \tag{4.9}$$

where ω_r is the radial trap frequency, $U(x)$ is the double-well potential [Fig. 4-1(c)], and the integration is over the classically forbidden region.

For our parameters, $\omega_J \approx \omega_r e^{-14} \approx 2\pi \times 5 \times 10^{-4}$ Hz. For $N = 10^5$ atoms in each well at an atomic mean field energy $\mu = h \times 3$ kHz, we expect $\Delta N \approx 400$ atoms ($\Delta N/N = 4\times10^{-3}$) to oscillate between the two wells at a frequency $\omega_{JP} \approx 2\pi\times1$ Hz. Thus, on the time scale of our experiment (a few milliseconds), we do not expect to observe the effects of Josephson coupling.

Quantitatively, the lack of coupling between the two separated condensates was verified by measuring the evolution of their relative phase (Figs. 4-3 and 4-5). The measured phase shifts of the matter wave interference depended only on the time-integral of the applied ac Stark phase shifts [Fig. 4-5(b)]. This is expected for uncoupled condensates since the final relative phase, ϕ_r, should be the same on different phase trajectories because the history of phase accumulation does not affect the total amount of accumulated phase. In constrast, in the presence of Josephson coupling the small population imbalance oscillating between the two wells would cause the relative phase between the two condensates to oscillate and produce a time dependent signal in Fig. 4-5(b).

Chapter 5

Vortices and Spin Textures

Shortly after the 1938 discovery of superfluidity in liquid ^{4}He [2, 103], the phenomenon of Bose-Einstein condensation was resurrected from its fate as an obscure theoretical subtlety and used to explain the experimental findings [133, 134, 210]. In this treatment, the superfluid (condensate) fraction was distinguished from the normal (thermal) fraction by a macroscopic, scalar order parameter, $|\psi(\vec{r})\rangle = \sqrt{n(\vec{r})}e^{iS(\vec{r})}$, where $n(\vec{r})$ is the superfluid density.

In such a system, the superfluid velocity can be expressed as $\vec{v}_s(\vec{r}) = -(\hbar/m)\nabla S(\vec{r})$, where m is the atomic mass. Due to the single-valued nature of the condensate order parameter, circulation in a superfluid is quantized:

$$\oint \vec{v}_s \cdot d\vec{\ell} = \kappa \frac{h}{m},\ \kappa = 0,\ \pm 1,\ \pm 2 \ldots \tag{5.1}$$

One ramification of Eq. 5.1 is that when a superfluid is rotated, angular momentum enters the system through quantized vortices. In spin-less or spin-polarized condensates, line defects such as vortices have cores where the density of condensed particles is necessarily zero to keep the order parameter single-valued [1, 78, 92, 123, 137, 224]. In Eq. 5.1, κ is known as the "winding number" or "charge" of the vortex state and represents the angular momentum per particle in units of $\hbar$.

Topological defects in superfluid systems described by vector order parameters can be more complex. In condensates with a spin degree of freedom, coreless vortices exist

as spin textures [18, 126, 141]. Such structures are referred to as skyrmions (Anderson-Toulouse vortices [7]) or merons (half-skyrmions, Mermin-Ho vortices [145]) depending on the boundary conditions of the system[1]. Spin textures play a central role in describing the physics of elementary particles [200], liquid ^{3}He-A [7, 18, 145], the quantum Hall effect [127], and gaseous Bose-Einstein condensates [91, 114, 115, 160, 225].

Superfluid phenomena become apparent when phase gradients and windings are established. In contrast to liquid helium systems, experimental control over gaseous Bose-Einstein condensates allows vortex and spin texture phase factors to be directly written onto the condensate wavefunction [123, 126, 141]. Such phase windings can be imprinted onto the condensate wavefunction either dynamically or topologically. Dynamically, the phase of the condensate evolves according to the time integral of its energy, which can be tailored locally with a spatially varying external potential. Topologically, the phase of the condensate advances through adiabatic variations in the parameters of the Hamiltonian governing the system. This phase, which is solely a function of the path traversed by the system in the parameter space of the Hamiltonian, is known as Berry's phase [17].

Vortices have been generated in single-component condensates by rotating the cloud with an anisotropic potential [1, 78, 92, 137], by slicing through the cloud with a perturbation above the critical velocity of the condensate [1, 96], and through the decay of solitons [4, 55]. Engineering topological states in a Bose-Einstein condensate has received much theoretical attention [98, 130, 140, 176, 186, 187, 221]. In spinor condensates, vortices and spin textures have been phase-imprinted by driving spatially selective spin-flip transitions [141] and adiabatic magnetic field variations [123, 126]. This chapter describes vortices and spin textures imprinted in spinor condensates using topological phases and expands on the work presented in Refs. [123] (App. D) and [126] (App. E).

^{23}Na condensates were prepared in either the lower, $|1,-1\rangle$, or upper, $|2,+2\rangle$, hyperfine state and confined in a Ioffe-Pritchard magnetic trap. We created vor-

[1]Originally, the term "skyrmion" referred to three-dimensional point-like topological defects [114, 115, 200]. However, it is common to use this term when describing two-dimensional line defects as well [91].

tices by adiabatically inverting the magnetic bias field along the trap axis and could remove them by returning the bias field to its original direction. Using surface wave spectroscopy [32, 77, 226], the axial angular momentum per particle of the $|1,-1\rangle$ and $|2,+2\rangle$ vortex states was measured to be consistent with $-2m_F\hbar$, as predicted [98, 152, 157, 159].

The field inversion process can be decomposed into two steps. First, the axial bias field is adiabatically reduced to zero. Then second, it is adiabatically increased in the opposite direction. While the axial bias field was zero, spin textures with Mermin-Ho [145] boundary conditions were produced. These spin textures were detected as coreless vortices in $F = 1$ spinor condensates. Reducing the axial bias field to zero continuously transformed the initially spin-polarized condensate into a coherent superposition of three spin states, each with a different phase winding. The resulting angular momentum per particle varied between spin states, and the condensate evolved such that states with more angular momentum per particle circulated around (i.e. at a larger radius than) states with less angular momentum per particle. Thus, the condensate had a net axial magnetization that varied with radial position.

5.1 Phase Imprinting

The spin-F condensate wavefunction can be written as $|\psi(\vec{r})\rangle = \sqrt{n(\vec{r})}|\zeta(\vec{r})\rangle$, where $n(\vec{r})$ is the atomic number density and the $2F+1$ component spinor

$$|\zeta(\vec{r})\rangle = \sum_{m_z=-F}^{F} \zeta_{m_z}(\vec{r})|F, m_z\rangle,\ |\langle\zeta(\vec{r})|\zeta(\vec{r})\rangle|^2 = 1 \tag{5.2}$$

describes a spin texture.

A Ioffe-Pritchard magnetic trap consists of an axial bias field (with curvature) and a two-dimensional quadrupole field in the orthogonal plane [68, 174]. Taking the z axis as the symmetry axis, the magnetic field profile of a Ioffe-Pritchard trap has

the form

$$\vec{B}(\vec{r}) = B_z\hat{z} + B'\left(x\hat{x} - y\hat{y}\right), \tag{5.3}$$

$$= B_z\hat{z} + B'r\left[\cos(2\phi)\hat{r} - \sin(2\phi)\hat{\phi}\right], \tag{5.4}$$

in Cartesian and cylindrical coordinates, respectively. $B' > 0$ is the radial magnetic field gradient and quadratic terms have been neglected. The local magnetic field is nearly parallel to the z axis throughout a condensate of radial extent R confined in a Ioffe-Pritchard magnetic trap with $B_z \gg B'R > 0$. Accordingly, the condensate spinor in the lab frame can be approximated by $|\zeta(\vec{r})\rangle = |F, m_z = +m_F\rangle$, where m_z and m_F are the projection of the atomic spin, $\vec{F}$, along the z axis and local magnetic field direction, respectively.

Adiabatically varying B_z rotates the local magnetic field direction and hence the atomic spins. This establishes a spatially dependent phase across the condensate because the spins rotate about a unit vector $\hat{n}(\phi) = \sin(\phi)\hat{x} + \cos(\phi)\hat{y}$ that depends on the azimuthal angle, ϕ, describing the atomic position [Fig. 5-1(a)]. The position dependent phase imprinted onto the condensate wavefunction can be calculated by applying the quantum mechanical rotation operator

$$|\zeta(\vec{r})\rangle = e^{-i(\vec{\mathcal{F}}/\hbar)\cdot\hat{n}(\phi)\beta(r)}|F, m_z = +m_F\rangle, \tag{5.5}$$

where $\vec{\mathcal{F}}$ is the spin operator such that $\vec{F} = \langle\zeta(\vec{r})|\vec{\mathcal{F}}|\zeta(\vec{r})\rangle$ and $\beta(r)$ is the angle through which $\vec{F}$ rotated about the $\hat{n}(\phi)$ axis.

This chapter considers two limiting cases for the variation of B_z: $B_z \to -B_z$ (Sec. 5.2) and $B_z \to 0$ (Sec. 5.3).

5.2 Vortex Formation and Detection

Inverting $B_z \to -B_z$ rotates all atomic spins by π radians and produces spin-polarized condensates with vortices. From Eq. 5.5 with $\beta(r) = \pi$, the condensate spinor in the

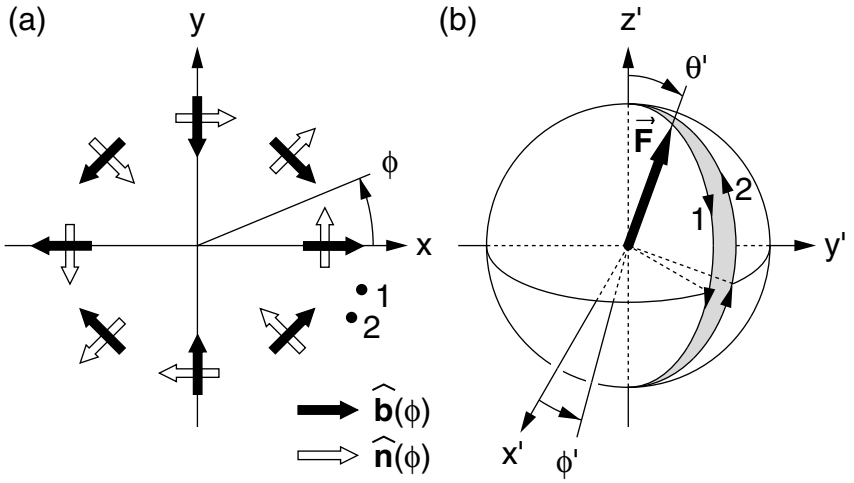

Figure 5-1: Spin rotation and Berry's phase. (a) The unit vectors $\hat{b}(\phi)$ (filled arrows) point in the direction of the two-dimensional quadrupole field providing the radial confinement of a Ioffe-Pritchard magnetic trap. The atomic spins rotate about the unit vectors $\hat{n}(\phi)$ (open arrows) as the axial bias field, B_z, is ramped from positive to negative values. (b) The spin, $\vec{F}$, for an atom in state $|F, m_F\rangle$ traverses a path on a sphere of radius $|m_F|\hbar$ as it adiabatically follows its local magnetic field. The primed coordinate system is centered on the atomic position and has axes parallel to those of the unprimed coordinate system in (a). For an atomic position described by the azimuthal angle ϕ, $\vec{F}$ rotates in a half-plane defined by $\phi' = -\phi$ for $m_F > 0$ and $\phi' = -\phi + \pi$ for $m_F < 0$ as B_z is inverted. After inverting B_z, the relative topological phase acquired between atoms located at positions 1 and 2 in (a) is proportional to the solid angle subtended by the shaded surface, bounded by the contour marked with arrowheads (see text).

lab frame after inverting B_z is

$$|\zeta(\vec{r})\rangle = e^{-i(\vec{\mathcal{F}}/\hbar)\cdot\hat{n}(\phi)\pi}|F, m_z = +m_F\rangle, \tag{5.6}$$

$$= (-1)^{F-m_F} e^{-i2m_F\phi}|F, m_z = -m_F\rangle. \tag{5.7}$$

The topological phase factor $e^{-i2m_F\phi}$ describes a vortex of winding number $2|m_F|$ with the sense of rotation dependent on the sign of m_F. The phase singularity (angular momentum barrier) at $r = 0$ requires $n(0) = 0$. The minimum length scale over which

the condensate density can vary is the healing length[2,3], $\xi = 1/\sqrt{8\pi na}$, where a is the s-wave scattering length for a binary collision. Accordingly, the density depletion at the vortex core has a radius of order $\xi = 750$ nm for a background condensate density $n = 10^{14}$ atoms/cm^3. The vortex core size also scales with the winding number of the vortex state [29].

5.2.1 Berry's Phase

The result in Eq. 5.7 can be interpreted in terms of Berry's phase [159]. Figure 5-1(b) shows the orientation of $\vec{F}$ in the lab frame for $m_F > 0$. Atoms located at position $k = 1, 2$ in Fig. 5-1(a) have azimuthal angle ϕ_k and angular momentum $\vec{F}_k$. As B_z is inverted, $\vec{F}_k$ traces path k from top to bottom on the sphere in Fig. 5-1(b). The topological phase acquired by an atom in this process is solely a function of the path traversed by its angular momentum vector. Since this path depends on the azimuthal angle describing the atomic position, a relative phase is established between spatially separated atoms. The condensate spinor after inverting B_z is given by

$$|\zeta(\vec{r})\rangle = e^{i\gamma(\phi)}|F, m_F\rangle, \tag{5.8}$$

where $\gamma(\phi)$ is the topological phase acquired by atoms with azimuthal angle ϕ.

For an atom in state $|F, m_F\rangle$, Berry's phase, $\gamma(C)$, acquired as its angular momentum vector traverses a closed contour, C, on the surface of the sphere in Fig. 5-1(b) is given by [17]

$$\gamma(C) = -m_F\Omega(C), \tag{5.9}$$

where $\Omega(C)$ is the solid angle subtended by a surface bounded by the contour C. Calculating the relative phase, $\gamma(\phi_1) - \gamma(\phi_2)$, with the aid of Eq. 5.9 requires closing the contours traced by each $\vec{F}_k$ along an identical path. For clarity, we choose to close each contour along path 2 itself and hence $\gamma(\phi_1) - \gamma(\phi_2) = \gamma(C)$, where C is the

[2]In the liquid helium community, this length scale is referred to as the coherence length. However, in the BEC community, the coherence length is typically reserved to describe the length scale over which the condensate can be described by a single phase [9, 50, 76, 83, 181, 203].

[3]Refs. [42, 128, 166, 169] define $\xi = 1/\sqrt{8\pi na}$ while Refs. [67, 170, 171] define $\xi = 1/\sqrt{4\pi na}$.

contour formed by path 1 traversed from top to bottom and path 2 traversed from bottom to top, as indicated with arrowheads in Fig. 5-1(b).

A surface bounded by this contour subtends a solid angle $\Omega(C) = 2(\phi_1 - \phi_2)$, yielding a relative phase $\gamma(\phi_1) - \gamma(\phi_2) = -2m_F(\phi_1 - \phi_2)$. Thus, we make the assignment

$$\gamma(\phi) = -2m_F\phi, \tag{5.10}$$

up to an additive term independent of position. This is the same phase as in Eq. 5.7 reinterpreted in terms of Berry's phase.

5.2.2 $F = 1$ and $F = 2$ ^{23}Na Condensates

Condensates in the $|F = 1, m_F = -1\rangle$ state containing up to 3×10^6 atoms were delivered to the science chamber using optical tweezers (Ch. 2). While optically confined by the tweezers, condensates were prepared in the $|2, +2\rangle$ state by sweeping through the $|1, -1\rangle \leftrightarrow |1, 0\rangle \leftrightarrow |1, +1\rangle$ radio-frequency transition with 100% efficiency, then sweeping through the $|1, +1\rangle \leftrightarrow |2, +2\rangle$ microwave transition with 80% efficiency [66]. In the science chamber, the condensate was loaded into a microfabricated Ioffe-Pritchard magnetic trap formed by a Z-shaped wire carrying current I and an external magnetic bias field, $B_\perp$ (Ch. 3, Figs. 3-4 and 3-5). An axial bias field, $B_z = B_{||}$, was applied to make the radial confinement harmonic and prevent non-adiabatic spin-flip transitions.

Typical magnetic microtrap parameters were $I = 1200$ mA, $B_\perp = 5.4$ G, and $B_z \approx 1$ G, resulting in a radial magnetic field gradient of $B' = 120$ G/cm. For atoms in the $|1, -1\rangle$ state, the axial and radial trap frequencies were $\omega_z = 2\pi \times 6$ Hz and $\omega_\perp = 2\pi \times 210$ Hz, respectively. For atoms in the $|2, +2\rangle$ state, the microtrap frequencies (for identical magnetic field parameters) were larger by a factor of $\sqrt{2}$ due to the larger magnetic moment. After transfer into the microtrap, condensates in the $|1, -1\rangle$ ($|2, +2\rangle$) state contained $\sim 2 \times 10^6$ atoms ($\sim 1 \times 10^6$ atoms) and had a lifetime > 10 s (> 3 s). This represented the first magnetic trapping of ^{23}Na condensates in the upper hyperfine level, with previous work done exclusively in optical dipole traps [66].

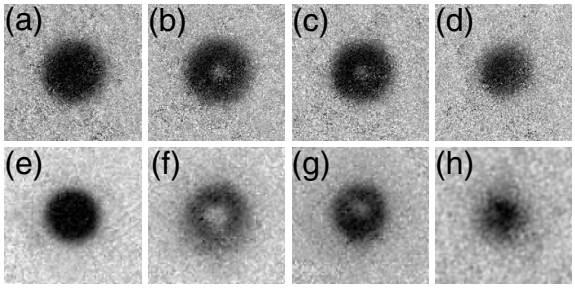

Figure 5-2: Vortices in $F = 1$ and $F = 2$ condensates. Axial absorption images of condensates in the $|1, -1\rangle$ state after 18 ms ballistic expansion (a) prior to inverting B_z, after inverting B_z and holding the trapped condensate for (b) 5 ms and (c) 20 ms, and (d) after inverting B_z and then returning it to its original direction. Axial absorption images of condensates in the $|2, +2\rangle$ state after 7 ms ballistic expansion (e) prior to inverting B_z, after inverting B_z and holding the trapped condensate for (f) 0 ms and (g) 5 ms, and (h) after inverting B_z and then returning it to its original direction. The field of view is (a)-(d) 570 μm $\times$ 570 μm and (e)-(h) 285 μm $\times$ 285 μm.

Subsequently, ^{23}Na condensates have been created by direct evaporation in the $|2, +2\rangle$ state [75].

5.2.3 Observation of Vortex Cores

Vortices were created in condensates held in a Ioffe-Pritchard magnetic trap by inverting B_z and could be removed by returning B_z to its original direction (Fig. 5-2). The vortices were observed by releasing the trapped condensate and allowing the atoms to expand ballistically. They were identified by central density depletions due to the angular momentum barrier associated with a rotating cloud. In the trapped condensate, the vortex core size was too small ($\sim \xi$) to be resolved optically. However, ballistic expansion for a time τ from a trap with frequencies $\omega_z \ll \omega_\perp$ radially magnified the condensate wavefunction, including the vortex core size, by a factor $\sqrt{1 + \omega_\perp^2 \tau^2}$ [28, 43, 135]. This made the vortex cores large enough to be unambiguously detected with standard absorption imaging techniques.

For condensates in the $|1, -1\rangle$ state, the best results were achieved by inverting the axial bias field linearly from $B_z = 860$ mG to -630 mG in 11 ms. For atoms in the $|2, +2\rangle$ state, the optimum ramp time over the same range was 4 ms. The field

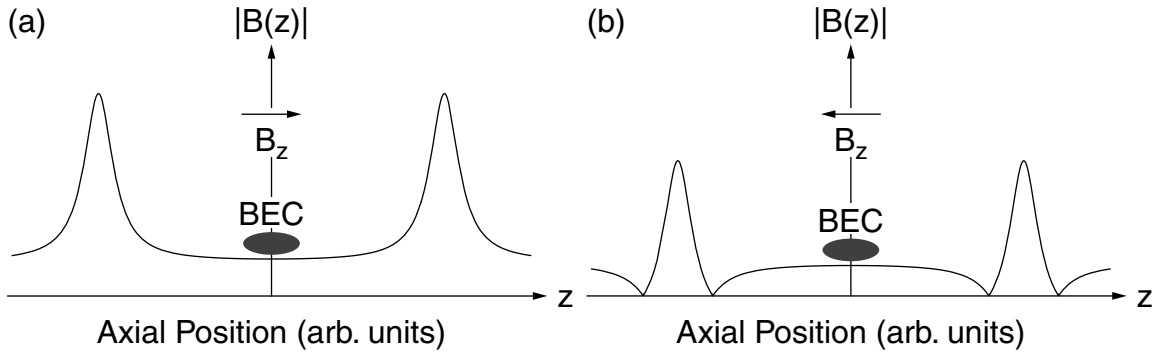

Figure 5-3: Axial magnetic field. The Z-wire (Ch. 3, Fig. 3-4) trapping potential along the z axis is proportional to the magnitude of the axial magnetic field shown (a) before inverting B_z and (b) after inverting B_z.

inversion process caused an atom loss of $\sim 50\%$ due to non-adiabatic spin flips as B_z passed through zero, in reasonable agreement with calculations in Refs. [152, 159]. The density depletions shown in Figs. 5-2(b), 5-2(c), and 5-2(g) were observed after inverting the axial bias field and holding the trapped condensate for longer than a radial trap period. Thus, the atom loss from the center of the cloud during the field inversion process could not be responsible for the observed density depletions. Typical $|1,-1\rangle$ ($|2,+2\rangle$) condensates after inverting the axial bias field contained up to 1×10^6 atoms (0.5×10^6 atoms) with a Thomas-Fermi radius $R_{TF} = 5.4 \pm 0.2$ μm ($R_{TF} = 4.5 \pm 0.2$ μm) in a trap with radial frequency $\omega_\perp = 2\pi \times 250$ Hz ($\omega_\perp = 2\pi \times 350$ Hz).

The magnetic field along the microtrap axis was

$$\vec{B}(r=0,z) = \left(B_z + \frac{1}{2}B''z^2\right)\hat{z}, \tag{5.11}$$

where quadratic terms neglected in Eqs. 5.3 and 5.4 have been included. The axial magnetic field curvature, B'', which arose from the geometry of the Z-wire, was held constant throughout the experiment. B_z was inverted by reversing an external axial magnetic field. Changing the sign of B_z, but not B'', resulted in a magnetic field saddle point at the center of the cloud and axial anti-trapping of weak-field seeking atoms (Fig. 5-3). This limited the condensate lifetime after inverting B_z to < 50 ms. Radial excitations caused by the field inversion process may also have limited the

condensate lifetime.

5.2.4 Angular Momentum Measurements

The axial angular momentum per particle of the vortex states was measured using surface wave spectroscopy [32, 77, 226]. A superposition of counter-rotating ($m_\ell = \pm 2$) quadrupolar ($\ell = 2$) surface waves was excited in the condensate[4], where ℓ and m_ℓ characterize the angular momentum and its projection along the z axis of the quadrupole modes, respectively. This created an elliptical condensate cross section with time dependent eccentricity. In the absence of a vortex, the $m_\ell = \pm 2$ quadrupole modes are degenerate and the axes of the elliptical condensate cross section remain fixed in time. This degeneracy is lifted by the presence of a vortex, causing the axes to precess in the direction of fluid flow. The precession rate, $\dot{\Theta}$, is given by [32, 77, 226]

$$\dot{\Theta} = \frac{\langle L_z \rangle}{2m\langle r_\perp^2 \rangle} \ , \tag{5.12}$$

where $\langle L_z \rangle$ is the axial angular momentum per particle characterizing the vortex state, m is the atomic mass, and $\langle r_\perp^2 \rangle = \langle x^2 + y^2 \rangle$ is the mean-squared trapped condensate radius with vortices present.

By measuring the precession rate of the quadrupole axes and the mean-squared radius of the condensate in the trap, the axial angular momentum per particle was determined. After exciting the quadrupolar modes, the condensate evolved in the trap for variable times in the range $0.2 - 7.4$ ms. The condensate was then released from the trap and imaged with resonant laser light after ballistic expansion [Figs. 5-4(a)-5-4(l)]. The resulting images were fit to an elliptical Thomas-Fermi profile to determine the orientation of the quadrupole axes as a function of time [Fig. 5-4(m)].

To determine the mean-squared trapped condensate radius, vortices were imprinted in the condensate but quadrupolar modes were not excited. Images of ballistically expanded condensates similar to those in Figs. 5-2(b), 5-2(c), 5-2(f), and

[4]The surface waves were excited by vertically displacing the magnetic trap center for 200 μs. This compressed the condensate vertically due to anharmonic terms in the microtrap potential and created an elliptical condensate cross section.

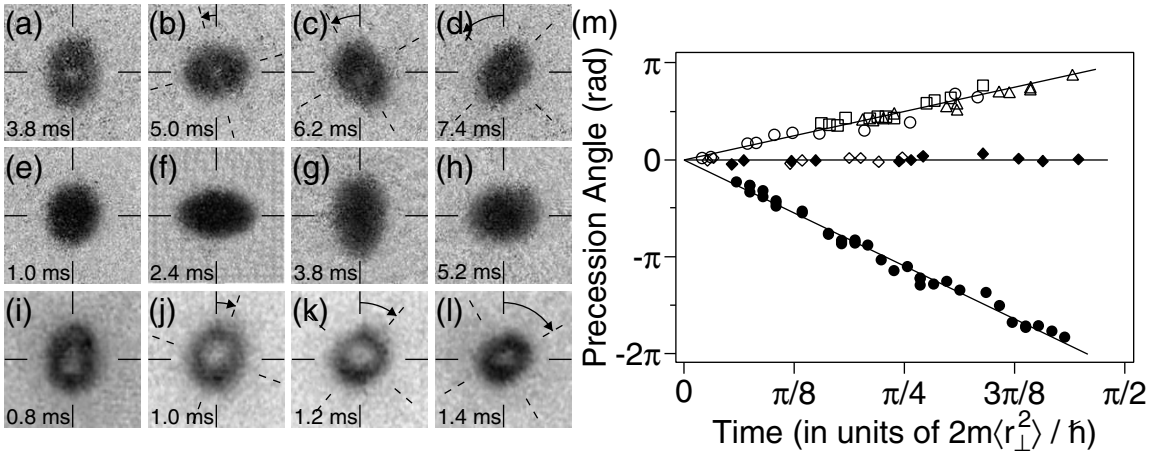

Figure 5-4: Surface wave spectroscopy. Axial absorption images after 18 ms ballistic expansion of $|1,-1\rangle$ condensates undergoing a quadrupole oscillation (a)-(d) in the presence of a vortex and (e)-(h) in the absence of a vortex. Successive images were taken during successive half periods of the quadrupole oscillation such that the short and long axes of the elliptical cross section were exchanged. Images (a)-(d) show counter-clockwise (positive) precession of the quadrupole axes, while images (e)-(h) show no precession. (i)-(l) Axial absorption images after 7 ms ballistic expansion of $|2,+2\rangle$ condensates undergoing a quadrupole oscillation in the presence of a vortex. The images were taken during a single half period of the quadrupole oscillation. Images (i)-(l) show clockwise (negative) precession of the quadrupole axes. The field of view is (a)-(h) 570 μm $\times$ 570 μm and (i)-(l) 285 μm $\times$ 285 μm. (m) Precession angle vs time in the presence of a vortex for $|1,-1\rangle$ condensates measured after a delay of 0 ms (open circles), 5 ms (open squares), and 20 ms (open triangles) from the completion of the inversion of the axial bias field, in the absence of a vortex for $|1,-1\rangle$ (open diamonds) and $|2,+2\rangle$ (filled diamonds) condensates, and in the presence of a vortex for $|2,+2\rangle$ condensates measured immediately upon the completion of the inversion of the axial bias field (filled circles).

5-2(g) were fit to a Thomas-Fermi profile with a circular cross section. The fitting routine ignored the central region of the cloud where the density was depleted due to the vortex core. The mean-squared trapped condensate radius was derived through the relation

$$\langle r_\perp^2 \rangle = \frac{2}{7} \frac{R_\perp^2}{1+\omega_\perp^2 \tau^2}, \tag{5.13}$$

where $R_\perp$ is the Thomas-Fermi radius of the condensate after ballistically expanding for a time τ from a trap with radial frequency $\omega_\perp$. The factor $1+\omega_\perp^2\tau^2$ accounts for the change in Thomas-Fermi radius during the expansion process [28] and the factor

2/7 results from averaging over the inhomogeneous condensate density distribution assuming no vortices are present. For low angular momentum vortex states, the density depletion at the vortex core does not significantly modify the density distribution of the condensate and we expect the 2/7 factor to still be accurate [42].

For condensates in the $|1,-1\rangle$ state, the quadrupole oscillation was excited after a delay of 0 ms, 5 ms, and 20 ms from the completion of the inversion of the axial bias field. The measured axial angular momenta per particle were $(+1.9 \pm 0.3)\hbar$, $(+2.1 \pm 0.3)\hbar$, and $(+1.9 \pm 0.2)\hbar$, respectively. For condensates in the $|2,+2\rangle$ state, the quadrupole oscillation was excited immediately upon the completion of the inversion of the axial bias field. The measured axial angular momentum per particle was $(-4.4 \pm 0.4)\hbar$. For both internal states, the measurements were consistent with the predicted axial angular momentum per particle of $-2m_F\hbar$ [98, 152, 157, 159]. The uncertainty in the measurements arises from the linear fit to the precession angle and the determination of $\langle r_\perp^2 \rangle$.

5.2.5 Multiply Charged Vortices

Multiply charged vortices are unstable against decay into multiple, singly charged vortices [29, 153, 158, 184]. From our experiments, we cannot determine if the condensate contained one multiply charged vortex or multiple, singly charged vortices. If multiple vortices were present, they must be closely spaced since they were not resolved after ballistic expansion. Furthermore, if the singly charged vortices had moved apart considerably, it would have lowered the extracted value of $\langle L_z \rangle$ [32], which was not observed even with delayed probing.

It is predicted that doubly charged vortices should decay into two singly charged vortices that are intertwined [153]. Imaging along the vortex axis and/or measuring the angular momentum per particle of the vortex states does not efficiently differentiate between a doubly charged vortex and a pair of intertwined, singly charged vortices. However, imaging perpendicular to the vortex axis may reveal such a decay (Fig. 5-5).

Our work represented the first observation of vortices with a single density deple-

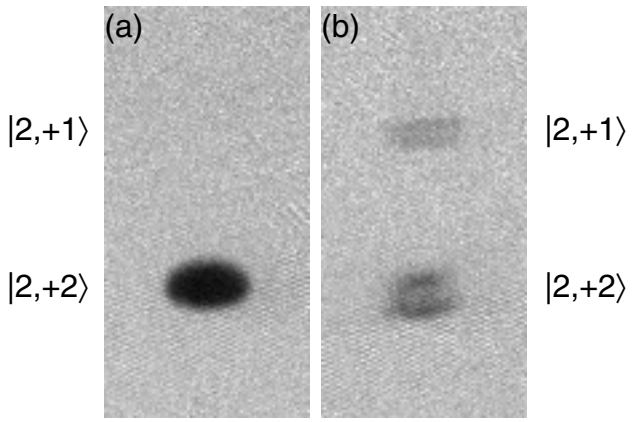

Figure 5-5: Vortex line. Absorption images of a condensates in the $|2,+2\rangle$ state after ballistic expansion (a) before and (b) after imprinting a vortex as described in Sec. 5.2. The imaging light propagated perpendicular to the condensate/vortex axis such that the vortex core appears as a line defect running along the entire length of the condensate. Ballistic expansion was initiated immediately after creating the vortex state. A magnetic field gradient was applied during ballistic expansion to spatially separate the remaining spin states. Spin-flip transitions to untrapped states during the phase imprinting process led to trap loss. Spin-flip transitions to the $|2,+1\rangle$ state, which is weak field seeking and remained radially confined by the magnetic trap, were directly observed as predicted in Ref. [152].

tion, but multiple (2 or 4) phase windings. Subsequently, long-lived vortex aggregates with a single density depletion and $7-60$ phase singularities have been observed [57].

Multiply charged vortices are stable in a multiply connected geometry such as a torus. This geometry can be realized by applying a repulsive potential along the vortex line with a blue-detuned laser beam [46, 98].

5.3 Coreless Vortex Formation and Detection

Section 5.2 described the formation of vortices in condensates confined in a Ioffe-Pritchard magnetic trap by inverting $B_z \rightarrow -B_z$. During this process, the axial bias field passed through zero. This section considers the nature of the system when $B_z \approx 0$.

For condensates confined in a Ioffe-Pritchard magnetic trap, adiabatically ramping

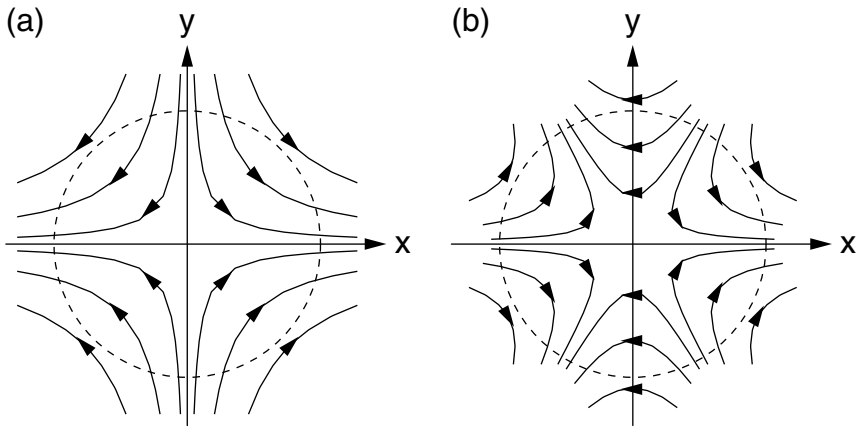

Figure 5-6: Planar spin textures. Spins aligned with two-dimensional (a) quadrupole and (b) hexapole magnetic fields produce textures with winding numbers -1 and -2, respectively. Counter-clockwise traversal of the dashed contours in (a) and (b) leads to clockwise (negative) spin rotation, with the winding number defined as the integer number of revolutions made by the spin vector while circumnavigating the singularity at the origin [144].

$B_z \to 0$ drives the transition [98]

$$|F, m_z = +m_F\rangle \to \sum_{m_z=-|m_F|}^{|m_F|} \zeta_{m_z}(r) e^{[i(m_z - m_F)\phi]} |F, m_z\rangle. \tag{5.14}$$

The condensate population is distributed across $2|m_F|+1$ spin states (in the lab frame) with each acquiring a different topological phase factor and angular momentum per particle due to the variation of Berry's phase with magnetic quantum number [17]. At this point, the atomic spins are no longer polarized in the lab frame and a spin texture has been created. Fully inverting B_z repolarizes the atomic spins and generates vortices (Sec. 5.2).

5.3.1 Spin Textures

As B_z is varied, the condensate remains in the state $|F, m_F\rangle$ with respect to the local magnetic field provided the local Zeeman energy, $\sim \mu_B[B_z^2 + (B'r)^2]^{1/2}$, dominates the local kinetic energy associated with the spin texture, $\sim \hbar^2/mr^2$, where μ_B is the Bohr magneton and m is the atomic mass. For $B_z = 0$, atomic spins aligned with the

quadrupole magnetic field produce a planar spin texture [Fig. 5-6(a)]. However, the infinite kinetic energy associated with the wavefunction singularity at $r = 0$ creates a nonplanar spin texture over a disc of radius $\sim (\hbar^2/m\mu_B B')^{1/3}$, with higher angular momentum spin states residing outside those with lower angular momentum. Thus, ramping $B_z \rightarrow 0$ rotates the atomic spins by an amount that depends on radial position.

For condensates initially in the $|1,-1\rangle$ state, adiabatically ramping $B_z \rightarrow 0$ creates a spin texture in the lab frame described by (Eq. 5.5)

$$|\zeta(\vec{r})\rangle = \begin{array}{l} \cos^2[\beta(r)/2]\ |1,-1\rangle\ + \\ \frac{-1}{\sqrt{2}}\sin[\beta(r)]\ e^{+i\phi}\ |1,0\rangle\ + \\ \sin^2[\beta(r)/2]\ e^{+i2\phi}\ |1,+1\rangle, \end{array} \tag{5.15}$$

while for condensates initially in the $|1,+1\rangle$ state, adiabatically ramping $B_z \rightarrow 0$ creates a spin texture in the lab frame described by (Eq. 5.5)

$$|\zeta(\vec{r})\rangle = \begin{array}{l} \cos^2[\beta(r)/2]\ |1,+1\rangle\ + \\ \frac{+1}{\sqrt{2}}\sin[\beta(r)]\ e^{-i\phi}\ |1,0\rangle\ + \\ \sin^2[\beta(r)/2]\ e^{-i2\phi}\ |1,-1\rangle. \end{array} \tag{5.16}$$

These spin textures are classified as a skyrmions (merons) for the boundary conditions $\beta(0) = 0$ and $\beta(\infty) = \pi$ [$\beta(\infty) = \pi/2$].

By symmetry, we contend that the radial dependence of $\beta(r)$ should be the same for both spin textures (Eq. 5.15 and Eq. 5.16). However, since condensates initially in the $|1,+1\rangle$ state are in the absolute ground state of the system[5], the radial dependence of $\beta(r)$ can be found most easily by minimizing the Gross-Pitaevskii energy functional,

$$E(\beta) = \int d^3\vec{r}\ n\left[\frac{\hbar^2}{2m}\langle\nabla\zeta|\nabla\zeta\rangle + V + \left(\frac{c_0}{2} + \frac{c_2}{2}\frac{|\vec{F}|^2}{\hbar^2}\right)n\right], \tag{5.17}$$

respect to variations in β using Eq. 5.16 as a trial spinor. Equation 5.17 uses the

[5]Atoms in the $|1,+1\rangle$ ($|1,-1\rangle$) state are strong (weak) magnetic field seeking, such that in the presence of a magnetic field the $|1,+1\rangle$ state is the absolute ground state of the system.

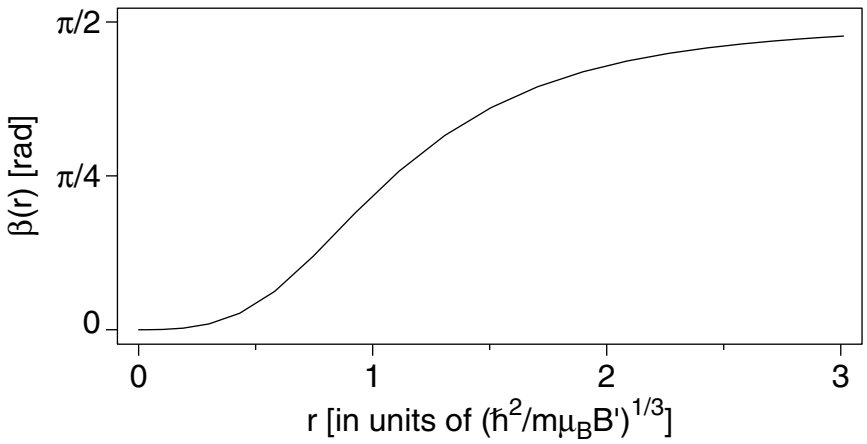

Figure 5-7: Radial dependence of the spin rotation angle. $\beta(r)$ is plotted for $B_z = 0$. For our radial magnetic field gradient, $B' = 180$ G/cm, $(\hbar^2/m\mu_B B')^{1/3} \approx 260$ nm.

Thomas-Fermi approximation, and $\langle \nabla\zeta | \nabla\zeta \rangle = \sum_{m_z=-F}^{F} \nabla\zeta_{m_z}^{\dagger} \cdot \nabla\zeta_{m_z}$, $V = g_F \mu_B \vec{F} \cdot \vec{B}/\hbar$, $\vec{F} = \langle \zeta | \vec{\mathcal{F}} | \zeta \rangle$, $c_0 = 4\pi\hbar^2\bar{a}/m$, and $c_2 = 4\pi\hbar^2\Delta a/m$. Here $\bar{a} = (2a_0 + a_2)/3$ and $\Delta a = (a_2 - a_0)/3$ characterize two-body interactions, where a_0 and a_2 are scattering lengths for binary collisions with total angular momentum $F = 0$ and $F = 2$, respectively [91]. For $c_2 > 0$ the atomic interactions are anti-ferromagnetic (polar), as in ^{23}Na [204], while for $c_2 < 0$ they are ferromagnetic, as in ^{87}Rb [117, 193].

Using Eq. 5.16 as a trial spinor, $\beta(r)$ satisfies the meron boundary conditions and varies from $\beta(0) = 0$, due to the kinetic energy of the spin texture, to $\beta(\infty) = \pi/2$, due to the atomic Zeeman energy, over a characteristic length scale given by the larger of $(\hbar^2/m\mu_B B')^{1/3}$ and $|B_z|/B'$ (Fig. 5-7). Terms proportional to $(\mathrm{d}\beta/\mathrm{dr})^2$ were neglected while varying Eq. 5.17. The trial spinor in Eq. 5.16 does not have the most general form since it was derived by rotating a polarized spinor (Eq. 5.5) and is inherently ferromagnetic, $|\vec{F}| = \hbar$. Accordingly, the spin dependent interaction term in Eq. 5.17 does not vary with $\beta(r)$ and therefore does not contribute to the determination of $\beta(r)$. This restriction is not severe since the Zeeman energy dominates the spin dependent interaction energy in our experiment.

5.3.2 Observation of Coreless Vortices

The experimental setup and conditions for producing spin textures were similar to those for producing vortices (Sec. 5.2.2). Condensates containing $\sim 2 \times 10^6$ atoms in the $|1,-1\rangle$ state were confined in a Ioffe-Pritchard Z-wire trap (Ch. 3, Figs. 3-4 and 3-5) with $I = 720$ mA, $B_\perp = 5.3$ G, and $B_z = B_{||} = 1.3$ G, resulting in a radial magnetic field gradient $B' = 180$ G/cm. The axial and radial trap frequencies were $\omega_z = 2\pi \times 4$ Hz and $\omega_\perp = 2\pi \times 250$ Hz, respectively.

Coreless vortices were imprinted in $F = 1$ spinor condensates by adiabatically ramping $B_z \rightarrow 0$ (Fig. 5-8). To observe the nature of the spin texture, an axial bias field was switched on non-adiabatically along either the negative [Figs. 5-8(a)-5-8(d)] or positive [Figs. 5-8(e)-5-8(h)] z axis. Switching the axial bias field on suddenly "froze" the atomic spins and effectively "projected" the condensate wavefunction onto a basis quantized with respect to the local (axial) magnetic field. This allowed the spin states to be separated by a magnetic field gradient applied during ballistic expansion. Switching the direction of the axial projection field exchanged the roles of the $|1,-1\rangle$ and $|1,+1\rangle$ states. With $B_z \approx 0$ the condensate lifetime was ~ 1 ms due to non-adiabatic spin-flips (Majorana flops) at the trap center. Therefore, the axial projection field was applied immediately after ramping $B_z \rightarrow 0$.

Figures 5-8(a) and 5-8(e) show the coreless nature of the vortices, while Figs. 5-8(b) and 5-8(f) show the concentric cylinder structure resulting from the competition between the atomic Zeeman energy and the kinetic energy of the rotating spin states. The boundary condition $\beta(0) = 0$ was maintained regardless of the sign of B_z, i.e. atomic spins along the trap axis always remained in the initial state. If the atomic spins had simply followed the local magnetic field, $\beta(r)$ would satisfy $\tan[\beta(r)] = B'r/B_z$. Thus, scanning B_z from slightly positive to slightly negative would instantaneously change the boundary condition at the origin from $\beta(0) = 0$ to $\beta(0) = \pi$ and flip the atomic spins along the trap axis. In interpreting the absorption images shown in Figs. 5-8(a), 5-8(b), 5-8(e), and 5-8(f), we have assumed that the two-dimensional ($\omega_z \ll \omega_\perp$) ballistic expansion process radially magnifies the conden-

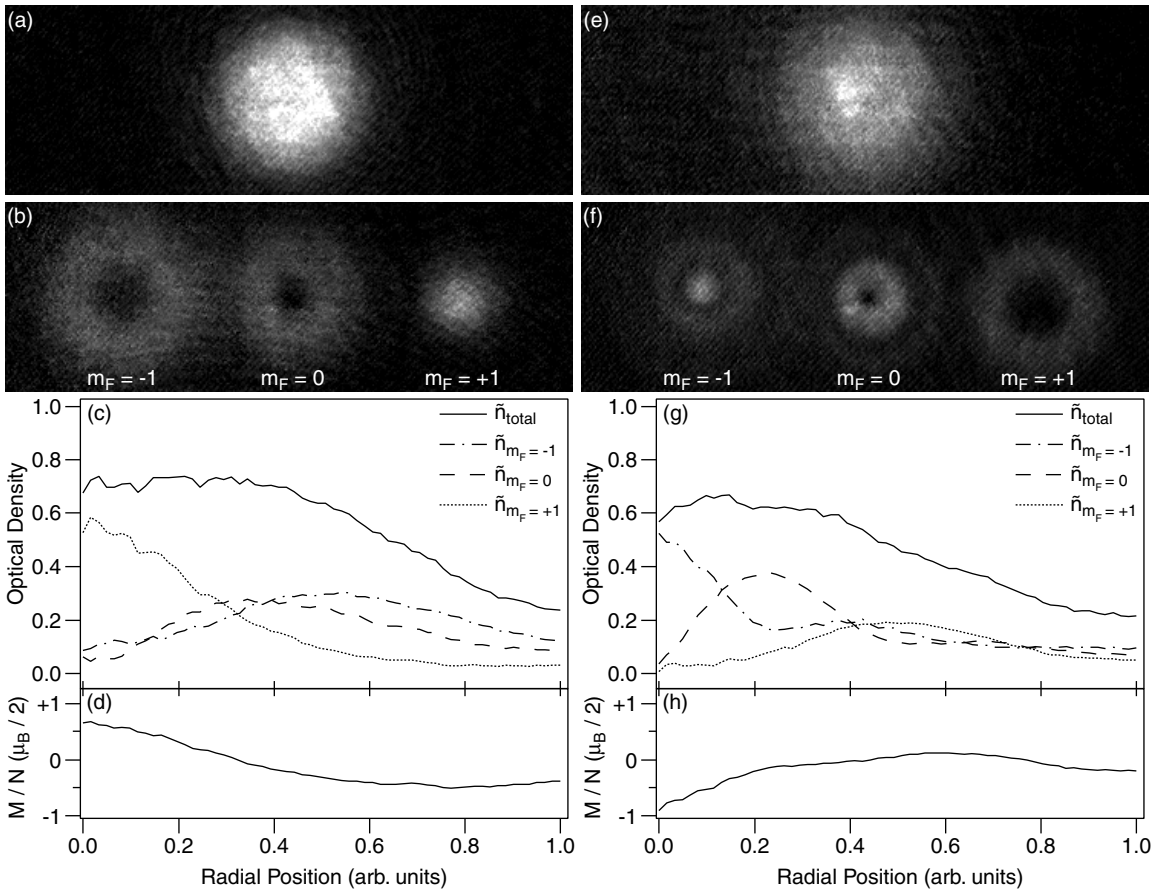

Figure 5-8: Coreless vortices in $F = 1$ spinor condensates. Coreless vortices were imprinted by ramping $B_z \to 0$ and diagnosed by suddenly switching (a)-(d) $B_z \ll 0$ and (e)-(h) $B_z \gg 0$. Axial absorption images display the optical density of condensates after 20 ms ballistic expansion (a,e) without and (b,f) with a magnetic field gradient applied to separate the different spin states. (c) and (g) Azimuthally averaged optical density vs radial position for spin components shown in (b) and (f), respectively. The radial separation of the spin states resulted from their relative phase windings and is a clear signature of the skyrmion/meron wavefunction (Eq. 5.15). (d,h) Axial magnetization per particle, $M/N = (\mu_B/2) \times (\tilde{n}_{m_F=+1} - \tilde{n}_{m_F=-1})/\tilde{n}_{total}$, vs radial position. The absorption imaging light was resonant with the $F = 2 \to F' = 3$ transition. The atoms were optically pumped into the $F = 2$ hyperfine level with a pulse resonant with the $F = 1 \to F' = 2$ transition. This provided equal imaging sensitivity to each spin state. The field of view in (a), (b), (e), and (f) is 1.0 mm × 3.0 mm.

sate wavefunction, as it does in the expansion of a single-component condensate with vortices [28, 43, 135].

Non-zero axial magnetic field curvature, $B'' \approx 5$ G/cm^2 (Eq. 5.11), along the microtrap axis implies that the spin texture had a slight axial dependence. The axial

bias field was ramped linearly from $B_z = 1.3$ G to $B_z \approx 0$ in 10 ms to imprint the coreless vortices. This compressed the condensate radially and increased the condensate chemical potential from $\mu \approx (\mu_B/2) \times 3$ mG to $\mu \approx (\mu_B/2) \times 27$ mG. Ramping $B_z \to 0$ fast compared to the axial trap period (250 ms), but slow compared to the initial radial trap period (4 ms), guaranteed that the axial magnetic field variation remained constant throughout the experiment at $\Delta B_z \approx 3$ mG, while at $B_z \approx 0$ the radial magnetic field variation was $\Delta B_r \approx 27$ mG. The images shown in Fig. 5-8 integrated the atomic number density along the z axis and therefore averaged over the minor ($\Delta B_z \ll \Delta B_r$) axial variation to the spin texture.

To project the condensate wavefunction onto a basis quantized with respect to the local magnetic field, a ~ 10 G axial bias field was switched on at a rate of $\dot{B}_z = 2 \times 10^5$ G/s along either the negative or positive z axis. 100 μs later the magnetic trap was switched off allowing the atoms to expand ballistically. For $0 \leq B_r \leq \Delta B_r$, the Landau-Zener non-adiabatic transition probability [185], $\exp(-\pi \mu_B B_r^2/\hbar \dot{B}_z) \geq 0.9$, was sufficiently close to unity that the atomic spins remained "frozen" during the sudden application of the axial bias field and the spin texture could be accurately diagnosed. While the total condensate density monotonically decreased as a function of radial position [Figs. 5-8(a) and 5-8(e)], the density of each spin component peaked at a different radius signifying a variation in the angular momentum per particle between spin states [Figs. 5-8(b) and 5-8(f)].

Applying the projection field along the positive z axis generated additional rings of atoms in the $|1, -1\rangle$ and $|1, 0\rangle$ states [Fig. 5-8(f)]. Ramping $B_z \to 0$ in 10 ms caused non-adiabatic spin-flips for atoms near $r = 0$ resulting in an atom loss of $\sim 50\%$ [123]. If these atoms had not left the condensate before the projection field was applied, they may have contributed to the images displayed in Fig. 5-8(f). The additional rings of atoms may also correspond to a low energy, radial spin-wave excitation [91, 160]. However, we could not identify any asymmetry between applying the projection field along the positive z axis as compared to the negative z axis that would account for the presence of the extra rings in Fig. 5-8(f), but not in Fig. 5-8(b).

The stability of the spin textures could not be characterized on time scales > 1 ms

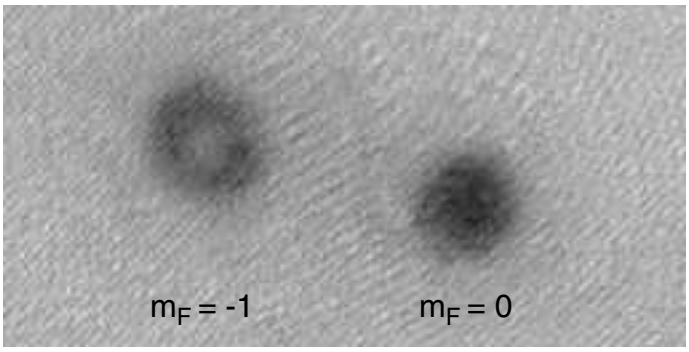

Figure 5-9: Vortices in an optical trap. Optically confined condensates were prepared in a coherent superposition of the $|1,-1\rangle$ and $|1,0\rangle$ states by a $\sim \pi/2$ radio frequency pulse. An overlapping Ioffe-Pritchard magnetic trapping potential (Eqs. 5.3 and 5.4) was turn on such that inverting the axial bias field imprinted vortices in the $|1,-1\rangle$ state (Eq. 5.6). No vortices were imprinted in the $|1,0\rangle$ state (Eq. 5.6). The axial absorption image was taken during ballistic expansion. The absorption imaging light was resonant with the $F = 2 \rightarrow F' = 3$ transition. The atoms were optically pumped into the $F = 2$ hyperfine level with a pulse resonant with the $F = 1 \rightarrow F' = 2$ transition. This provided equal imaging sensitivity to each spin state. The field of view is 1.0 mm $\times$ 2.0 mm.

due to non-adiabatic spin-flip transitions while $B_z \approx 0$ and excitations created by suddenly applying the axial projection field. It is predicted that skyrmions/merons in condensates with anti-ferromagnetic (ferromagnetic) interactions are unstable (stable) [13, 97, 114, 115, 139, 149, 150, 227, 228].

5.4 Vortices and Spin Textures in Optical Traps

Bose-Einstein condensates under optical confinement, as opposed to magnetic confinement, have their atomic spins decoupled from the trapping potential. For non-rotating condensates, spin dependent [193, 204] and magnetic field dependent [95] atom-atom interactions have been investigated. It is natural to extend these studies to rotating condensates where the ground state properties are predicted to depend strongly on spin composition and atom-atom interactions [13, 23, 97, 104, 114, 115, 116, 139, 149, 150, 176, 189, 190, 192, 225, 227, 228].

By overlapping a Ioffe-Pritchard magnetic trapping potential with an optical

dipole trap[6], vortices and spin textures were imprinted in condensates with arbitrary initial spin (Fig. 5-9). It was technically challenging to keep both traps overlapped while varying the axial bias field because the current-carrying coils that produced the axial field also produced a slight radial field. Thus, varying the axial bias field caused a variation in the radial bias field and shifted the radial position of the Ioffe-Pritchard magnetic trap.

5.5 Higher Order Vortices and Spin Textures

The phase imprinting technique described in this chapter can be extended to generate vortices and spin textures with higher winding numbers and angular momentum per particle by using higher-order, axisymmetric multipole magnetic fields and/or condensates with different spin. In general, a two-dimensional axisymmetric multipole magnetic field can be expressed as

$$\vec{B}(\vec{r}) = Ar^{\alpha-1}\left[\cos(\alpha\phi)\hat{r} - \sin(\alpha\phi)\hat{\phi}\right],\ \alpha > 0, \tag{5.18}$$

where $\alpha = 2$ describes a quadrupole field [Fig. 5-6(a)] and $\alpha = 3$ describes a hexapole field [Fig. 5-6(a)]. The topological phase factor in Eq. 5.7 is generalized to $e^{-i2(\alpha-1)m_F\phi}$ for inverting the axial bias field in the presence of an arbitary radial multipole magnetic field. A similar generalization is applicable for Eqs. 5.15 and 5.16.

Two-dimensional magnetic multiple fields for order α (Eq. 5.18) can be generated by $\alpha-1$ wires and an orthogonal bias field, $B_\perp$. For example, a single-wire waveguide (Ch. 3, Fig. 3-2) generates a quadrupole magnetic field, while a two-wire waveguide can generate a hexapole magnetic field for appropriate parameters [Ch. 3, Fig. 3-12(b)].

Additionally, vortices may be repeatedly imprinted in condensates to increase the angular momentum per particle. Vortices were imprinted by inverting the axial bias field in the presence of a radial multipole magnetic field, and were removed by

[6]The radial confinement frequency of the optical dipole trap was approximately two times higher than that of the magnetic trap.

returning the axial bias field to its original direction. If the magnetic multipole field is turned off before returning the axial bias field to its original direction, the vortices will remain in the condensate. Then, by turning back on the radial magnetic multipole field and subsequently inverting the axial bias field additional vortices are added to the condensate. In principle, this process can be cycled indefinitely to increase the vorticity of a condensate.

Chapter 6

Picokelvin Temperature Atomic Vapors

Low temperature and low density atomic vapors are used extensively for spectroscopy, metrology, atomic clocks, and atom optics. Extending the accessible temperature and density ranges to even lower values can reveal phase transitions, such as Bose-Einstein condensation [40, 110], the Kosterlitz-Thouless transition [118, 119, 120, 170, 175], and the Tonks-Girardeau transition [54, 65, 162, 171, 211] for Bosons and BCS pairing for Fermions [12, 19, 20], transitions to reduced dimensionality [67, 69, 188, 196], and quantum reflection from material surfaces [3, 14, 198].

Temperature is a quantity that parameterizes how energy is distributed across the available states of a system, and effective temperatures can be defined for decoupled degrees of freedom or subsets of particles. For example, nuclear spins isolated from the kinetic motion of their respective atoms have been cooled by adiabatic demagnetization to an effective temperature of 280 pK [161]. Spin ensembles have a finite number of available states so that a spin-polarized sample, such as a magnetically trapped condensate, would be characterized by zero effective temperature. In contrast, the motion of free particles is subject to a continuum of states, and the kinetic temperature of an ensemble can only asymptotically approach absolute zero.

Effective temperatures in atomic vapors are defined by the widths of velocity distributions, which can be much smaller than the mean velocity of the sample. Raman

cooling [106, 179] and velocity-selective coherent population trapping (VSCPT) [191] have generated velocity distributions with very narrow peaks, corresponding to nanokelvin and picokelvin effective temperatures. However, these temperatures were associated with the motion of only a subset of the atoms in the cloud and/or with atomic motion in only one dimension.

For trapped, partially condensed atomic vapors, the condensate fraction has zero entropy, and the kinetic temperature of the sample is determined by the velocity distribution of the thermal (noncondensed) component. When released, the condensate fraction expands slower than the thermal component and has been characterized by picokelvin effective temperatures for anisotropic [147] and non-interacting [217] gases.

Cooling the atomic motion of entire ensembles in all three dimensions has proven difficult. To date, kinetic temperatures of a few hundred nanokelvin have been achieved with adiabatic and optical cooling [108, 212], and evaporative cooling techniques have produced condensates with temperatures of 3 nK [51]. This chapter describes our efforts to adiabatically and evaporatively cool partially condensed atomic vapors to picokelvin kinetic temperatures and expands on the work presented in Ref. [124] (App. F).

Spin-polarized gaseous Bose-Einstein condensates were confined by a combination of gravitational and magnetic forces. The partially condensed atomic vapors were decompressed, by weakening the gravito-magnetic trap to a mean frequency of 1 Hz, then evaporatively reduced in size to 2500 atoms. This lowered the peak condensate density to 5×10^{10} atoms/cm^3 and cooled the entire cloud in all three dimensions to a kinetic temperature of 450 ± 80 pK. These samples were characterized by a thermal velocity ~ 1 mm/s, a speed of sound ~ 100 μm/s, and a healing length limited by the ~ 20 μm harmonic oscillator length of the trapping potential. The $1/e$ lifetime of condensates in the gravito-magnetic trap was 80 ± 5 s.

6.1 Thermometry

An upper limit for the temperature of a partially condensed atomic vapor is the Bose-Einstein condensation phase transition temperature, T_c, which in the thermodynamic limit for a harmonically-trapped ideal Bose gas is (Ch. 1, Eq. 1.3)

$$k_B T_c = \hbar\bar{\omega}\left(\frac{N}{\zeta(3)}\right)^{1/3} \approx 0.94\hbar\bar{\omega}N^{1/3}, \tag{6.1}$$

where k_B is Boltzmann's constant, $\zeta(n)$ is the Riemann Zeta function, $\bar{\omega} = (\omega_x\omega_y\omega_z)^{1/3}$ is the geometric mean of the harmonic trap frequencies, and N is the total number of atoms, both condensed and noncondensed. Thus, picokelvin temperatures ($T_c \leq 1$ nK) are guaranteed for partially condensed atomic vapors with $N \leq 10^4$ atoms confined at a mean frequency $\bar{\omega} \leq 2\pi \times 1$ Hz.

Corrections to Eq. 6.1 arise due to the finite size of the system and atom-atom interactions [42]. The finite size correction always reduces the BEC transition temperature whereas repulsive (attractive) atom-atom interactions reduce (increase) it. ^{23}Na in the $|1,-1\rangle$ state has a positive s-wave scattering length, $a \approx +2.8$ nm, and hence repulsive atom-atom interactions, such that for a given number of atoms and mean trap frequency Eq. 6.1 still provides an upper limit for the temperature of a partially condensed atomic vapor. For spherically symmetric systems, the finite size corrections scale as $\Delta T_c/T_c \propto -N^{-1/3}$ and the correction due to atom-atom interactions scales as $\Delta T_c/T_c \propto -(a/a_{HO})N^{1/6}$, where $a_{HO} = \sqrt{\hbar/m\bar{\omega}}$ and m is the atomic mass. For atomic vapors with $N = 10^4$ atoms confined at a mean frequency of $\bar{\omega} = 2\pi \times 1$ Hz, $\Delta T_c/T_c = -3 \times 10^{-2}$ and $\Delta T_c/T_c = -3 \times 10^{-5}$ due to finite size and interaction effects, respectively. Both of these corrections are negligible for the experiments discussed below.

Partially condensed atomic vapors contain two components, a thermal (noncondensed) component and a condensate component. The number of atoms in the thermal component, N_{th}, and their gaussian width in the trap, w_{th}, as well as the number of atoms in the condensate, N_0, are completely determined by the temperature, T,

and total number of atoms, $N = N_0 + N_{th}$, characterizing the sample. Provided that the thermal energy is much larger than the trap level spacing, $k_B T \gg \hbar\bar{\omega}$, and the cloud is in thermal equilibrium, the following relations hold:

$$N_{th} = \zeta(3) \times \left(\frac{k_B T}{\hbar\bar{\omega}}\right)^3, \tag{6.2}$$

$$w_{th} = \sqrt{\frac{2k_B T}{m\omega^2}}, \tag{6.3}$$

$$\frac{N_0}{N} = 1 - \left(\frac{T}{T_c}\right)^3, \tag{6.4}$$

where ω is the trap frequency for the axis along which w_{th} is measured. Equation 6.2 arises due to the population of all thermally accessible states, and Eq. 6.3 is a result of the equipartition theorem. Thermometry can be performed by examining the distribution of trapped thermal atoms (number and width) subject to the constraints in Eqs. 6.2 and 6.3. The presence of a condensate component leads to additional constraints on the total distribution of atoms.

6.2 Gravito-Magnetic Trap

Condensates in the $|F = 1, m_F = -1\rangle$ state containing up to 3×10^6 atoms were delivered to the science chamber using optical tweezers (Ch. 2) and loaded into the gravito-magnetic trap [Fig. 6-1]. A small coil carrying current I_S located vertically below the atoms generated a vertical bias field, B_z, and supported the weak field seeking condensates against gravity with a vertical magnetic field gradient, $B'_z = 2mg/\mu_B \approx 8$ G/cm, where m is the atomic mass, g is the gravitational acceleration, and μ_B is the Bohr magneton. Additional control over B_z and B'_z was provided by two external coils carrying independent currents I_U and I_L. Weak curvature, B''_z, to the vertical bias field created stable vertical confinement such that a harmonic restoring force was provided magnetically (gravitationally) for downward (upward) vertical displacements [Fig. 6-1(b)]. A radial field gradient $B'_r = \partial B_r/\partial r = -B'_z/2$ ($\nabla \cdot \vec{B} = 0$) was also present and added in quadrature with B_z to provide harmonic

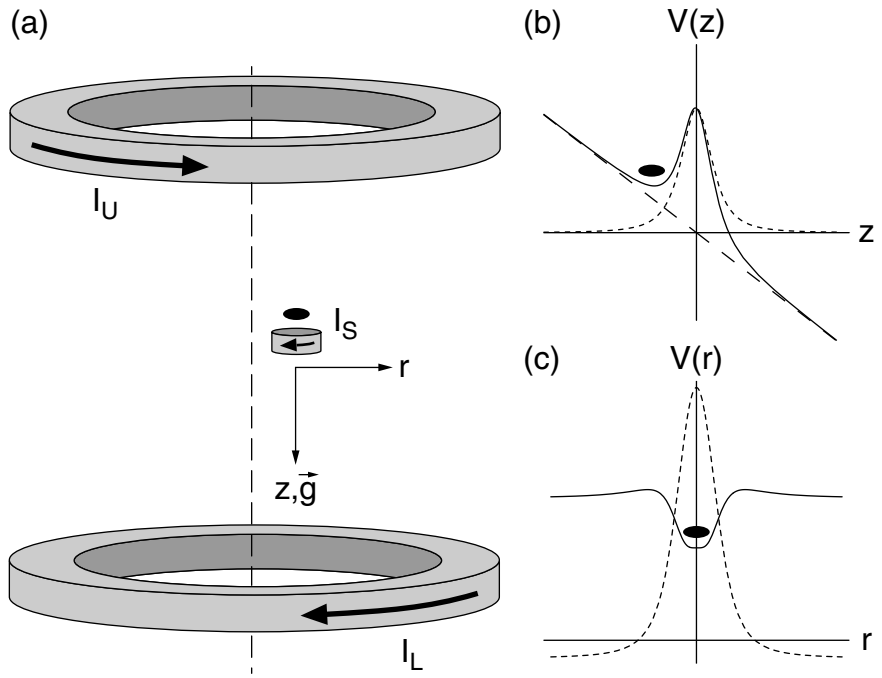

Figure 6-1: Gravito-magnetic trap. (a) Bose-Einstein condensates were levitated against gravity $\sim$ 5 mm above a 1 cm diameter, 25-turn coil mounted inside the ultrahigh vacuum chamber running current I_S. Two 10 cm diameter, 20-turn coils were mounted outside the vacuum chamber, and were supplied individually with currents I_U and I_L. The vertical separation between the large coils was 10 cm. The 1 cm diameter coil was mounted radially off-axis with respect to the pair of 10 cm diameter coils by $\sim$ 1 cm. This broke the cylindrical symmetry of the trapping potential. Additional bias fields $\sim$ 1 G were applied in the horizontal plane to cancel the radial magnetic fields generated by I_U and I_L on the axis of the small coil and maintain a stable trapping potential. The acceleration due to gravity, $\vec{g}$, points down the page. (b) Magnetic potential due to I_S (short dashed line), gravitation potential (long dashed line), and joint vertical potential of the gravito-magnetic trap (solid line). (c) A radially repulsive potential magnetic potential was generated by running I_S alone (dashed line), however applying a slight anti-bias field with I_U modified the radial energy profile and created a magnetic field minimum at $r = 0$ (solid line). In (a)-(c), the solid oval denotes the trapped condensate.

radial confinement with a restoring force proportional to $(B'_r)^2/B_z$ [Fig. 6-1(c)].

6.2.1 Stable Confinement

The magnetic field on axis of a single coil of radius R carrying current I is

$$B_z(z) = \frac{1}{2}\mu_0 I R^2 \frac{1}{(z^2+R^2)^{3/2}}, \tag{6.5}$$

where μ_0 is the permeability of free space. Neglecting terms $\mathcal{O}(r^3)$, the off axis magnetic field takes the form (in cylindrical coordinates) [99]

$$\vec{B}(r,z) \approx \left[B_z(z) - \frac{r^2}{4}B_z''(z)\right]\hat{z} - \frac{r}{2}B_z'(z)\hat{r}, \tag{6.6}$$

where the derivatives are given by

$$B_z'(z) = \frac{\partial B_z(z)}{\partial z} = -\frac{3}{2}\mu_0 I R^2 \frac{z}{(z^2+R^2)^{5/2}}, \tag{6.7}$$

$$B_z''(z) = \frac{\partial^2 B_z(z)}{\partial z^2} = \frac{3}{2}\mu_0 I R^2 \frac{4z^2-R^2}{(z^2+R^2)^{7/2}}. \tag{6.8}$$

Atom are levitated against gravity where $B_z' = 2mg/\mu_B$. Stable three-dimenational confinement about this point is only possible for vertical positions within a certain range. From Eq. 6.8 $B_z'' > 0$ for $|z| > R/2$, thus stable vertical confinement is only possible at distances greater than $R/2$ above the single coil. Stable radial confinement is possible only if $\partial|\vec{B}(r,z)|/\partial r > 0$, i.e. the magnitude of the magnetic field increases off axis. $\partial|\vec{B}(r,z)|/\partial r > 0$ for $(B_z')^2 - 2B_z B_z'' > 0$ or equivalently for $|z| < \sqrt{2/5}R$, thus stable radial confinement is only possible at distances less than $\sqrt{2/5}R \approx 0.63R$ above the single coil.

Combining these two results, we see that a stable, three-dimensional confinement potential is achieved for weak field seeking atoms at a distance $0.50R < |z| < 0.63R$ above a single current-carrying coil of radius R. For our parameters ($R \approx 5$ mm), stable three-dimensional confinement is only expected over a range $\Delta z = 0.13R = 650$ μm centered 2.825 mm above the single coil.

The criterion for stable vertical confinement is not flexible and atoms may only be trapped at distances greater than $R/2$ above the single coil. The criterion for stable

radial confinement, $(B_z')^2 - 2B_z B_z'' > 0$, is flexible since B_z in this inequality is the net bias field along the trap axis. B_z can be lowered by applying a vertical bias field that partially cancels the vertical field due to the single coil, and stable radial confinement is possible farther above the single coil than $\sqrt{2/5}R \approx 0.63R$ [Fig. 6-1(c)].

6.2.2 Radial Symmetry

The single coil gravito-magnetic trap has perfect radial symmetry. This is in contrast to traditional Ioffe-Pritchard magnetic traps formed by a two-dimensional quadrupole field and an axial bias field with curvature [68, 174]. The two-dimensional quadrupole field can be written as

$$\vec{B}(x, y, z) = B_r'(x\hat{x} - y\hat{y}), \tag{6.9}$$

while the axial bias field and curvature have components

$$\vec{B}(x, y, z) = \left[B_z + \frac{1}{2}B_z'' z^2 - \frac{1}{4}B_z''(x^2 + y^2)\right]\hat{z} - \frac{1}{2}B_z'' z(x\hat{x} + y\hat{y}). \tag{6.10}$$

The terms $-(B_z'' z/2)(x\hat{x} + y\hat{y})$ in Eq. 6.10 are necessary in order to satisfy Maxwell's equations and interfere with the two-dimensional quadrupole field (Eq. 6.9) to produce effective magnetic field gradients $B_x' = B_r' - B_z'' z/2$ and $B_y' = B_r' + B_z'' z/2$ along the x and y axis, respectively. Thus, the radial symmetry of traditional Ioffe-Pritchard magnetic trapping potentials is broken for planes $z \neq 0$.

6.3 Cooling Stages

For typical loading parameters ($I_S = 340$ mA, $I_U = 5.5$ A, and $I_L = 0$) the gravito-magnetic trap was spherically symmetric with trap frequencies $\omega_x \approx \omega_y \approx \omega_z \approx 2\pi \times$ 8 Hz. Condensates loaded into the gravito-magnetic trap from the optical tweezers were held for 5 s to allow for the damping of excitations. The resulting partially condensed clouds had $\sim 5 \times 10^5$ atoms and a BEC transition temperature $T_c = 30$ nK. At all times, the atomic vapor maintained a temperature T such that $0.5 < T/T_c < 1$.

6.4 Adiabatic Decompression

Further cooling was accomplished by adiabatically decompressing the trapping potential in two 5 s stages, with a 5 s delay in between to allow excitations to damp. In the first stage, the vertical frequency was reduced to $\omega_z = 2\pi \times (1.81 \pm 0.05)$ Hz by simultaneously raising currents I_L and I_U by identical amounts and lowering the current I_S by a factor of 10. This kept the magnetic field gradient, B'_z, constant, but transferred its dominant source from the small coil to the external coils. The external coils produced very little magnetic field curvature due to their large diameters (Eq. 6.8), thus the net magnetic field curvature was reduced by lowering I_S. In the second stage, the radial frequencies were reduced to $\omega_x = 2\pi \times (0.65 \pm 0.05)$ Hz and $\omega_y = 2\pi \times (1.2 \pm 0.1)$ Hz by raising I_L and lowering I_U by identical amounts. The vertical magnetic field gradient and curvature remained constant, but the vertical bias field, B_z, increased. This reduced the radial confinement due to the scaling $\omega_r \propto B'_r/B_z^{1/2}$ [68, 174]. The radial asymmetry ($\omega_x \neq \omega_y$) arose because the small coil and the large external coils were not coaxial [Fig. 6-1(a)].

For currents $I_S = 34$ mA, $I_U = 14$ A, and $I_L = 44$ A, the final gravito-magnetic trap had a mean frequency $\bar{\omega} = 2\pi \times (1.12 \pm 0.08)$ Hz and an axial bias field $B_z = 17$ G. The trap frequencies were measured by observing the condensate oscillate in the trap, and the axial bias field was measured by driving the microwave transitions $|1, -1\rangle \rightarrow |2, 0\rangle,\ |2, -1\rangle,\ |2, -2\rangle$. The residual anharmonicities of the trapping potential were small, with $\Delta\omega/\omega = 0.1$ for 500 μm displacements from the trap center. Further radial decompression was not possible due to a finite trap depth [Fig. 6-1(c)] and sensitivity of trap stability to milligauss level radial bias fields.

6.4.1 Evaporative Atom Number Reduction

After decompression, the partially condensed atomic vapors had $\sim 2 \times 10^5$ atoms and a BEC transition temperature $T_c = 3$ nK. T_c was lowered further by reducing the number of atoms in the cloud (Eq. 6.1), while maintaining a substantial condensate fraction at all times ($0.5 < T/T_c < 1$). The atom number was reduced by holding the

atoms in the gravito-magnetic trap for up to 200 s. Often, microwave radiation near the $|1,-1\rangle \rightarrow |2,0\rangle$ transition was applied to shorten the hold time required to arrive at lower atom number to 10 s. The atom number reduction was accompanied by cooling, during which the elastic collision rate (between thermal atoms and the condensate) dropped from 0.25 Hz to 0.01 Hz. Therefore, a few collisions were sufficient to cause evaporation out of the finite depth trap. This cooling was not efficient in the sense of providing a gain in phase-space density, but still was capable of maintaining thermal equilibrium and lowering the absolute temperature of the vapor (see below).

6.5 Picokelvin Temperatures

Using this technique, we cooled partially condensed vapors containing up to 30000 atoms to temperatures below 1 nK (Figs. 6-2 and 6-3). Our lowest measured three-dimensional kinetic temperature was 450 ± 80 pK for 2500 atoms at a peak condensate density of 5×10^{10} atoms/cm^3. Under these conditions, the peak atom-atom interaction energy was $\mu = k_B \times 33$ pK $= h \times 0.7$ Hz, while the zero point energy of the harmonic trapping potential was $(1/2)\hbar\bar{\omega} = k_B \times 27$ pK. Condensates released from the gravito-magnetic trap would expand with energies of this order, and therefore could be characterized by effective temperatures ~ 30 pK.

Additional cooling would require lowering the trap frequencies further or reducing the atom number more. However, weakly confining traps have proven technically difficult to control such that lowering $\bar{\omega}/2\pi$ substantially below 1 Hz is challenging. Likewise, because $T_c \propto N^{1/3}$, atom number reduction by an order of magnitude only results in temperature reduction by a factor of two. Furthermore, lower temperatures and lower densities are accompanied by collisional equilibrium times approaching 100 s.

The temperature of the atomic vapors was extracted by fitting integrated, one-dimensional atomic density cross-sections by a bimodal distribution (Fig. 6-2)

$$n(x) = N_0 \Psi_0^2 + \frac{N_{th}}{\sqrt{\pi} w_{th}} e^{-x^2/w_{th}^2}, \tag{6.11}$$

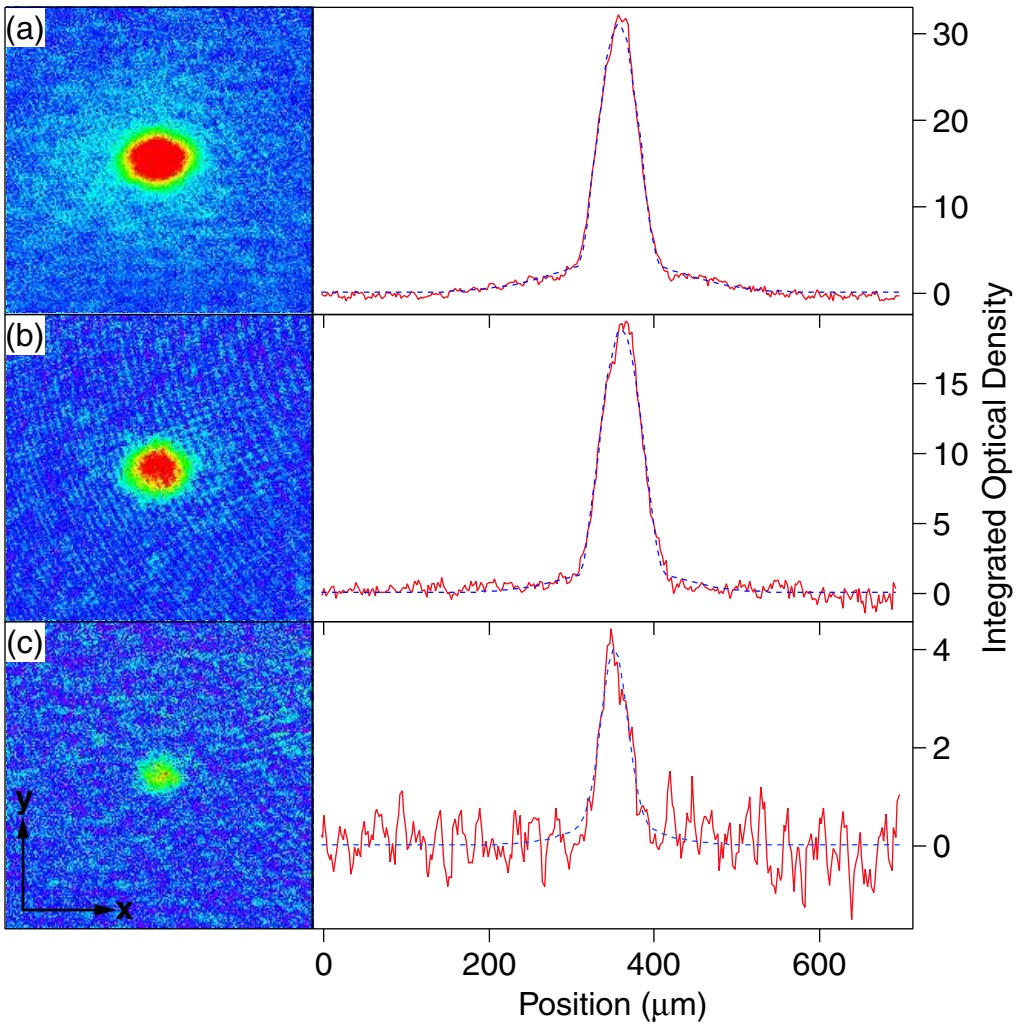

Figure 6-2: (Color) Picokelvin temperature thermometry. Partially condensed atomic vapors confined in the gravito-magnetic trap with (a) 28000, (b) 16000, and (c) 2500 atoms. The one-dimensional cross sections (red solid line) were obtained by integrating the two-dimensional absorption images of the trapped clouds along the y axis. Bimodal fits to Eq. 6.11 (blue dashed line) yielded temperatures of (a) 1.05 ± 0.08 nK, (b) 780 ± 50 pK, and (c) 450 ± 80 pK, where the uncertainty is due to the fit of an individual image. The absorption imaging light was resonant with the $F = 2 \rightarrow F' = 3$ cycling transition for the trapped atoms, and was aligned with the vertical (z) axis. The atoms were optically pumped into the $F = 2$ hyperfine level with a pulse resonant with the $F = 1 \rightarrow F' = 2$ transition. The field of view for the absorption images in (a)-(c) is 460 μm $\times$ 460 μm.

where N_{th}, w_{th}, and N_0 are given in Eqs. 6.2, 6.3, and 6.4, respectively, and Ψ_0^2 is a bell-shaped function with width w_0 that describes the condensate peak. The fitted parameters were T, N, and w_0.

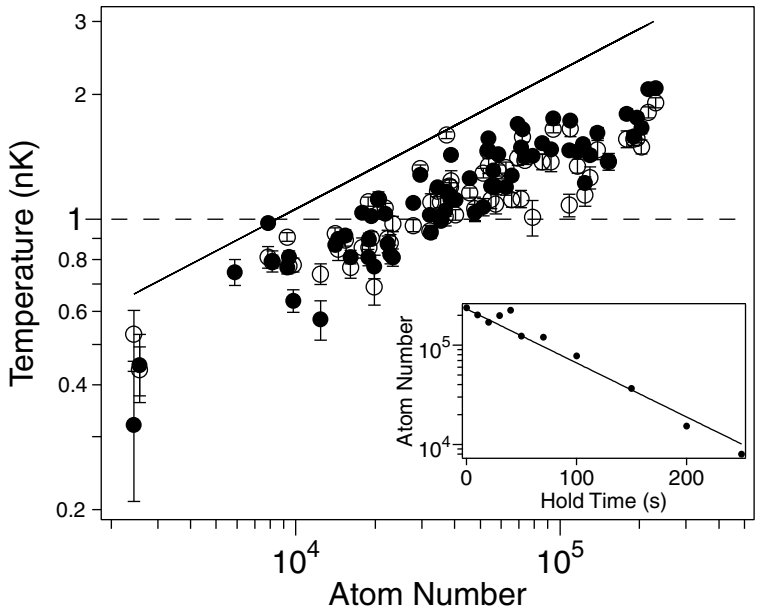

Figure 6-3: Partially condensed atomic vapors at picokelvin temperatures. The temperature of over 60 partially condensed atomic vapors is plotted vs total number of condensed and noncondensed atoms. A solid line at the Bose-Einstein condensation phase transition temperature (Eq. 6.1) and a dashed line at 1 nK are provided as a guides. Condensate temperatures were determined from one-dimensional fits to atomic density cross sections integrated along either the x (closed circles) or y (open circles) axis (Fig. 6-2). Differences in the two measured temperatures for a single condensate reflect the true uncertainty of the measurement. Plotted error bars represent the statistical uncertainty of the fit. The inset shows that the $1/e$ condensate lifetime in the gravito-magnetic trap was limited by one-body processes to 80 ± 5 s.

Because $\mu \approx \hbar\bar{\omega}$, the condensates in the gravito-magnetic trap were in a density regime intermediate between the Thomas-Fermi ($\mu \gg \hbar\bar{\omega}$) and ideal ($\mu \ll \hbar\bar{\omega}$) gas limits. Data fit using either the Thomas-Fermi condensate wavefunction [$\Psi_0^2 = (15/16)w_0^{-1}max(1 - x^2/w_0^2, 0)^2$] or the ideal gas condensate wavefunction [$\Psi_0^2 = w_0^{-1}\pi^{-1/2}\exp(-x^2/w_0^2)$] yielded the same atom number and temperature. Also, the fitted atom number and temperature were independent of the use of microwave radiation to reduce the atom number.

All atomic vapors represented in Fig. 6-3 had a clear bimodal density distribution from which a temperature was reproducibly extracted. The temperatures extracted from one dimensional fits along both radial axis were nominally the same, empirically indicating that the atomic vapors remained close to thermal equilibrium at all times.

Chapter 7

Conclusion

As emphasized by its title, *Microtraps and Waveguides for Bose-Einstein Condensates*, this thesis has focused on the design and implementation of devices to advance the field of atom optics. Connections between atom optics and photon optics are made frequently. For example, the magnetic waveguides demonstrated in Ch. 3 are the matter wave analog to fiber optic cables. However, matter wave theory is typically nonlinear due to atom-atom interactions (Ch. 1, Eq. 1.4). While this nonlinearity gives rise to interesting atom optical phenomena, such as four wave mixing [49, 215], it often plagues devices such as beam splitters [8, 81, 90, 201, 206] and produces systematic uncertainties in precision interferometry [71].

Bose-Einstein condensates are a fully coherent source of matter waves [9, 25, 107, 113], however exploiting this coherence for atom interferometric purposes has been limited by their nonlinear interactions. The trapped-atom interferometer demonstrated in Ch. 4 successfully utilized the phase coherence associated with the condensate wavefunction, while avoiding complications arising due to wavepacket recombination in the presence of atom-atom interactions. Likewise, Ch. 6 demonstrated partially condensed atomic vapors at picokelvin temperatures and densities two or three orders of magnitude lower than typical condensates. At these low densities, the atom-atom interaction energy may be low enough to pursue precision atom interferometry with Bose-Einstein condensates [71]. An alternative approach to lowering the mean field energy of the condensate is through the use of a Feshbach resonance where atom-

atom interactions can be tuned to zero with an external magnetic field [41, 95, 217]. However, performing precision interferometer with the aid of a Feshbach resonance would require excellent magnetic field control since the atom-atom interactions vary rapidly with the applied field.

7.1 Superfluid Gyroscope

Placing Ch. 5 (*Vortices and Spin Textures*) in the context of atom optics is more subtle. Rotation sensing is a major application of atom interferometers, and the inherent rotation associated with a vortex state can be used as a superfluid gyroscope [11, 93, 197].

Consider the superposition of two spin states

$$|\psi\rangle = \frac{1}{\sqrt{2}}(|1,-1\rangle + |2,+1\rangle), \tag{7.1}$$

held in a Ioffe-Pritchard magnetic trap. The superposition $|\psi\rangle$ was chosen because both the $|1,-1\rangle$ and $|2,+1\rangle$ state are weak field seeking and have the same magnetic moment. This allows for long spin coherence times even in the presence of the magnetic field gradients. The superposition $|\psi\rangle$ has been created in ^{87}Rb condensates with coherence times > 100 ms [79]. Inelastic spin-exchange collisions between atoms in different hyperfine states are suppressed in ^{87}Rb as compared to ^{23}Na such that the condensate lifetime in the state $|\psi\rangle$ is a few seconds for ^{87}Rb [79] while it is expected to be a few milliseconds for ^{23}Na [66].

Vortices created by the topological phase imprinting technique demonstrated in Ch. 5 were shown to have a winding number that depended on the magnitude and sign of the magnetic quantum number, m_F, describing the atomic state. Hence, imprinting vortices in state $|\psi\rangle$ produces counter rotating spin states

$$|\psi\rangle \rightarrow \frac{1}{\sqrt{2}}\left(e^{i2\phi}|1,-1\rangle + e^{-i2\phi}|2,+1\rangle\right), \tag{7.2}$$

where ϕ is the azimuthal angle with respect to the vortex line. We have taken

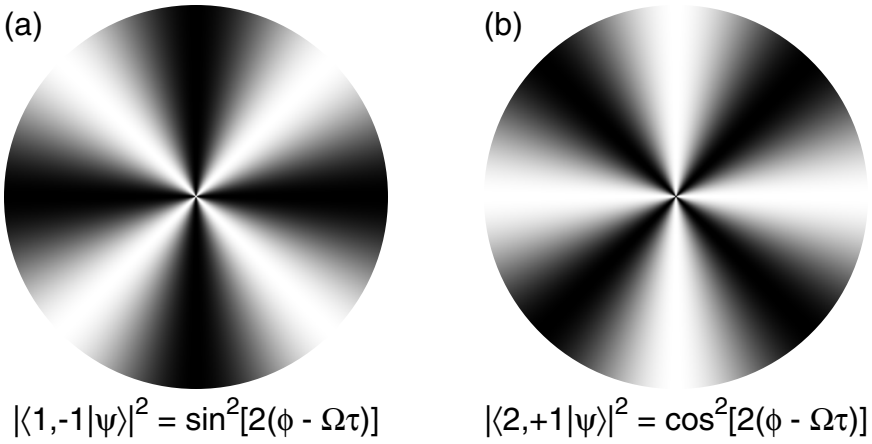

Figure 7-1: Vortex phase interferogram. Density distribution for atoms in the (a) $|1,-1\rangle$ and (b) $|2,+1\rangle$ states for the wavefunction in Eq. 7.5. In the presence of external rotation, these patterns rotate as τ is varied (see text).

quadrupolar radial confinement for the Ioffe-Pritchard magnetic trap [Ch. 5, Fig. 5-6(a)]. Higher order phase windings can be imprinted using higher order mulitpole magnetic fields. This will increase the rotation sensitivity of the gyroscope.

To account for the presence of external rotation, the azimuthal angle ϕ is replaced by $\phi \rightarrow \phi - \Omega t$, where Ω is the rotation rate projected along the vortex line and t is time. The time dependent offset angle, Ωt, can be derived from the standard expression for the Sagnac phase shift due to rotation (Ch. 4, Eq. 4.1)

$$\Delta\phi_{rot} = \frac{2m}{\hbar}\Omega A, \tag{7.3}$$

where m is the atomic mass and A is the area enclosed by the rotating atoms. For the vortex states in Eq. 7.2, the superfluid velocity is $|v_s| = 2\hbar/mr$, where r is the radial displacement from the vortex line. The total area enclosed by the rotating atoms is $\pi r^2 \times t/(2\pi r/|v_s|) = (\hbar/m)t$, where πr^2 is the area enclosed while making one loop around the condensate in a time $2\pi r/|v_s|$. Substituting this result into Eq. 7.3, we see that $\Delta\phi_{rot} = 2\Omega t$, where the factor of 2 is due to the winding number of the vortex state.

In the presence of external rotation, the counter-rotating vortex superposition

state evolves as

$$|\psi\rangle \rightarrow \frac{1}{\sqrt{2}}\left(e^{i2(\phi-\Omega t)}|1,-1\rangle + e^{-i2(\phi-\Omega t)}|2,+1\rangle\right). \tag{7.4}$$

Driving a $\pi/2$ transition between the states $|1,-1\rangle \leftrightarrow |2,+1\rangle$ at a time τ after creating the vortex superposition yields the wavefunction

$$|\psi\rangle \rightarrow i\sin[2(\phi-\Omega\tau)]|1,-1\rangle + \cos[2(\phi-\Omega\tau)]|2,+1\rangle, \tag{7.5}$$

The angular dependence of the $|1,-1\rangle$ and $|2,+1\rangle$ state densities varies with τ according to the external rotation rate. Thus, the external rotation rate can be extracted from the measured phase of the density distributions (vortex interferogram) as a function of τ (Fig. 7-1).

For $\tau = 1$ s, a rotation rate of $10^3 \times \Omega_\oplus$, where $\Omega_\oplus$ is the rotation rate of the Earth, would cause a phase shift of ~ 8 degrees to the vortex interferogram. This is far from the rotation sensitivity achievable with other atom interferometry techniques [73, 129] and liquid helium superfluid gyroscopes [11, 197], but demonstrates the principle of rotation sensing with superfluids.

7.2 Last Man Standing

The science chamber apparatus (Ch. 2) has performed well over its two year life. I am the last member of its construction team still working on the apparatus and will take away the last memories its infancy when I depart. This includes nervous times, like when we mistakenly vented the BEC production chamber, when the magnetic trap sprung a water leak, when we first tried to evaporatively cool to BEC but found the magnetic trap bottom to be ~ 6 G too high, and joyous times, like when we made our first condensate and when we were finally able to translate condensates into the science chamber.

I wish all future users the best of luck in creating their own fond memories.

Appendix A

Propagation of Bose-Einstein Condensates in a Magnetic Waveguide

This appendix contains a reprint of Ref. [122]: A.E. Leanhardt, A.P. Chikkatur, D. Kielpinski, Y. Shin, W. Ketterle, and D.E. Pritchard, *Propagation of Bose-Einstein Condensates in a Magnetic Waveguide*, Phys. Rev. Lett. **89**, 040401 (2002).

Propagation of Bose-Einstein Condensates in a Magnetic Waveguide

A. E. Leanhardt, A. P. Chikkatur, D. Kielpinski, Y. Shin, T. L. Gustavson, W. Ketterle, and D. E. Pritchard *

Department of Physics, MIT-Harvard Center for Ultracold Atoms, and Research Laboratory of Electronics, Massachusetts Institute of Technology, Cambridge, Massachusetts 02139

(Received 9 March 2002; published 2 July 2002)

Gaseous Bose-Einstein condensates of $2-3 \times 10^6$ ^{23}Na atoms were loaded into a microfabricated magnetic trap using optical tweezers. Subsequently, the condensates were released into a magnetic waveguide and propagated 12 mm. Single-mode propagation was observed along homogeneous segments of the waveguide. Inhomogeneities in the guiding potential arose from geometric deformations of the microfabricated wires and caused strong transverse excitations. Such deformations may restrict the waveguide physics that can be explored with propagating condensates. Finer perturbations to the guiding potential fragmented the condensate when it was brought closer to the surface.

DOI: 10.1103/PhysRevLett.89.040401 PACS numbers: 03.75.Fi, 03.75.Be, 39.20.+q

Progress in the field of atom optics depends on developing improved sources of matter waves and advances in their coherent manipulation. Bose-Einstein condensates of dilute alkali vapors [1] are now used as sources of coherent atoms. Miniaturizing the current carrying structures used to confine condensates offers prospects for finer control over the clouds [2,3]. Following the successful trapping and guiding of thermal atoms using self-supported miniature wires [4–8] and substrate-supported microfabricated wire arrays [9–12], recent experiments merged wire traps on the millimeter scale [13] and microfabricated electronic devices [14,15] with Bose-Einstein condensation. This has opened up a front on which further techniques for coherent condensate transport and manipulation can be explored. While condensate guiding with optical potentials may be limited fundamentally by diffraction [16], fundamental limitations to guiding condensates with microfabricated surfaces are not expected for an atom-surface separation in excess of 1 μm [17].

In this Letter, we demonstrate that a Bose-Einstein condensate (BEC) transported with optical tweezers can be transferred into a microtrap on a substrate. Such condensates contained 5 times more atoms than those created in a similar microtrap [14]. We released the BEC from the microfabricated magnetic trap into a single-wire magnetic waveguide and studied its propagation. Condensates were observed to propagate 12 mm before exiting the field of view of our imaging system. We observed single-mode (excitationless) BEC propagation along homogeneous segments of the waveguide in a regime where the longitudinal kinetic energy of the condensate exceeded its transverse confinement energy. Transverse excitations were created in condensates propagating through perturbations in the guiding potential. These perturbations resulted from geometric deformations of the current carrying wires on the substrate. Finer imperfections were observed when trapped condensates were brought closer to the microchip as evidenced by the longitudinal fragmentation of the cloud.

Condensates containing over 10^7 ^{23}Na atoms were created in the $|F, m_F\rangle = |1, -1\rangle$ state in a macroscopic Ioffe-Pritchard magnetic trap [18], loaded into the focus of an optical tweezers beam, and transported over 30 cm in 1250 ms into an auxiliary "science" chamber as described in Ref. [13]. Condensates containing $2-3 \times 10^6$ atoms arrived less than 500 μm below the microfabricated structures mounted in the science chamber. The optical tweezers consisted of 50 mW of 1064 nm laser light focused to a $1/e^2$ radius of 26 μm. This resulted in axial and radial trap frequencies of 4 and 440 Hz, respectively, and a trap depth of 2.7 μK.

A schematic of the microchip onto which the BEC was loaded is shown in Fig. 1. The microfabricated wires lie on a 600 μm thick silicon substrate mounted on an aluminum block. They are 50 μm wide and electroplated with copper to a thickness of 10 μm. The minimum separation distance between wires is 50 μm (100 μm center-to-center). Macroscopic leads that extended to a vacuum feedthrough were attached to the wafer using a gap welding technique. The BEC was initially loaded into a Z-wire trap [9] formed by currents I_1 and I_2 along with an orthogonal magnetic bias field $B_\perp$. Typical loading conditions were $I_1 = I_2 = 1200$ mA and $B_\perp = 5.4$ G, corresponding to a separation of 450 μm between the BEC and the microchip. The longitudinal trap frequency was $\omega_{||} = 2\pi \times 6.0$ Hz and, for a longitudinal bias field $B_{||} = 3.0$ G, the transverse trap frequency was $\omega_\perp = 2\pi \times 97.0$ Hz. Transfer efficiency from the optical tweezers to the Z-wire trap was near unity, and BEC lifetimes over 10 s were observed with the application of a radio frequency (rf) shield [18] which limited the trap depth to ≈ 1 μK and was produced by the current $I_{\rm rf}$ on an auxiliary wire, as shown in Fig. 1.

The BEC was transferred into the waveguide by linearly ramping the current I_2 to zero in 250 ms. The atoms were accelerated into the waveguide by the remaining end cap of the Z-wire trap. Downstream, the effect of this end cap was negligible and we observed BEC propagation at a constant velocity of 3.0 cm/s after a propagation distance of 4 mm for $I_1 = 1200$ mA. Upon releasing the BEC from the Z-wire trap, its longitudinal velocity was controlled by applying an external longitudinal magnetic field gradient

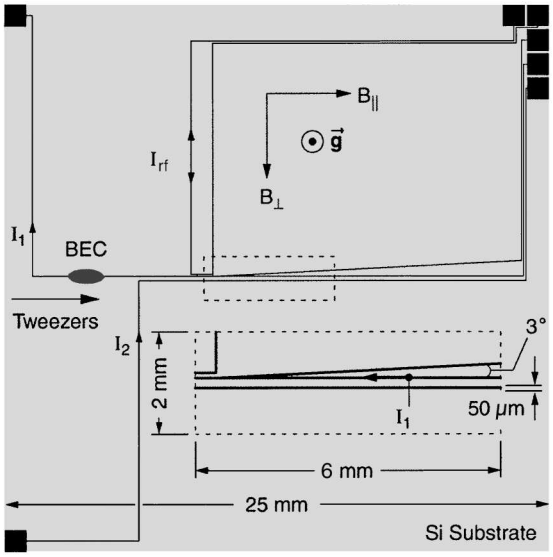

FIG. 1. Microfabricated magnetic trap and waveguide. Optical tweezers loaded a Bose-Einstein condensate into the Z-wire trap formed by currents I_1 and I_2 in conjunction with the magnetic bias field $B_\perp$. Lowering I_2 to zero released the condensate into a single-wire magnetic waveguide. Atom flow was from left to right. The inset shows the widening of the waveguide wire in the region where another wire merges with it at a small angle. The only current flowing in the inset is I_1. The condensate was trapped above the plane of the page and the gravitational acceleration, $\vec{g}$, points out of the page. All microfabricated features are drawn to scale.

created by running current through a single coil coaxial with the waveguide axis. The field gradient was linearly ramped up and down over 6.5 ms to prevent creating excitations and was held constant for 52 ms. With gradients of 0–0.6 G/cm, the atomic velocity was varied over the range 3.0–6.6 cm/s. Throughout this work, condensates were detected via absorption imaging whereby resonant laser light propagating parallel to $B_\perp$ illuminated the atoms and was imaged onto a CCD camera [18].

For all velocities, we observed single-mode condensate propagation along unperturbed sections of the waveguide, as shown in Fig. 3(a) below. The condensate depicted has a smooth shape without any excitations.

Perturbations to the guiding potential arise from geometric deformations of the current carrying wires on the substrate. The extent to which such deformations alter the potential experienced by the atoms depends on the atom-wire separation distance, r, longitudinal extent of the perturbation, ℓ, wire width, w, and wire thickness, t. Under our guiding conditions ($r \gg w, t$) the waveguide potential responds only to changes in the centroid of the current density. In general, only wire deformations with $\ell \gtrsim r$ will significantly perturb the guiding potential due to solid angle considerations. Such a deformation ($\ell \approx 1$ mm, $r = 450$ μm) is depicted in the inset of Fig. 1. As the wire width varies during the bifurcation process, the centroid of the current density will shift in the plane of the microchip. This shift will be mirrored by a shift in the trajectory of the guide in a plane parallel to that of the microchip [19]. Such a shift causes the guide axis to make an angle, θ, with respect to its nominal trajectory along which $B_{||}$ and $B_\perp$ are aligned parallel and perpendicular, respectively. As a result, the effective parallel, $B'_{||}$, and perpendicular, $B'_\perp$, magnetic fields are found by the rotation

$$B'_{||} = B_{||}\cos\theta - B_\perp \sin\theta, \tag{1}$$

$$B'_\perp = B_\perp \cos\theta + B_{||}\sin\theta, \tag{2}$$

where $-\pi/2 \le \theta \le \pi/2$. θ is taken to be a positive (negative) angle for the specific case of atoms entering (exiting) the waveguide perturbation depicted in the inset of Fig. 1.

Since the potential along the waveguide axis is determined by the local magnetic field (due to the Zeeman interaction) and the vertical position of the guide center (due to the gravitational interaction), changes in the effective parallel and perpendicular magnetic fields produce variations in the potential experienced by the propagating atoms. Variations in the effective parallel magnetic field are given by (for small angles)

$$\Delta B'_{||} = -B_\perp \sin\theta\,. \tag{3}$$

Thus, atoms entering (exiting) the perturbed guiding region will encounter a magnetic potential well (barrier). Furthermore, changes in the effective perpendicular magnetic field cause the atom-substrate distance to vary by (for small angles)

$$\Delta r = -r\,\frac{\Delta B'_\perp}{B_\perp} = -r\,\frac{B_{||}}{B_\perp}\,\sin\theta\,. \tag{4}$$

Thus, the guide center entering (exiting) the perturbed guiding region will shift towards (away from) the surface of the microchip, and atoms will encounter a gravitational potential barrier (well). For ^{23}Na atoms in the $|1, -1\rangle$ state, the Zeeman interaction energy is $h \times 700$ Hz/mG and the gravitational interaction energy is $h \times 560$ Hz/μm, where h is Planck's constant.

The effects of the perturbation depicted in the inset of Fig. 1 on BEC propagation were studied by varying the incident velocity of the atoms sent into the region. Condensates traveling below 4.5 cm/s were totally reflected from the perturbation, while clouds at speeds above 5.4 cm/s were entirely transmitted. Figure 2 shows the results for intermediate atomic velocities. The local magnetic field in the perturbed guiding region was measured by driving rf spin-flip transitions that removed atoms from the guide [18]. It was found that upon entering (exiting) the perturbed region the magnetic bottom of the guiding potential decreased (increased) by $h \times (50 \pm 10)$ kHz. The signs of these shifts are consistent with those predicted by Eq. (3). The magnitude of the shift in the Zeeman energy upon exiting the guide is also consistent

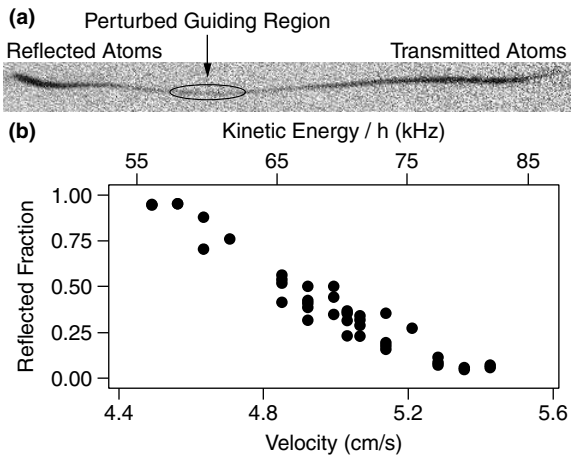

FIG. 2. Bose-Einstein condensates scattering from the waveguide perturbation shown in the inset of Fig. 1. (a) Absorption image after 8 ms of ballistic expansion of a partially transmitted condensate. The incident velocity was 5.0 cm/s. (b) The fraction of atoms reflected as a function of incident velocity. Waveguide parameters for all data were $I_1 = 1200$ mA, $B_\perp = 5.4$ G, $B_{||} = 3.6$ G, and $\omega_\perp = 2\pi \times 84.5$ Hz. The field of view in (a) is 0.35 mm $\times$ 4.00 mm.

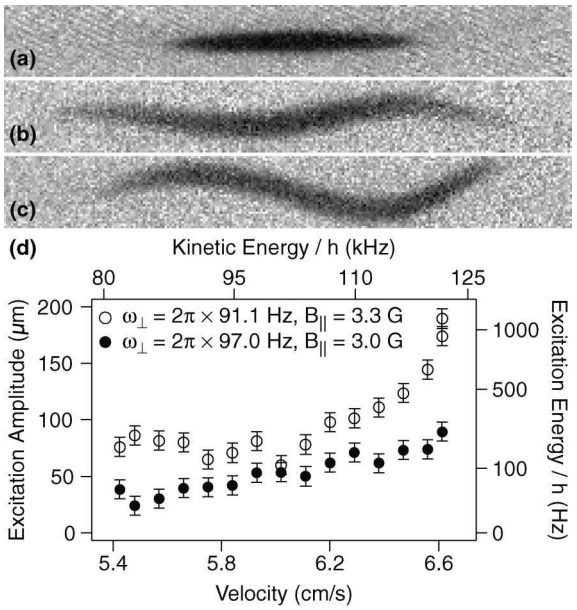

FIG. 3. Bose-Einstein condensate propagation. (a) Absorption image after 10 ms of ballistic expansion of a typical condensate just prior to entering the waveguide perturbation depicted in the inset of Fig. 1. The condensate contained 2×10^6 atoms and was accelerated to a velocity $v = 6.3$ cm/s. It had propagated over 6 mm without excitation in a waveguide with $\omega_\perp = 2\pi \times 84.5$ Hz and $B_{||} = 3.6$ G. Absorption images after 15 ms of ballistic expansion of condensates transmitted through the perturbed guiding region with $v = 6.5$ cm/s for (b) $\omega_\perp = 2\pi \times 97.0$ Hz and $B_{||} = 3.0$ G and (c) $\omega_\perp = 2\pi \times 91.1$ Hz and $B_{||} = 3.3$ G. (d) Peak-to-peak amplitudes of condensate excitations after 15 ms of ballistic expansion versus velocity. For all data $I_1 = 1200$ mA and $B_\perp = 5.4$ G. All transmitted condensates propagated 4 mm beyond the perturbed guiding region before being imaged. The field of view in (a)–(c) is 0.26 mm $\times$ 2.00 mm.

with the onset of transmission through the perturbed guiding region, as shown in Fig. 2(a). From Eq. (3) with $B_\perp = 5.4$ G, the maximum angular deviation, θ_m, of the waveguide trajectory necessary to produce a $h \times 50$ kHz perturbation to the Zeeman energy is $\theta_m = 13$ mrad. The corresponding vertical displacement of the guide center from Eq. (4) with $B_\perp = 5.4$ G, $B_{||} = 3.6$ G, and $\theta_m = 13$ mrad is 4 μm. This yields a gravitational potential variation of $h \times 2.2$ kHz, which is small compared to the Zeeman energy shifts associated with the perturbation.

In the propagation regime where the longitudinal kinetic energy of the BEC is large compared to the transverse confinement energy of the guide, perturbations involving transverse shifts in the guide trajectory are expected to transversely excite incident condensates. Figure 3 depicts such transverse excitations for condensates transmitted through the waveguide perturbation depicted in the inset of Fig. 1. The incident BEC velocity was in the range 5.4–6.6 cm/s. Excitations were characterized by the peak-to-peak amplitude of the transverse displacement of the BEC after ballistic expansion. The imaging axis only provided sensitivity to transverse excitations in the plane normal to the surface of the microchip.

The nearly sinusoidal nature of the BEC excitations shown in Figs. 3(b) and 3(c) indicates that the dipole mode of the BEC was primarily excited. Further evidence for this comes from the fact that little variation in the excitation amplitude as a function of the propagation time after exiting the perturbed guiding region was observed. Conversely, transmitted condensates showed strong signs of higher order excitations when $B_{||}$ was increased beyond 3.6 G corresponding to $\omega_\perp \leq 2\pi \times 84.5$ Hz. The absorption images deviated visibly from a smooth sinusoidal shape. In addition, the measured excitation amplitude depended strongly on propagation time, indicting the phasing and dephasing of several excitation modes.

Figure 3(d) shows a clear increase in the excitation amplitude for increasing velocity at fixed $B_{||}$ and $\omega_\perp$ as well as for increasing $B_{||}$ (decreasing $\omega_\perp$) at fixed velocity. Both trends are consistent with the expectation of increased excitations for an increased ratio of atomic longitudinal kinetic energy to transverse confinement energy. The latter trend is also consistent with the expectation of increased excitations for an increased perturbation size since, from Eq. (4), the vertical displacement of the guide center is proportional to $B_{||}$.

Because the perturbations to the magnetic potential above a single wire are due to its geometric deformations, one expects such perturbations to increase as the trap center is brought closer to the surface of the microchip. We observed longitudinal fragmentation of the BEC as the atoms were brought to within 150 μm of the surface (Fig. 4). At 55 μm from the surface the potential developed axial variations with a characteristic length scale

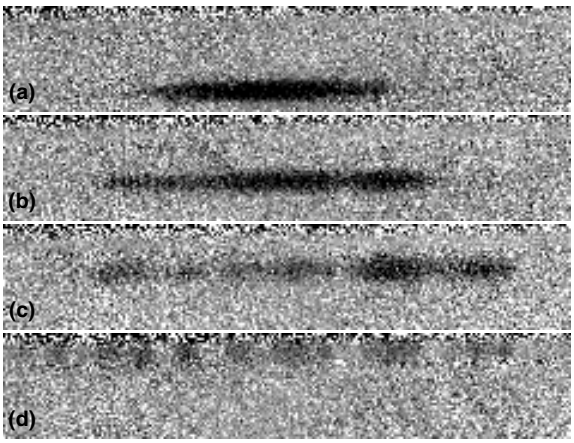

FIG. 4. Fragmented structure of Bose-Einstein condensates brought close to the substrate. Absorption images after 5 ms of ballistic expansion from the Z-wire trap shown in Fig. 1. The atom-substrate separation was (a) 190, (b) 145, (c) 100, and (d) 55 μm. For all images, the condensate started in a trap with $I_1 = I_2 = 540$ mA, $B_\perp = 5.4$ G, and $B_{||} = 0.3$ G corresponding to an atom-substrate separation of 200 μm. The condensate was translated towards the substrate by lowering the wire currents linearly over 500 ms. The atoms were held at their final position for 100 ms prior to trap shutoff. The field of view in (a)–(d) is 0.37 mm $\times$ 2.00 mm.

of 100–150 μm. These variations could be magnetic or gravitational in origin.

In conclusion, we have demonstrated the single-mode propagation of Bose-Einstein condensates in a microfabricated magnetic waveguide and identified sources of transverse excitations. Such excitations need to be addressed to realize the full potential of integrated atom-optical components fabricated on a microchip. In this work, the condensate density was large enough that the mean field energy exceeded the transverse confinement energy. In addition, the longitudinal velocity spread was determined by the mean field expansion of the cloud upon release from the Z-wire trap. The generation of more dilute clouds with narrower longitudinal velocity distributions is possible by continually draining a constant flux of atoms from the Z-wire trap serving as a reservoir. Such a matter wave source is ideal for the realization of an atom interferometer on a microchip.

We are indebted to S. Gupta for contributions to the apparatus, E. Tsikata for experimental assistance, the MIT Microsystems Technology Laboratories for fabricating the microchip used in this work, M. Prentiss and M. Vengalattore for valuable discussions, and A. D. Cronin and D. Schneble for critical readings of the manuscript. This work was funded by ONR, NSF, ARO, NASA, and the David and Lucile Packard Foundation. A. E. L. acknowledges additional support from NSF.

Note added.—Results similar to those in Fig. 4 also appear in Ref. [20]

*http://cua.mit.edu/ketterle_group/

[1] *Bose-Einstein Condensation in Atomic Gases,* Proceedings of the International School of Physics Enrico Fermi, Course CXL edited by M. Inguscio, S. Stringari, and C. E. Wieman (IOS Press, Amsterdam, 1999).

[2] J. D. Weinstein and K. G. Libbrecht, Phys. Rev. A **52**, 4004 (1995).

[3] J. H. Thywissen, M. Olshanii, G. Zabow, M. Drndić, K. S. Johnson, R. M. Westervelt, and M. Prentiss, Eur. Phys. J. D **7**, 361 (1999).

[4] J. Fortagh, A. Grossmann, C. Zimmermann, and T. W. Hänsch, Phys. Rev. Lett. **81**, 5310 (1998).

[5] J. Denschlag, D. Cassettari, and J. Schmiedmayer, Phys. Rev. Lett. **82**, 2014 (1999).

[6] M. Key, I. G. Hughes, W. Rooijakkers, B. E. Sauer, E. A. Hinds, D. J. Richardson, and P. G. Kazansky, Phys. Rev. Lett. **84**, 1371 (2000).

[7] B. K. Teo and G. Raithel, Phys. Rev. A **63**, 031402(R) (2001).

[8] P. Cren, C. F. Roos, A. Aclan, J. Dalibard, and D. Guéry-Odelin, Eur. Phys. J. D (to be published).

[9] J. Reichel, W. Hänsel, and T. W. Hänsch, Phys. Rev. Lett. **83**, 3398 (1999).

[10] D. Müller, D. Z. Anderson, R. J. Grow, P. D. D. Schwindt, and E. A. Cornell, Phys. Rev. Lett. **83**, 5194 (1999).

[11] N. H. Dekker, C. S. Lee, V. Lorent, J. H. Thywissen, S. P. Smith, M. Drndić, R. M. Westervelt, and M. Prentiss, Phys. Rev. Lett. **84**, 1124 (2000).

[12] R. Folman, P. Krüger, D. Cassettari, B. Hessmo, T. Maier, and J. Schmiedmayer, Phys. Rev. Lett. **84**, 4749 (2000).

[13] T. L. Gustavson, A. P. Chikkatur, A. E. Leanhardt, A. Görlitz, S. Gupta, D. E. Pritchard, and W. Ketterle, Phys. Rev. Lett. **88**, 020401 (2002).

[14] H. Ott, J. Fortagh, G. Schlotterbeck, A. Grossmann, and C. Zimmermann, Phys. Rev. Lett. **87**, 230401 (2001).

[15] W. Hänsel, P. Hommelhoff, T. W. Hänsch, and J. Reichel, Nature (London) **413**, 498 (2001).

[16] K. Bongs, S. Burger, S. Dettmer, D. Hellweg, J. Arlt, W. Ertmer, and K. Sengstock, Phys. Rev. A **63**, 031602(R) (2001).

[17] C. Henkel and W. Wilkens, Europhys. Lett. **47**, 414 (1999).

[18] W. Ketterle, D. S. Durfee, and D. M. Stamper-Kurn, in *Bose-Einstein Condensation in Atomic Gases* (Ref. [1]), pp. 67–176.

[19] Analogously, the trajectory will vary in a plane normal to the microchip for variations in the wire thickness.

[20] J. Fortágh, H. Ott, S. Kraft, and C. Zimmermann, cond-mat/0205310.

Appendix B

Bose-Einstein Condensates near a Microfabricated Surface

This appendix contains a reprint of Ref. [125]: A.E. Leanhardt, Y. Shin, A.P. Chikkatur, D. Kielpinski, W. Ketterle, and D.E. Pritchard, *Bose-Einstein Condensates near a Microfabricated Surface*, Phys. Rev. Lett. **90**, 100404 (2003).

Bose-Einstein Condensates near a Microfabricated Surface

A. E. Leanhardt, Y. Shin, A. P. Chikkatur, D. Kielpinski, W. Ketterle, and D. E. Pritchard*

Department of Physics, MIT-Harvard Center for Ultracold Atoms, and Research Laboratory of Electronics, Massachusetts Institute of Technology, Cambridge, Massachusetts 02139

(Received 15 November 2002; published 12 March 2003)

Magnetically and optically confined Bose-Einstein condensates were studied near a microfabricated surface. Condensate fragmentation observed in microfabricated magnetic traps was not observed in optical dipole traps at the same location. The measured condensate lifetime was ≥ 20 s and independent of the atom-surface separation under both magnetic and optical confinement. Radio-frequency spin-flip transitions driven by technical noise were directly observed for optically confined condensates and could limit the condensate lifetime in microfabricated magnetic traps.

DOI: 10.1103/PhysRevLett.90.100404 PACS numbers: 03.75.Nt, 03.75.Be, 34.50.Dy, 39.20.+q

The manipulation of gaseous Bose-Einstein condensates with magnetic fields produced by wires microfabricated on material surfaces has opened a new frontier in the field of atom optics [1–4]. Magnetic confinement using microfabricated wires is tighter and has higher spatial resolution than is achievable in macroscopic magnetic traps [5–8]. Generally, an important feature of magnetic traps is the excellent thermal isolation between the nanokelvin temperature clouds they confine and the 300 K laboratory environment. However, decreasing the atom-surface separation into the micrometer range has raised concerns that fluctuating surface currents may perturb the atoms [9,10]. While early demonstrations of trapping and guiding laser-cooled thermal atoms with microfabricated devices reported no evidence of deleterious surface effects [11–14], recent studies using samples cooled by forced radio-frequency (rf) evaporation to $\lesssim 2\ \mu$K have found corrugated potentials [3,15], large heating rates [2,15], and short trap lifetimes [2,15] for atom-surface separations in the 100 μm regime. The ultimate applicability of microfabricated devices to atom optics depends on the characterization and elimination of such effects.

In this work, we experimentally investigate the behavior of Bose-Einstein condensates near a microfabricated surface. The condensates were confined at the same position relative to the surface by either a microfabricated magnetic trap or an optical dipole trap. Since the two traps operate on different principles and the electromagnetic fields for each have different sources, this study provides a unique examination of the interaction between Bose-Einstein condensates and a microfabricated surface. For example, while condensates confined near the surface in a microfabricated magnetic trap were found to fragment longitudinally [3,15], the clouds remained intact under optical confinement.

Significantly, the measured condensate lifetime in both the microfabricated magnetic trap and the optical dipole trap was ≥ 20 s, an order of magnitude longer than previous results [2,15], and independent of the atom-surface separation. We have directly observed spin-flip transitions driven by rf technical noise for condensates held in the optical dipole trap. The transition rate increased rapidly with decreasing atom-surface separation implying that distance-dependent losses can occur in magnetic traps where the products of such transitions cannot be directly identified.

Bose-Einstein condensates containing over 10^7 ^{23}Na atoms were created in the $|F = 1, m_F = -1\rangle$ state in a macroscopic Ioffe-Pritchard magnetic trap, loaded into the focus of an optical tweezers beam, and transported ≈ 32 cm in 2 s into an auxiliary "science" chamber as described in Ref. [16]. The optical tweezers consisted of ≈ 50 mW of 1064 nm laser light focused to a $1/e^2$ radius of 26 μm. This resulted in axial and radial trap frequencies $\omega_{||} = 2\pi \times 4$ Hz and $\omega_{\perp} = 2\pi \times 425$ Hz, respectively, and a trap depth of 2.5 μK. Condensates containing $(2–3) \times 10^6$ atoms arrived 70–500 μm below the microfabricated structures mounted in the science chamber. The atom-surface separation was varied by angling the optical tweezers axis before translation and was limited to distances $\geq 70\ \mu$m due to the laser beam clipping on the microchip support structures.

In the science chamber, the condensate either remained confined by the optical tweezers or was loaded into a microfabricated Ioffe-Pritchard magnetic trap formed by a Z-shaped wire carrying current I and an external magnetic bias field, $B_{\perp}$, as described in Ref. [3]. An additional longitudinal bias field, $B_{||}$, was applied with external coils to adjust the magnetic trap bottom and radial trap frequency. The microfabricated wires were lithographically patterned on a 600 μm thick silicon substrate mounted on an aluminum block. They were 50 μm wide and electroplated with copper to a thickness of 10 μm.

As in previous experiments [3,15], condensates confined near the surface in the microfabricated magnetic trap were observed to fragment longitudinally [Fig. 1(a)]. The condensate density depletions appeared in the same longitudinal position relative to the surface on each realization of the experiment, and more fragments formed as the atoms came closer to the microchip [3]. In contrast, condensates confined optically at the same location were not observed to fragment [Fig. 1(b)]. The same

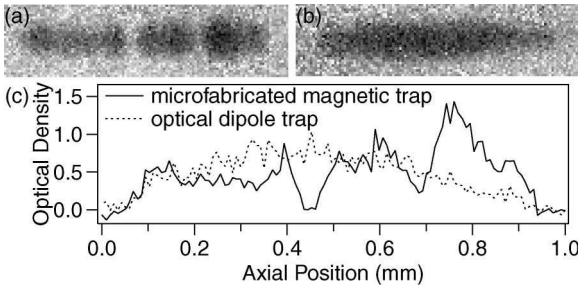

FIG. 1. Fragmentation of Bose-Einstein condensates. Transverse absorption images after 10 ms ballistic expansion of condensates containing $\approx 10^6$ atoms after holding at a distance of 85 μm from the microfabricated surface for 15 s in the (a) microfabricated magnetic trap and (b) optical dipole trap. (c) Radially averaged optical density vs axial position for condensates shown above. Longitudinal fragmentation occurred for condensates held in the microfabricated magnetic trap, but not for those confined optically at the same location with the magnetic trap off. The magnetic trap was operated with $I = 130$ mA, $B_\perp = 3.2$ G, and $B_{||} = 1.4$ G yielding a radial trap frequency $\omega_\perp = 2\pi \times 450$ Hz. The optical dipole trap had a radial trap frequency $\omega_\perp = 2\pi \times 425$ Hz and was operated with $B_{||} = 1.8$ G. For both condensates, the chemical potential was $\mu = k_B \times 120$ nK. The absorption imaging light was resonant with the $F = 1 \rightarrow F' = 2$ transition. The field of view in (a) and (b) is 0.25 mm $\times$ 1.00 mm.

longitudinal bias field was nominally applied to both magnetically and optically confined condensates so that any surface magnetization effects would perturb the clouds identically. The lack of condensate fragmentation in the optical dipole trap implies that the longitudinal potential corrugations arise due to the presence of current flow in the microfabricated wires, in agreement with conclusions reached elsewhere [17]. Deviations of the current flow from a straight line would lead to such corrugations and could arise due to imperfect microfabrication including variations in the width and thickness of the wire estimated to be 5% of the electroplated thickness, variations in the resistivity of the wire over its cross section, and parasitic conductances to the substrate. Other possible origins of irregular current flow are instabilities at high current density [17].

It is interesting to note that in our earlier work no fragmentation was observed when condensates confined in a macroscopic Z-shaped wire trap were brought within ≈ 10 μm of the surface of the wire [16]. The wire was made of copper and had a circular cross section with 1.27 mm diameter. The condensates were loaded into the wire trap 740 μm from the surface of the wire and brought closer by lowering the wire current. The experimental parameters upon closest approach were $I = 920$ mA and $B_\perp = 2.9$ G, yielding estimated axial and radial trap frequencies $\omega_{||} = 2\pi \times 7$ Hz and $\omega_\perp = 2\pi \times 78$ Hz, respectively [18]. The macroscopic wire trap contained 5×10^5 atoms extended longitudinally over 200 μm at a chemical potential $\mu = k_B \times 30$ nK. Differences between the macroscopic and microfabricated wire traps include vastly different fabrication techniques as well as lower current densities in the macroscopic wire.

Confined atoms are sensitive to noise at their trap frequency and Zeeman splitting frequency [9,10]. In this work, typical radial trap frequencies were ≈ 500 Hz while Zeeman splitting frequencies were ≈ 1 MHz. Noise at the trap frequency leads to heating and subsequent trap loss after the atoms acquire an energy greater than the trap depth. For atoms confined in a Ioffe-Pritchard magnetic trap, radial magnetic bias field fluctuations cause radial trap-center fluctuations. The amplitude of such trap-center fluctuations is independent of the longitudinal bias field. However, for optically confined atoms, only fluctuating radial magnetic field *gradients* cause radial trap-center fluctuations. The effects of such gradients can be minimized by applying a longitudinal bias field that adds in quadrature with the fluctuating radial gradients since it is the gradient of the magnitude of the bias field vector that determines the force on an atom.

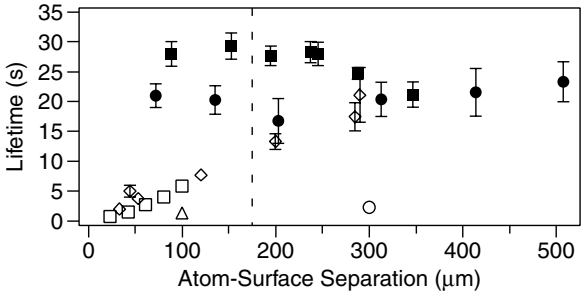

FIG. 2. Lifetime of Bose-Einstein condensates near a microfabricated surface. The $1/e$ lifetime of condensates confined in the microfabricated magnetic trap (solid squares) and optical dipole trap (solid circles) is shown to be independent of distance from the microfabricated surface. Statistical error bars are included. Additionally, excitations created while transferring the condensate from the optical tweezers into the microfabricated magnetic trap caused fluctuations in the measured magnetic trap lifetime, indicated by the scatter in the data. I and $B_\perp$ were varied with distance to maintain the radial magnetic trap frequency at $\omega_\perp = 2\pi \times 450$ Hz with $B_{||} = 1.4$ G. The vertical line indicates the onset of longitudinal condensate fragmentation in the magnetic trap. In the optical dipole trap, the condensate was held directly below the microfabricated wire used to form the magnetic trap with $B_{||} = 1.8$ G. No external connections were made to the microchip. The optical dipole trap had axial and radial trap frequencies $\omega_z = 2\pi \times 4$ Hz and $\omega_\perp = 2\pi \times 425$ Hz, respectively. Only atoms remaining in the $|1, -1\rangle$ state were resonant with the absorption imaging light. For comparison, the distance dependence of thermal cloud lifetimes measured in Ref. [15] is shown for atoms confined magnetically by a microstructure (open squares) and copper wire (open diamonds). Error bars smaller than the symbol size are not included. Also, magnetically confined condensate lifetimes reported in Ref. [2] (open triangle) and Ref. [15] (open circle) are shown for comparison.

Spin-flip transitions driven by rf noise at the atomic Zeeman splitting frequency distribute the atomic population across magnetically confinable and unconfinable states. This causes atom loss for clouds held in magnetic traps. However, all spin states are confined in an optical dipole trap so spin-flip transitions do not lead to loss and the products can be directly observed. Since magnetically and optically confined condensates react differently to noise, whether it is at their trap frequency or the atomic Zeeman splitting frequency, a systematic study of condensate lifetimes in both magnetic and optical traps provides better noise characterization than studies performed in either a magnetic or an optical trap exclusively.

Any atom-surface coupling, regardless of frequency, should manifest itself as a dependence of the condensate lifetime on the atom-surface separation. Figure 2 shows a measurement of the magnetically and optically confined condensate lifetime as a function of the distance from the microfabricated surface. No distance dependence was observed and the measured condensate lifetime was ≥ 20 s, 10 times longer than previous results [2,15]. A distance independent condensate lifetime indicates that atom-surface interactions are unimportant over the 70–500 μm separation range. This is in contrast to results presented in Ref. [15], where a distance-dependent lifetime was observed for thermal atoms magnetically confined near a microfabricated surface. These data are included in Fig. 2 for comparison.

Several experimental details altered the measured condensate lifetime. Excitations created during the microfabricated magnetic trap loading were found to shorten the measured lifetime, and care had to be taken to overlap the optical and magnetic traps during transfer to minimize such excitations. Translating the condensate either towards or away from the microfabricated surface by adiabatically varying I and $B_\perp$ to shift the trap center while maintaining a constant radial trap frequency was found to decrease the condensate lifetime. This presumably resulted from excitations induced by irregular current changes due to technical limitations in controlling the power supplies connected to the microchip. As a result, microfabricated magnetic trap lifetime data are presented only for atom-surface separations ≥ 70 μm, where the atoms were loaded into their final position directly from the optical tweezers. Occasionally, heating was observed for atoms in both the microfabricated magnetic trap and optical dipole trap due to technical noise at the trap frequency, even with care taken to eliminate ground loops and minimize cable lengths [19]. Connecting a 10 mF capacitor in parallel with the 2 Ω microfabricated wire ($1/RC = 2\pi \times 8$ Hz) eliminated such effects. Thereafter, applying rf power to the microchip at a frequency chosen to limit the trap depth for magnetically confined atoms did not consistently alter the condensate lifetime.

The distance independent condensate lifetime presented in Fig. 2 indicates that our experiment is not currently limited by the proximity of the microfabricated surface. However, we have observed spin-flip transitions driven by rf noise in the microfabricated wires. Figure 3 shows the behavior of condensates confined optically directly beneath the microfabricated wire used for magnetic trapping. Condensate atoms initially in the $|1, -1\rangle$ state [Fig. 3(a)] were found to make transitions to other magnetic sublevels [Fig. 3(b)]. Such transitions would act as a loss mechanism for magnetically confined clouds. The transition rate was found to decrease as the square of the atom-surface separation distance, d. Since the magnetic field of a straight wire decays as $1/d$, and the power scales as the square of the field, the $1/d^2$ dependence of the spin-flip transition rate is expected for atoms in the near field ($d \ll \lambda$) of the wire, where $\lambda \approx 300$ m is the wavelength of ≈ 1 MHz radiation.

The transition rate vs distance data presented in Fig. 3(c) were taken with all connections necessary to run the microfabricated magnetic trap made to the microchip, but with no current flowing in the microfabricated wires. The atoms were exposed to a longitudinal bias field $B_{||} = 1.8$ G to simulate the field configuration in the microfabricated magnetic trap. This also maximized their

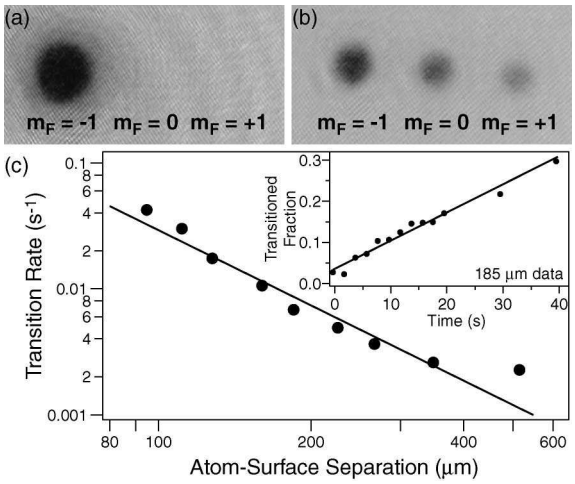

FIG. 3. Spin-flip transitions driven by radio-frequency technical noise. Axial absorption images after 22 ms ballistic expansion of condensates held in the optical dipole trap at a distance of 185 μm from the microfabricated surface for (a) 0 s and (b) 40 s. A magnetic field gradient was applied during ballistic expansion to separate the different spin states. (c) Spin-flip transition rate, Γ, vs distance, d, from the microfabricated surface on a log-log scale. A line $\Gamma \propto 1/d^2$ is provided as a guide. The inset shows the fraction of the total atoms in the $m_F = 0$ state with the transition rate being defined as the initial slope of the data (before any atoms in the $m_F = +1$ state were detected). The absorption imaging light was resonant with the $F = 2 \rightarrow F' = 3$ transition. The atoms were optically pumped into the $F = 2$ hyperfine level with a pulse resonant with the $F = 1 \rightarrow F' = 2$ transition. This provided equal imaging sensitivity to each magnetic sublevel. The field of view in (a) and (b) is 1.0 mm $\times$ 2.0 mm.

sensitivity to fluctuating fields generated by wire currents since rf transitions are more favorable for magnetic fields oscillating orthogonal to a static bias field. Spin-flip transitions were suppressed by exposing the optically confined atoms to an orthogonal bias field, $B_\perp$.

The rf driven spin-flip transition rate depended strongly on experimental details, suggesting that antenna effects coupled rf noise into the system. The rate was measured to be of order 100 times higher if care was not taken to carefully eliminate ground loops and use minimal cable lengths [19]. Also, with no connections to the microchip, spin-flip transitions were not detectable for condensates held up to 60 s. The spin-flip rate presented in Fig. 3(c) became comparable to the measured condensate decay rate displayed in Fig. 2 for atom-surface separations <100 μm. Thus, extending long condensate lifetimes much closer to the surface will require further rf shielding and/or filtering.

In conclusion, we have studied the behavior of Bose-Einstein condensates near a microfabricated surface. Condensates found to fragment while held in a microfabricated magnetic trap were observed to remain intact while held at the same position relative to the microchip in an optical dipole trap. A possible explanation is that deviations of the current path from a straight line give rise to corrugations in the longitudinal potential. The origins of such current path deviations are under investigation. Furthermore, our work demonstrates magnetically and optically confined condensate lifetimes ≥ 20 s at distances ≥ 70 μm from a microfabricated surface. The lifetime was measured to be independent of the atom-surface separation and 10 times longer than results obtained elsewhere at comparable distances. Spin-flip transitions driven by rf technical noise were directly observed for condensates held in an optical dipole trap; however, we found no evidence for fundamental, thermally induced noise driven processes above the level of those attributed to technical noise. Our results demonstrate the extreme sensitivity of Bose-Einstein condensates to small static and dynamic electromagnetic fields. This sensitivity provides a challenge for realizing microfabricated atom-optical devices, but it also emphasizes the potential for developing new detector and instrumentation technology.

We thank T. Pasquini for experimental assistance and M. Crescimanno for a critical reading of the manuscript. This work was funded by ONR, NSF, ARO, NASA, and the David and Lucile Packard Foundation. A. E. L. acknowledges additional support from NSF.

Note added.—Recently, we have observed condensate fragmentation near conductors 50 μm wide and evaporated with gold to a thickness of 1.25 μm. This shows that the fragmentation phenomena are not limited to copper conductors, in agreement with conclusions reached elsewhere [20]. Also, Ref. [20] reports magnetic trap lifetimes limited by thermally induced spin flips.

*Electronic address: http://cua.mit.edu/ketterle_group/

[1] H. Ott, J. Fortagh, G. Schlotterbeck, A. Grossmann, and C. Zimmermann, Phys. Rev. Lett. **87**, 230401 (2001).
[2] W. Hänsel, P. Hommelhoff, T.W. Hänsch, and J. Reichel, Nature (London) **413**, 498 (2001).
[3] A. E. Leanhardt, A. P. Chikkatur, D. Kielpinski, Y. Shin, T. L. Gustavson, W. Ketterle, and D. E. Pritchard, Phys. Rev. Lett. **89**, 040401 (2002).
[4] S. Schneider, A. Kasper, Ch. vom Hagen, M. Bartenstein, B. Engeser, T. Schumm, I. Bar-Joseph, R. Folman, L. Feenstra, and J. Schmiedmayer, Phys. Rev. A **67**, 023612 (2003).
[5] J. D. Weinstein and K. G. Libbrecht, Phys. Rev. A **52**, 4004 (1995).
[6] J. Schmiedmayer, Eur. Phys. J. D **4**, 57 (1998).
[7] J. H. Thywissen, M. Olshanii, G. Zabow, M. Drndić, K. S. Johnson, R. M. Westervelt, and M. Prentiss, Eur. Phys. J. D **7**, 361 (1999).
[8] E. A. Hinds and I. G. Hughes, J. Phys. D **32**, R119 (1999).
[9] C. Henkel and M. Wilkens, Europhys. Lett. **47**, 414 (1999).
[10] C. Henkel, S. Pötting, and M. Wilkens, Appl. Phys. B **69**, 379 (1999).
[11] J. Reichel, W. Hänsel, and T.W. Hänsch, Phys. Rev. Lett. **83**, 3398 (1999).
[12] D. Müller, D. Z. Anderson, R. J. Grow, P. D. D. Schwindt, and E. A. Cornell, Phys. Rev. Lett. **83**, 5194 (1999).
[13] N. H. Dekker, C. S. Lee, V. Lorent, J. H. Thywissen, S. P. Smith, M. Drndić, R. M. Westervelt, and M. Prentiss, Phys. Rev. Lett. **84**, 1124 (2000).
[14] R. Folman, P. Krüger, D. Cassettari, B. Hessmo, T. Maier, and J. Schmiedmayer, Phys. Rev. Lett. **84**, 4749 (2000).
[15] J. Fortágh, H. Ott, S. Kraft, A. Günther, and C. Zimmermann, Phys. Rev. A **66**, 041604(R) (2002).
[16] T. L. Gustavson, A. P. Chikkatur, A. E. Leanhardt, A. Görlitz, S. Gupta, D. E. Pritchard, and W. Ketterle, Phys. Rev. Lett. **88**, 020401 (2002).
[17] S. Kraft, A. Günther, H. Ott, C. Zimmermann, and J. Fortágh, J. Phys. B **35**, L469 (2002).
[18] The axial and radial trap frequencies were scaled from the frequencies measured with $I = 2.0$ A in Ref. [16] by $(0.92\ \text{A}/2.0\ \text{A})^{1/2}$ and $2.0\ \text{A}/0.92$ A, respectively.
[19] The current supply for the microfabricated wire and the wire itself were grounded to the vacuum chamber at the location of the electrical feedthrough for the microchip connections. The total length of all (unshielded) current carrying cables was ≈ 1 m.
[20] M. P. A. Jones, C. J. Vale, D. Sahagun, B. V. Hall, and E. A. Hinds, quant-ph/0301018.

Appendix C

Atom Interferometry with Bose-Einstein Condensates in a Double-Well Potential

This appendix contains a preprint of Ref. [199]: Y. Shin, M. Saba, T.A. Pasquini, W. Ketterle, D.E. Pritchard, and A.E. Leanhardt, *Atom Interferometry with Bose-Einstein Condensates in a Double-Well Potential*, arXiv:cond-mat/0306305 (2003).

Atom interferometry with Bose-Einstein condensates in a double-well potential

Y. Shin, M. Saba, T. A. Pasquini, W. Ketterle, D. E. Pritchard, and A. E. Leanhardt*
Department of Physics, MIT-Harvard Center for Ultracold Atoms, and Research Laboratory of Electronics, Massachusetts Institute of Technology, Cambridge, Massachusetts, 02139
(Dated: July 17, 2003)

A trapped-atom interferometer was demonstrated using gaseous Bose-Einstein condensates coherently split by deforming an optical single-well potential into a double-well potential. The relative phase between the two condensates was determined from the spatial phase of the matter wave interference pattern formed upon releasing the condensates from the separated potential wells. Coherent phase evolution was observed for condensates held separated by 13 μm for up to 5 ms and was controlled by applying ac Stark shift potentials to either of the two separated condensates.

PACS numbers: 03.75.Dg, 39.20.+q, 03.75.-b, 03.75.Lm

Demonstrating atom interferometry with particles confined by magnetic [1, 2, 3, 4] and optical [5] microtraps and waveguides would realize the matter wave analog of optical interferometry using fiber-optic devices. Current proposals for confined-atom interferometers rely on the merger and separation of two potential wells to coherently divide atomic wavepackets [6, 7, 8]. This type of division differs from previously demonstrated atomic beam splitters. To date, atomic beams and vapors have been coherently diffracted into different momentum states by mechanical [9, 10] and optical [11] gratings, and Bose-Einstein condensates have been coherently delocalized over multiple sites in optical lattices [12, 13, 14, 15, 16, 17]. Atom interferometers utilizing these beam splitting elements have been used to sense accelerations [12, 18] and rotations [19, 20], monitor quantum decoherence [21], characterize atomic and molecular properties [22], and measure fundamental constants [18, 23].

In this Letter, we demonstrate a trapped-atom interferometer with gaseous Bose-Einstein condensates confined in an optical double-well potential. Condensates were coherently split by deforming an initially single-well potential into two wells separated by 13 μm. The relative phase between the two condensates was determined from the spatial phase of the matter wave interference pattern formed upon releasing the atoms from the separated potential wells [17, 24]. This recombination method avoids deleterious mean field effects [25, 26] and detects applied phase shifts on a single realization of the experiment, unlike in-trap recombination schemes [6, 7, 8].

The large separation between the split potential wells allowed the phase of each condensate to evolve independently and either condensate to be addressed individually. An ac Stark phase shift was applied to either condensate by temporarily turning off the optical fields generating its potential well. The spatial phase of the resulting matter wave interference pattern shifted linearly with the applied phase shift and was independent of the time of its application. This verified the phase sensitivity of the interferometer and the independent phase evolution of the separated condensates. The measured coherence time of the separated condensates was 5 ms.

The present work demonstrates a trapped-atom interferometer with two interfering paths. This geometry has the flexibility to measure either highly localized potentials or uniform potential gradients, such as those arising from atom-surface interactions or the earth's gravitational field, respectively. In contrast, multiple-path interferometers demonstrated in optical lattice systems are restricted to measurements of the latter [12, 17].

Bose-Einstein condensates containing over 10^7 ^{23}Na atoms were created in the $|F = 1, m_F = -1\rangle$ state in a magnetic trap, captured in the focus of a 1064 nm optical tweezers laser beam, and transferred into an auxiliary "science" chamber as described in Ref. [27]. In the science chamber, the condensate was loaded from the optical tweezers into the interferometer's single-well optical trap formed by a counter-propagating, orthogonally-polarized 1064 nm laser beam shifted in frequency from the tweezers by ~ 100 MHz to avoid interference effects.

A schematic diagram of the setup for the interferometer's optical trap is shown in Fig. 1(a). The optical potentials were derived from a collimated laser beam that passed through an acousto-optic modulator (AOM) and was focused onto the condensate with a lens. The AOM was driven by two radio frequency (rf) signals to create the double-well potential. The separation between the potential wells was controlled by the frequency difference between the rf drives. The $1/e^2$ radius of each focused beam was 5 μm. For typical optical powers, this resulted in a single beam trap depth $U_0 = h \times 5$ kHz, where h is Planck's constant, and a radial (axial) trap frequency $f_r = 615$ Hz ($f_z = 30$ Hz).

The condensate was initially loaded into the single-well trap shown in Fig. 1(b). After holding the cloud in this trap for 15 s to damp excitations, the peak atomic mean field energy was $\tilde{\mu}_0 \approx h \times 3$ kHz. The single-well trap was deformed into the double-well potential shown in Fig. 1(c) by linearly increasing the frequency difference between the rf signals driving the AOM in 5 ms. The amplitude of the rf signals were tailored during the splitting

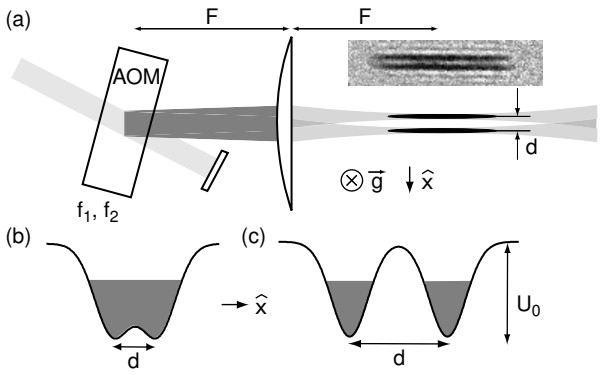

FIG. 1: (a) Schematic diagram of the optical setup for the double-well potential. An acousto-optic modulator (AOM) was driven by two frequencies, f_1 and f_2, and diffracted a collimated beam into two beams. The AOM was placed in the focal plane of a lens of focal length F so that the two beams propagated parallel to each other. The radial separation of the potential wells, d, was controlled by the frequency difference, $\Delta f = |f_1 - f_2|$. $\vec{g}$ denotes the direction of gravitational acceleration. The absorption image shows two well-separated condensates confined in the double-well potential diagramed in (c). The field of view is 70 μm $\times$ 300 μm. Energy diagrams for (b) initial single-well trap with $d = 6$ μm and (c) final double-well trap with $d = 13$ μm. In both (b) and (c), $U_0 = h \times 5$ kHz and the peak atomic mean field energy was $\sim h \times 3$ kHz. The potential "dimple" in (b) was $< h \times 500$ Hz which was much less than the peak atomic mean field energy allowing the trap to be characterized as a single-well. The potential "barrier" in (c) was $h \times 4.7$ kHz which was larger than the peak atomic mean field energy allowing the resulting split condensates to be characterized as independent.

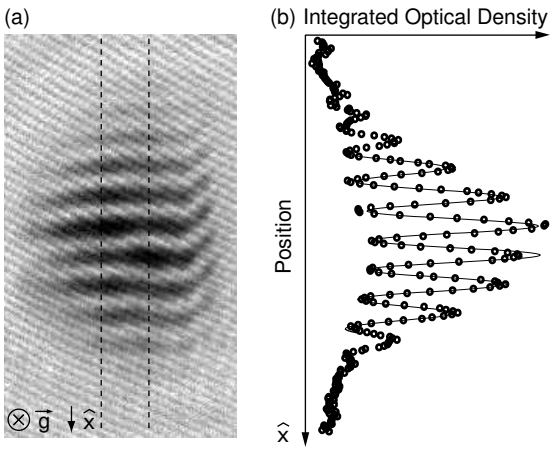

FIG. 2: Matter wave interference. (a) Absorption image of condensates released from the double-well potential in Fig. 1(c) and allowed to overlap during 30 ms of ballistic expansion. The imaging axis was parallel to the direction of gravitational acceleration, $\vec{g}$. The field of view is 600 μm $\times$ 350 μm. (b) Radial density profiles were obtained by integrating the absorption signal between the dashed lines, and typical images gave $> 60\%$ contrast. The solid line is a fit to a sinusoidally-modulated Gaussian curve from which the phase of the interference pattern was extracted (see text).

process to guarantee an even division of the condensate atoms and nearly equal trap depths after splitting.

The key achievement of this work was the reproducibility of the spatial phase of the matter wave interference pattern on each realization of the experiment. Figure 2 shows a typical matter wave interference pattern formed by the condensates released from the double-well potential. The reproducibility directly confirmed that deforming the optical potential from a single-well into a double-well coherently split the condensate into two clouds with deterministic relative phase. While past work suffered from an unstable potential barrier separating the two condensates and irreproducible turn off a high current magnetic trap to initiate ballistic expansion [24], the current experiment derived its double-well potential from a single laser beam. Thus, vibrations and fluctuations of the laser beam were common-mode to both wells and a clean and rapid trap turn off was achieved.

The condensates were sufficiently separated that their phases evolved independent of each other to the extent that no coupling between the potential wells could be detected. This claim is supported qualitatively by the absorption image in Fig. 1(a) and the observation of high-contrast matter wave interference patterns that penetrated the full atomic density profile with uniform spatial period and no thick central fringe [28], and quantitatively by measurements of the phase evolution (Figs. 3 and 4).

The relative phase between the two separated condensates was determined by the spatial phase of their matter wave interference pattern. For a ballistic expansion time $t \gg 1/f_r$, each condensate had a quadratic phase profile [29], $\psi_\pm(\vec{r},t) = \sqrt{n_\pm(\vec{r},t)}\exp(i\frac{m}{2\hbar t}|\vec{r} \pm \vec{d}/2|^2 + \phi_\pm)$, where $\pm$ denotes one well or the other, $n_\pm$ is the condensate density, $\hbar = h/2\pi$, m is the atomic mass, and $\phi_\pm$ is the condensate phase. This resulted in a total density profile for the matter wave interference pattern

$$n(\vec{r},t) = (n_+ + n_- + 2\sqrt{n_+ n_-}\cos(\frac{md}{\hbar t}x + \phi_r)), \quad (1)$$

where $\phi_r = \phi_+ - \phi_-$ is the relative phase between the two condensates and $\vec{d} = d\hat{x}$. To extract ϕ_r, the integrated cross section shown in Fig. 2(b) was fit with a sinusoidally-modulated Gaussian curve, $G(x) = A\exp(-(x-x_c)^2/\sigma^2)(1 + B\cos(\frac{2\pi}{\lambda}(x-x_0) + \phi_f))$, where ϕ_f is the phase of the interference pattern with respect to a chosen fixed x_0. Ideally, if x_0 was set at the center of the two wells, then $\phi_r = \phi_f$. However, misalignment of the imaging axis with the direction of gravitational acceleration created a constant offset, $\phi_f = \phi_r + \delta\phi$. With $t = 30$ ms the measured fringe period, $\lambda = 41.5$ μm, was within 4% of the point source formula prediction [Eq. (1)], $ht/md = 39.8$ μm.

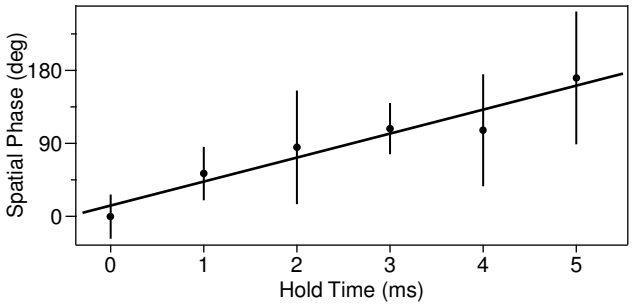

FIG. 3: Phase coherence of the separated condensates. The spatial phase of the interference pattern is plotted versus hold time after splitting. Each point represents the average of eight measurements, and the error bars are ± one standard deviation. The phase evolution was due to unequal trap depths for the two wells, which was determined from the linear fit to be $h \times 70$ Hz or $\sim 1\%$ of the trap depth.

The coherent phase evolution of the split condensates is displayed quantitatively in Figs. 3 and 4. The relative phase, ϕ_r, between the separated condensates was observed to evolve linearly in time and the standard deviation of eight measurements of ϕ_f was < 90 degrees up to 5 ms after splitting (Fig. 3). Furthermore, for hold times between 0 and 1 ms, the standard deviation was substantially smaller, < 40 degrees. Since ϕ_r distributed randomly between -180 and $+180$ degrees would have a standard deviation of ~ 104 degrees, the results in Figs. 3 and 4 clearly demonstrate that the separated condensates had a reproducible relative phase after splitting. The linear time evolution of ϕ_r was due to a chemical potential difference between separated condensates and could be controlled by varying the trap depths of the individual potential wells after splitting.

Fundamental limits on the phase coherence between isolated condensates arise due to Poissonian number fluctuations associated with the coherent state description of the condensate [30, 31, 32]. For our experimental parameters, the time scale for phase diffusion was ~ 200 ms. The uncertainty in determining ϕ_f at longer hold times > 5 ms is attributed to axial and breathing-mode excitations created during the splitting process. These excitations lead to interference fringes that were angled and had substantial curvature, rendering a determination of ϕ_f impossible. Splitting the condensate more slowly in an effort to minimize excitations, but still fast compared to the phase diffusion time, did not improve the measured stability of ϕ_f. Since controlling axial excitations appears critical for maintaining phase coherence, splitting condensates that are freely propagating in a waveguide potential may be more promising [3].

The phase sensitivity of the trapped-atom interferometer was demonstrated by applying ac Stark phase shifts to either (or both) of the two separated condensates. Phase shifts were applied to individual condensates by pulsing off the optical power generating the corresponding potential well for a duration $\tau_p \ll 1/f_r$. Figure 4(a) shows that the spatial phase of the matter wave interference pattern shifted linearly with the pulse duration, as expected. Due to the inhomogeneous optical potential, $U(r)$, the applied ac Stark phase shifts varied across the condensate as $\Delta\phi(r) = -U(r)\tau_p/\hbar$. Averaging this phase shift over the inhomogeneous condensate density, $n(\vec{r})$, approximates the expected spatial phase shift of the matter wave interference pattern as $\Delta\bar{\phi} = \frac{1}{N}\int d^3\vec{r}\; n(\vec{r})\Delta\phi(\vec{r}) = (U_0 - \frac{2}{7}\tilde{\mu}_0)\Delta t/\hbar$, where N is the number of atoms, and U_0 and $\tilde{\mu}_0$ are the trap depth and mean field energy at the center of each potential well, respectively. The measured phase shifts yielded $U_0 = h \times 5$ kHz [Fig. 4(b)], which was consistent with calculations based on other measured trap parameters.

The measured phase shifts of the matter wave interference depended only on the time-integral of the applied ac Stark phase shifts [Fig. 4(b)], as expected for uncoupled condensates. The final relative phase, ϕ_r, should be the same on different phase trajectories because the history of phase accumulation does not affect the total amount of accumulated phase. For coupled condensates, Josephson oscillations between the wells would cause the relative phase to vary nonlinearly with time [25, 29] and produce a time dependent signal in Fig. 4(b). Due to the large well separation and mean field energy $h \times 1.7$ kHz below the barrier height, the single-particle tunnelling rate in our system was extremely low ($\lesssim 10^{-3}$ Hz) [29], and the condensates were effectively uncoupled.

In conclusion, we have performed atom interferometry with Bose-Einstein condensates confined in an optical double-well potential. A coherent condensate beam splitter was demonstrated by deforming a single-well potential into a double-well potential. The large spatial separation between the potential wells guaranteed that each condensate evolved independently and allowed for addressing each condensate individually. Recombination was performed by releasing the atoms from the double-well potential and allowing them to overlap while expanding ballistically. Implementing a similar readout scheme with magnetic potentials generated by microfabricated current carrying wires should be possible and would eliminate deleterious mean field effects inherent in proposals using in-trap wavepacket recombination. Propagating the separated condensates along a waveguide prior to phase readout would create an atom interferometer with an enclosed area, and hence with rotation sensitivity.

We thank W. Jhe, C. V. Nielsen, and A. Schirotzek for experimental assistance and S. Gupta, Z. Hadzibabic, and M. W. Zwierlein for critical comments on the manuscript. This work was funded by ARO, NSF, ONR, and NASA. M.S. acknowledges additional support from the Swiss National Science Foundation.

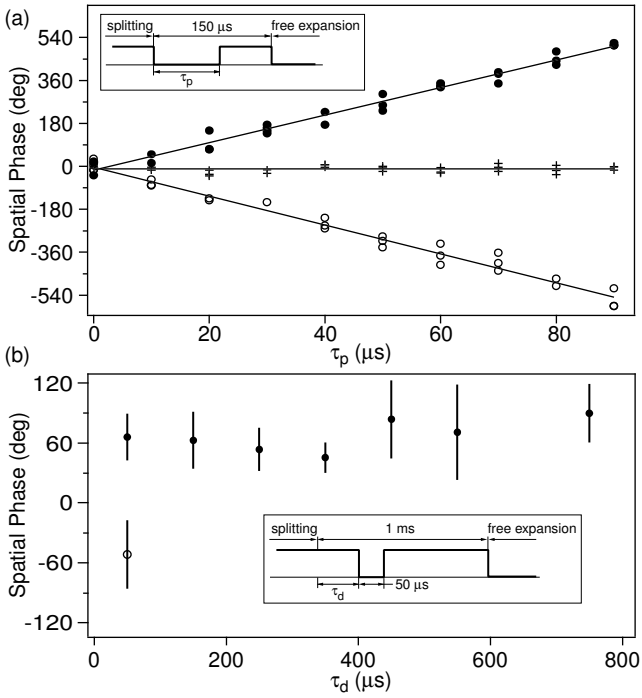

FIG. 4: Trapped-atom interferometry. (a) ac Stark phase shifts were applied to either well exclusively (solid circles and open circles) or both wells simultaneously (crosses) by turning off the corresponding rf signal(s) driving the AOM for a duration τ_p. The resulting spatial phase of the matter wave interference pattern scaled linearly with τ_p and hence the applied phase shift. Applying the ac Stark shift to the opposite well (solid versus open circles) resulted in an interference pattern phase shift with opposite sign. Applying ac Stark shifts to both wells (crosses) resulted in no phase shift for the interference pattern. This data was taken with a slightly modified experimental setup such that the trap depth of the individual potential wells was $U_0 = h \times 17$ kHz. (b) A 50 μs pulse induced a 70 degree shift independent of the pulse position. The experimental setup was as described in Fig. 1. Solid and open circles have the same meaning as in (a). The insets show the time sequence of the optical intensity for the well(s) temporarily turned off.

* URL: `http://cua.mit.edu/ketterle_group/`

[1] H. Ott, J. Fortagh, G. Schlotterbeck, A. Grossmann, and C. Zimmermann, Phys. Rev. Lett. **87**, 230401 (2001).

[2] W. Hänsel, P. Hommelhoff, T. W. Hänsch, and J. Reichel, Nature **413**, 498 (2001).

[3] A. E. Leanhardt, A. P. Chikkatur, D. Kielpinski, Y. Shin, T. L. Gustavson, W. Ketterle, and D. E. Pritchard, Phys. Rev. Lett. **89**, 040401 (2002).

[4] S. Schneider, A. Kasper, C. vom Hagen, M. Bartenstein, B. Engeser, T. Schumm, I. Bar-Joseph, R. Folman, L. Feenstra, and J. Schmiedmayer, Phys. Rev. A **67**, 023612 (2003).

[5] R. Dumke, T. Müther, M. Volk, W. Ertmer, and G. Birkl, Phys. Rev. Lett. **89**, 220402 (2002).

[6] E. A. Hinds, C. J. Vale, and M. G. Boshier, Phys. Rev. Lett. **86**, 1462 (2001).

[7] W. Hänsel, J. Reichel, P. Hommelhoff, and T. W. Hänsch, Phys. Rev. A **64**, 063607 (2001).

[8] E. Andersson, T. Calarco, R. Folman, M. Andersson, B. Hessmo, and J. Schmiedmayer, Phys. Rev. Lett. **88**, 100401 (2002).

[9] O. Carnal and J. Mlynek, Phys. Rev. Lett. **66**, 2689 (1991).

[10] D. W. Keith, C. R. Ekstrom, Q. A. Turchette, and D. E. Pritchard, Phys. Rev. Lett. **66**, 2693 (1991).

[11] M. Kasevich and S. Chu, Phys. Rev. Lett. **67**, 181 (1991).

[12] B. P. Anderson and M. A. Kasevich, Science **282**, 1686 (1998).

[13] C. Orzel, A. K. Tuchman, M. L. Fenselau, M. Yasuda, and M. A. Kasevich, Science **291**, 2386 (2001).

[14] F. S. Cataliotti, S. Burger, C. Fort, P. Maddaloni, F. Minardi, A. Trombettoni, A. Smerzi, and M. Inguscio, Science **293**, 843 (2001).

[15] M. Greiner, I. Bloch, O. Mandel, T. W. Hänsch, and T. Esslinger, Phys. Rev. Lett. **87**, 160405 (2001).

[16] M. Greiner, O. Mandel, T. Esslinger, T. W. Hänsch, and I. Bloch, Nature **415**, 39 (2002).

[17] O. Mandel, M. Greiner, A. Widera, T. Rom, T. W. Hänsch, and I. Bloch, Phys. Rev. Lett. **91**, 010407 (2003).

[18] A. Peters, K. Y. Chung, B. Young, J. Hensley, and S. Chu, Phil. Trans. R. Soc. Lond. A **355**, 2223 (1997).

[19] A. Lenef, T. D. Hammond, E. T. Smith, M. S. Chapman, R. A. Rubenstein, and D. E. Pritchard, Phys. Rev. Lett. **78**, 760 (1997).

[20] T. L. Gustavson, P. Bouyer, and M. A. Kasevich, Phys. Rev. Lett. **78**, 2046 (1997).

[21] M. S. Chapman, T. D. Hammond, A. Lenef, J. Schmiedmayer, R. A. Rubenstein, E. Smith, and D. E. Pritchard, Phys. Rev. Lett. **75**, 3783 (1995).

[22] C. R. Ekstrom, J. Schmiedmayer, M. S. Chapman, T. D. Hammond, and D. E. Pritchard, Phys. Rev. A **51**, 3883 (1995).

[23] S. Gupta, K. Dieckmann, Z. Hadzibabic, and D. E. Pritchard, Phys. Rev. Lett. **89**, 140401 (2002).

[24] M. R. Andrews, C. G. Townsend, H.-J. Miesner, D. S. Durfee, D. M. Kurn, and W. Ketterle, Science **275**, 637 (1997).

[25] A. Smerzi, S. Fantoni, S. Giovanazzi, and S. R. Shenoy, Phys. Rev. Lett. **79**, 4950 (1997).

[26] J. A. Stickney and A. A. Zozulya, Phys. Rev. A **66**, 053601 (2002).

[27] T. L. Gustavson, A. P. Chikkatur, A. E. Leanhardt, A. Görlitz, S. Gupta, D. E. Pritchard, and W. Ketterle, Phys. Rev. Lett. **88**, 020401 (2002).

[28] A. Röhrl, M. Naraschewski, A. Schenzle, and H. Wallis, Phys. Rev. Lett. **78**, 4143 (1997).

[29] F. Dalfovo, S. Giorgini, L. P. Pitaevskii, and S. Stringari, Rev. Mod. Phys. **71**, 463 (1999).

[30] M. Lewenstein and L. You, Phys. Rev. Lett. **77**, 3489 (1996).

[31] J. Javanainen and M. Wilkens, Phys. Rev. Lett. **78**, 4675 (1997).

[32] C. Menotti, J. R. Anglin, J. I. Cirac, and P. Zoller, Phys. Rev. A **63**, 023601 (2001).

Appendix D

Imprinting Vortices in a Bose-Einstein Condensate using Topological Phases

This appendix contains a reprint of Ref. [123]: A.E. Leanhardt, A. Görlitz, A.P. Chikkatur, D. Kielpinski, Y. Shin, D.E. Pritchard, and W. Ketterle, *Imprinting Vortices in a Bose-Einstein Condensate using Topological Phases*, Phys. Rev. Lett. **89**, 190403 (2002). Axel Görlitz and I worked on this experiment during April and May, 2001 with no success. At that time we attempted to "thread" the magnetic field zero of a three-dimensional (spherical) quadrupole field through an optically confined condensate. The quadrupole field had a $10 - 20$ G/cm gradient and was normally used for the MOT. The optical trap had a disc shape and had just been used to create two-dimensional condensates [67]. We were very concerned about spin-flip transitions as the quadrupole zero passed through the condensate so we pierced the center of the cloud with a blue-detuned laser beam to create a toroidal shaped condensate. Ultimately the experiment sat dormant for nearly a year before it was revitalized late one night in March, 2002. The results of that revitalization are contained in this Letter.

Imprinting Vortices in a Bose-Einstein Condensate using Topological Phases

A. E. Leanhardt, A. Görlitz,* A. P. Chikkatur, D. Kielpinski, Y. Shin, D. E. Pritchard, and W. Ketterle†

Department of Physics, MIT-Harvard Center for Ultracold Atoms, and Research Laboratory of Electronics, Massachusetts Institute of Technology, Cambridge, Massachusetts, 02139

(Received 16 June 2002; published 22 October 2002)

Vortices were imprinted in a Bose-Einstein condensate using topological phases. Sodium condensates held in a Ioffe-Pritchard magnetic trap were transformed from a nonrotating state to one with quantized circulation by adiabatically inverting the magnetic bias field along the trap axis. Using surface wave spectroscopy, the axial angular momentum per particle of the vortex states was found to be consistent with $2\hbar$ or $4\hbar$, depending on the hyperfine state of the condensate.

DOI: 10.1103/PhysRevLett.89.190403 PACS numbers: 03.75.Fi, 03.65.Vf, 67.40.Db, 67.40.Vs

As superfluids, Bose-Einstein condensates support rotational flow only through quantized vortices. The atomic velocity field is proportional to the gradient of the phase associated with the macroscopic wave function. This phase winds through an integer multiple of 2π radians around a vortex line. Such a phase winding can be imprinted onto the condensate wave function either dynamically or topologically. Dynamically, the phase of the condensate evolves according to the time integral of its energy, which can be tailored locally with a spatially varying external potential. Topologically, the phase of the condensate advances through adiabatic variations in the parameters of the Hamiltonian governing the system. This phase, which is solely a function of the path traversed by the system in the parameter space of the Hamiltonian, is known as Berry's phase [1].

In this Letter, we implement the proposal of Refs. [2–5] and demonstrate the use of topological phases to imprint vortices in a gaseous Bose-Einstein condensate. Previously, vortices have been generated in two-component condensates using a dynamical phase-imprinting technique [6] and in single-component condensates by rotating the cloud with an anisotropic potential [7–10], by slicing through the cloud with a perturbation above the critical velocity of the condensate [8,11], and through the decay of solitons [12,13]. In this work, ^{23}Na condensates were prepared in either the lower, $|F, m_F\rangle = |1, -1\rangle$, or upper, $|2, +2\rangle$, hyperfine state and confined in a Ioffe-Pritchard magnetic trap. Vortices were created by adiabatically inverting the magnetic bias field along the trap axis and could be removed by returning the bias field to its original direction. Using surface wave spectroscopy [14–16], we measured the axial angular momentum per particle of the $|1, -1\rangle$ and $|2, +2\rangle$ vortex states to be consistent with $-2m_F\hbar$ as predicted [2–5].

A Ioffe-Pritchard magnetic trap consists of an axial bias field (with curvature) and a two-dimensional quadrupole field in the orthogonal plane [17,18]:

$$\vec{B}(x, y, z) = B_z\hat{z} + B'(x\hat{x} - y\hat{y}), \quad (1)$$

where B' is the radial magnetic field gradient and quadratic terms have been neglected. For a condensate of radial extent R, inverting B_z from $B_z \gg B'R > 0$ to $B_z \ll -B'R < 0$ rotates the atomic angular momentum, $\vec{F}$, by π radians. While all atomic angular momenta rotate through the same angle, a relative phase is established across the condensate because the angular momenta rotate about a unit vector $\hat{n}(\phi) = \sin\phi\hat{x} + \cos\phi\hat{y}$ that depends on the azimuthal angle, ϕ, describing the atomic position [Fig. 1(a)].

As B_z is inverted, $\vec{F}$ adiabatically follows $\vec{B}(x, y, z)$, and the condensate remains in the state $|F, m_F\rangle$ with respect to the local magnetic field. However, in a basis

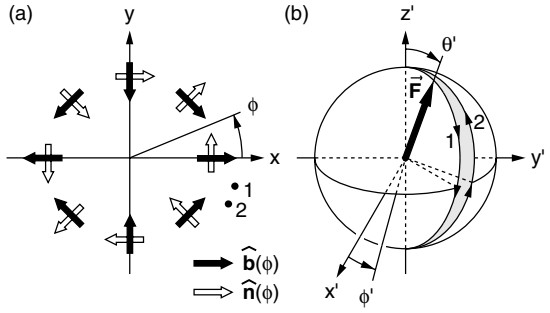

FIG. 1. Geometry of the rotating magnetic field for imprinting topological phases. (a) The unit vectors $\hat{b}(\phi)$ point in the direction of the two-dimensional quadrupole field providing the radial confinement of a Ioffe-Pritchard magnetic trap. The atomic angular momenta rotate about the unit vectors $\hat{n}(\phi)$ as the axial bias field, B_z, is ramped from positive to negative values. (b) For an atom in state $|F, m_F\rangle$, its atomic angular momentum, $\vec{F}$, traverses a path on a sphere of radius $|m_F|\hbar$ as it adiabatically follows its local magnetic field. The primed coordinate system is centered on the atomic position and has axes parallel to those of the unprimed coordinate system in (a). For an atomic position described by the azimuthal angle ϕ, $\vec{F}$ rotates in a half-plane defined by $\phi' = -\phi$ for $m_F > 0$ and $\phi' = -\phi + \pi$ for $m_F < 0$ as B_z is inverted. After inverting B_z, the relative topological phase acquired between atoms located at positions 1 and 2 in (a) is proportional to the solid angle subtended by the shaded surface, bounded by the contour marked with arrowheads (see text).

fixed in the lab frame, the condensate makes the transition $|F, m_z = +m_F\rangle \rightarrow |F, m_z = -m_F\rangle$, where m_F and m_z are the projection of $\vec{F}$ along the local magnetic field direction and z axis, respectively. Applying the quantum mechanical rotation operator gives the condensate wave function in the lab frame after inverting B_z as

$$|\psi\rangle = e^{-i(\vec{\mathcal{F}}/\hbar)\cdot\hat{n}(\phi)\pi}\sqrt{\rho(\vec{r})}|F, m_z = +m_F\rangle, \quad (2)$$

$$= (-1)^{F+m_F}\sqrt{\rho(\vec{r})}e^{-i2m_F\phi}|F, m_z = -m_F\rangle, \quad (3)$$

where $\vec{\mathcal{F}}$ is the angular momentum operator such that $\vec{F} = \langle\vec{\mathcal{F}}\rangle$ and $\rho(\vec{r})$ is the number density of condensed atoms. The topological phase factor $e^{-i2m_F\phi}$ describes a vortex of winding number $2|m_F|$ with the sense of rotation dependent on the sign of m_F.

This result can be interpreted in terms of Berry's phase [4]. Figure 1(b) shows the orientation of $\vec{F}$ in the lab frame for $m_F > 0$. Atoms located at position $k = 1, 2$ in Fig. 1(a) have azimuthal angle ϕ_k and angular momentum $\vec{F}_k$. As B_z is inverted, $\vec{F}_k$ traces path k from top to bottom on the sphere in Fig. 1(b). The topological phase acquired by an atom in this process is solely a function of the path traversed by its angular momentum vector. Since this path depends on the azimuthal angle describing the atomic position, a relative phase is established between spatially separated atoms. The condensate wave function after inverting B_z is given by

$$|\psi\rangle = \sqrt{\rho(\vec{r})}e^{i\gamma(\phi)}|F, m_F\rangle, \quad (4)$$

where $\gamma(\phi)$ is the topological phase acquired by atoms with azimuthal angle ϕ.

For an atom in state $|F, m_F\rangle$, Berry's phase, $\gamma(C)$, acquired as its angular momentum vector traverses a closed contour, C, on the surface of the sphere in Fig. 1(b) is given by [1]

$$\gamma(C) = -m_F\Omega(C), \quad (5)$$

where $\Omega(C)$ is the solid angle subtended by a surface bounded by the contour C. Calculating the relative phase, $\gamma(\phi_1) - \gamma(\phi_2)$, with the aid of Eq. (5) requires closing the contours traced by each $\vec{F}_k$ along an identical path. For clarity, we choose to close each contour along path 2 itself, and hence $\gamma(\phi_1) - \gamma(\phi_2) = \gamma(C)$, where C is the contour formed by path 1 traversed from top to bottom and path 2 traversed from bottom to top, as indicated with arrowheads in Fig. 1(b).

A surface bounded by this contour subtends a solid angle $\Omega(C) = 2(\phi_1 - \phi_2)$, yielding a relative phase $\gamma(\phi_1) - \gamma(\phi_2) = -2m_F(\phi_1 - \phi_2)$. Thus, we set

$$\gamma(\phi) = -2m_F\phi, \quad (6)$$

up to an additive term independent of position. This yields a reinterpretation of Eq. (3) in terms of Berry's phase.

In this work, Bose-Einstein condensates containing over 10^7 ^{23}Na atoms were created in the $|1, -1\rangle$ state in a magnetic trap, captured in the focus of an optical tweezers laser beam, and transferred into an auxiliary "science" chamber as described in Ref. [19]. While optically confined by the tweezers, $|2, +2\rangle$ condensates were generated by sweeping through the $|1, -1\rangle \leftrightarrow |1, 0\rangle \leftrightarrow |1, +1\rangle$ radio-frequency transition with 100% efficiency, then sweeping through the $|1, +1\rangle \leftrightarrow |2, +2\rangle$ microwave transition with 80% efficiency [20]. In the science chamber, the condensate was loaded into a microfabricated Ioffe-Pritchard magnetic trap formed by a Z-shaped wire carrying current I and an external magnetic bias field, $B_\perp$, as detailed in Ref. [21]. Condensates were detected via axial absorption imaging whereby resonant laser light propagating along the z axis illuminated the atoms and was imaged onto a CCD camera.

Typical wire-trap parameters were $I = 1200$ mA, $B_\perp = 5.4$ G, and $B_z \approx 1$ G, resulting in a radial magnetic field gradient of $B' = 120$ G/cm. For $|1, -1\rangle$ ($|2, +2\rangle$) condensates, the axial and radial trap frequencies were $\omega_z = 2\pi \times 6.0$ Hz ($\omega_z = 2\pi \times 8.5$ Hz) and $\omega_\perp = 2\pi \times 210$ Hz ($\omega_\perp = 2\pi \times 300$ Hz), respectively. After transfer into the wire trap, condensates in the $|1, -1\rangle$ ($|2, +2\rangle$) state contained over 2×10^6 atoms (1×10^6 atoms) and had a lifetime in excess of 10 s (3 s) with an applied radio-frequency shield. This represents the first magnetic trapping of ^{23}Na condensates in the upper hyperfine level, with previous work done exclusively in optical dipole traps [20].

Along the wire-trap axis, the magnetic field is

$$\vec{B}(x = 0, y = 0, z) = (B_z + \tfrac{1}{2}B''z^2)\hat{z}, \quad (7)$$

where quadratic terms neglected in Eq. (1) have been included. The axial magnetic field curvature, B'', which arises from the geometry of the Z wire, was held constant throughout the experiment. By reversing an external axial magnetic field, we inverted B_z. Changing the sign of B_z, but not B'', resulted in a magnetic field saddle point at the center of the cloud and axial antitrapping of weak-field seeking atoms. This limited the condensate lifetime after inverting B_z to $\lesssim 50$ ms.

Vortices created by inverting B_z were observed after ballistic expansion and were identified by central density depletions due to the angular momentum barrier associated with a rotating cloud (Fig. 2). These vortices could be removed by returning B_z to its original direction.

For $|1, -1\rangle$ condensates, the best results were achieved by inverting the axial bias field linearly from $B_z = 860$ mG to -630 mG in 11 ms. For $|2, +2\rangle$ condensates, the optimum ramp time over the same range was 4 ms. The field inversion process caused an atom loss of $\approx 50\%$ due to nonadiabatic spin flips as B_z passed through zero [4,5]. The density depletions shown in Figs. 2(b), 2(c), and 2(g) were observed after inverting the axial bias field and holding the trapped condensate for longer than a radial trap period. Thus, the atom loss from the center of the cloud during the field inversion process could not be

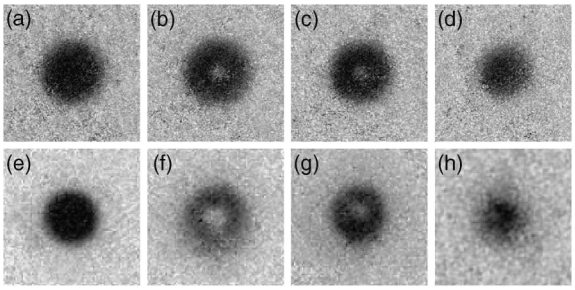

FIG. 2. Observation of vortices formed by imprinting topological phases. Axial absorption images of condensates in the $|1, -1\rangle$ state after 18 ms of ballistic expansion (a) prior to inverting B_z, after inverting B_z, and holding the trapped condensate for (b) 5 ms and (c) 20 ms, and (d) after inverting B_z and then returning it to its original direction. Axial absorption images of condensates in the $|2, +2\rangle$ state after 7 ms of ballistic expansion (e) prior to inverting B_z, after inverting B_z, and holding the trapped condensate for (f) 0 ms and (g) 5 ms, and (h) after inverting B_z and then returning it to its original direction. The field of view is (a)–(d) 570 μm $\times$ 570 μm and (e)–(h) 285 μm $\times$ 285 μm.

responsible for the observed density depletions. Typical $|1, -1\rangle$ ($|2, +2\rangle$) condensates after inverting the axial bias field contained up to 1×10^6 atoms (0.5×10^6 atoms) with a Thomas-Fermi radius $R_{\mathrm{TF}} = 5.4 \pm 0.2$ μm ($R_{\mathrm{TF}} = 4.5 \pm 0.2$ μm) in a trap with radial frequency $\omega_\perp = 2\pi \times 250$ Hz ($\omega_\perp = 2\pi \times 350$ Hz).

The axial angular momentum per particle of the vortex states was measured using surface wave spectroscopy [14–16]. A superposition of counterrotating ($m_\ell = \pm 2$) quadrupolar ($\ell = 2$) surface waves was excited in the condensate by radially displacing the magnetic trap center for 200 μs. Here ℓ and m_ℓ characterize the angular momentum and its projection along the z axis of the quadrupole modes, respectively. This created an elliptical condensate cross section with time-dependent eccentricity. In the absence of a vortex, the $m_\ell = \pm 2$ quadrupole modes are degenerate and the axes of the elliptical condensate cross section remain fixed in time. This degeneracy is lifted by the presence of a vortex, causing the axes to precess in the direction of the fluid flow. The precession rate, $\dot{\Theta}$, is given by [14–16]

$$\dot{\Theta} = \frac{\langle L_z \rangle}{2M\langle r_\perp^2 \rangle}, \tag{8}$$

where $\langle L_z \rangle$ is the axial angular momentum per particle characterizing the vortex state, M is the atomic mass, and $\langle r_\perp^2 \rangle = \langle x^2 + y^2 \rangle$ is the mean-squared trapped condensate radius with vortices present.

By measuring the precession rate of the quadrupole axes and the mean-squared radius of the condensate in the trap, the axial angular momentum per particle was determined. After exciting the quadrupolar modes, the condensate evolved in the trap for variable times in the range 0.2–7.4 ms. The condensate was then released from the trap and imaged with resonant light after ballistic expansion as shown in Figs. 3(a)–3(l). The resulting images were fit to an elliptical Thomas-Fermi profile to determine the orientation of the quadrupole axes. The orientation angle is plotted as a function of time in Fig. 3(m). To determine the mean-squared trapped condensate radius, vortices were imprinted in the condensate but quadrupolar modes were not excited. Images of ballistically expanded condensates similar to those in Figs. 2(b), 2(c), 2(f), and 2(g) were fit to a Thomas-Fermi profile with a circular cross section. The fitting routine ignored the central region of the cloud where the density was depleted due to the vortex core. The mean-squared trapped condensate radius was derived through the relation

$$\langle r_\perp^2 \rangle = \frac{2}{7} \frac{R_\perp^2}{1 + \omega_\perp^2 \tau^2}, \tag{9}$$

where $R_\perp$ is the Thomas-Fermi radius of the condensate after ballistically expanding for a time τ from a trap with radial frequency $\omega_\perp$. The factor $1 + \omega_\perp^2 \tau^2$ accounts for the change in Thomas-Fermi radius during the expansion process [22], and the factor $2/7$ results from averaging over the inhomogeneous condensate density distribution assuming no vortices are present. For low angular momentum vortex states, the density depletion at the vortex core does not significantly modify the density distribution of the condensate, and we expect the $2/7$ factor to still be accurate [23].

For $|1, -1\rangle$ condensates, the quadrupole oscillation was excited after a delay of 0, 5, and 20 ms from the completion of the inversion of the axial bias field. The measured axial angular momenta per particle were $(+1.9 \pm 0.3)\hbar$, $(+2.1 \pm 0.3)\hbar$, and $(+1.9 \pm 0.2)\hbar$, respectively. The uncertainty in the measurement arises from the linear fit to the precession angle and the determination of $\langle r_\perp^2 \rangle$. For $|2, +2\rangle$ condensates, the quadrupole oscillation was excited immediately upon the completion of the inversion of the axial bias field. The measured axial angular momentum per particle was $(-4.4 \pm 0.4)\hbar$. For both internal states, the measurements are consistent with the predicted axial angular momentum per particle of $-2m_F\hbar$ [2–5].

Multiply charged vortices are unstable against decay into singly charged vortices [24]. From our experiments, we cannot determine if the condensate contained one multiply charged vortex or multiple, singly charged vortices. If multiple vortices were present, they must be closely spaced since they were not resolved after ballistic expansion. Furthermore, if the singly charged vortices had moved apart considerably, it would have lowered the extracted value of $\langle L_z \rangle$ [15], which was not observed even with delayed probing.

In conclusion, we have used topological phases to imprint vortices in a Bose-Einstein condensate. Higher angular momentum states can be generated by using higher-order, axisymmetric multipole magnetic fields. In general, this phase-imprinting technique opens the

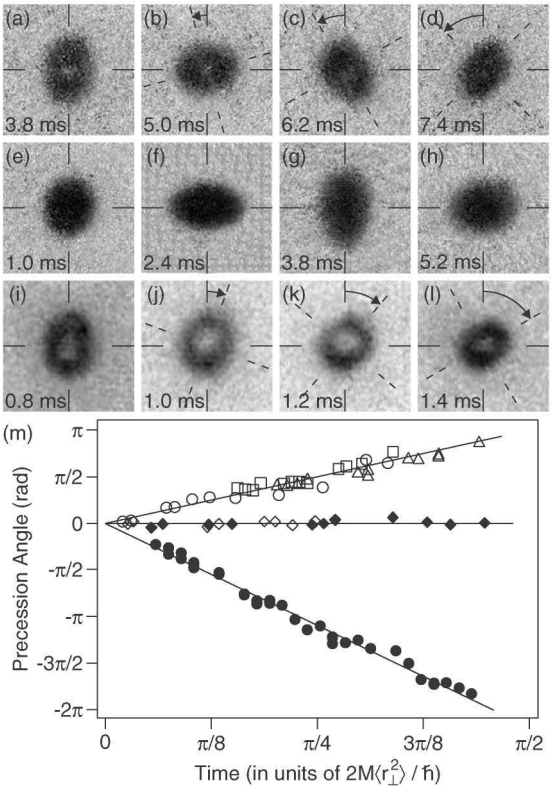

FIG. 3. Surface wave spectroscopy. Axial absorption images after 18 ms of ballistic expansion of $|1, -1\rangle$ condensates undergoing a quadrupole oscillation (a)–(d) in the presence of a vortex and (e)–(h) in the absence of a vortex. Successive images were taken during successive half periods of the quadrupole oscillation such that the short and long axes of the elliptical cross section were exchanged. Images (a)–(d) show counterclockwise (positive) precession of the quadrupole axes, while images (e)–(h) show no precession. (i)–(l) Axial absorption images after 7 ms of ballistic expansion of $|2, +2\rangle$ condensates undergoing a quadrupole oscillation in the presence of a vortex. The images were taken during a single half period of the quadrupole oscillation. Images (i)–(l) show clockwise (negative) precession of the quadrupole axes. The field of view is (a)–(h) $570\ \mu\text{m} \times 570\ \mu\text{m}$ and (i)–(l) $285\ \mu\text{m} \times 285\ \mu\text{m}$. (m) Precession angle vs time in the presence of a vortex for $|1, -1\rangle$ condensates measured after a delay of 0 ms (open circles), 5 ms (open squares), and 20 ms (open triangles) from the completion of the inversion of the axial bias field, in the absence of a vortex for $|1, -1\rangle$ (open diamonds) and $|2, +2\rangle$ (filled diamonds) condensates, and in the presence of a vortex for $|2, +2\rangle$ condensates measured immediately upon the completion of the inversion of the axial bias field (filled circles).

potential for studying the stability of multiply charged vortices and the dynamics of vortex-vortex interactions at short separations.

We thank J. R. Abo-Shaeer for a critical reading of the manuscript. This work was funded by ONR, NSF, ARO, NASA, and the David and Lucile Packard Foundation. A. E. L. acknowledges additional support from NSF.

*5th Physikalisches Institut, University of Stuttgart, 70550 Stuttgart, Germany.
†Electronic address: http://cua.mit.edu/ketterle_group/

[1] M. V. Berry, Proc. R. Soc. London A **392**, 45 (1984).
[2] M. Nakahara, T. Isoshima, K. Machida, S.-i. Ogawa, and T. Ohmi, Physica (Amsterdam) **284-288B**, 17 (2000).
[3] T. Isoshima, M. Nakahara, T. Ohmi, and K. Machida, Phys. Rev. A **61**, 063610 (2000).
[4] S.-I. Ogawa, M. Möttönen, M. Nakahara, T. Ohmi, and H. Shimada, Phys. Rev. A **66**, 013617 (2002).
[5] M. Möttönen, N. Matsumoto, M. Nakahara, and T. Ohmi, cond-mat/0205542.
[6] M. R. Matthews, B. P. Anderson, P. C. Haljan, D. S. Hall, C. E. Wieman, and E. A. Cornell, Phys. Rev. Lett. **83**, 2498 (1999).
[7] K. W. Madison, F. Chevy, W. Wohlleben, and J. Dalibard, Phys. Rev. Lett. **84**, 806 (2000).
[8] J. R. Abo-Shaeer, C. Raman, J. M. Vogels, and W. Ketterle, Science **292**, 476 (2001).
[9] P. C. Haljan, I. Coddington, P. Engels, and E. A. Cornell, Phys. Rev. Lett. **87**, 210403 (2001).
[10] E. Hodby, G. Hechenblaikner, S. A. Hopkins, O. M. Maragò, and C. J. Foot, Phys. Rev. Lett. **88**, 010405 (2002).
[11] S. Inouye, S. Gupta, T. Rosenband, A. P. Chikkatur, A. Görlitz, T. L. Gustavson, A. E. Leanhardt, D. E. Pritchard, and W. Ketterle, Phys. Rev. Lett. **87**, 080402 (2001).
[12] Z. Dutton, M. Budde, C. Slowe, and L. V. Hau, Science **293**, 663 (2001).
[13] B. P. Anderson, P. C. Haljan, C. A. Regal, D. L. Feder, L. A. Collins, C. W. Clark, and E. A. Cornell, Phys. Rev. Lett. **86**, 2926 (2001).
[14] F. Zambelli and S. Stringari, Phys. Rev. Lett. **81**, 1754 (1998).
[15] F. Chevy, K. W. Madison, and J. Dalibard, Phys. Rev. Lett. **85**, 2223 (2000).
[16] P. C. Haljan, B. P. Anderson, I. Coddington, and E. A. Cornell, Phys. Rev. Lett. **86**, 2922 (2001).
[17] Y. V. Gott, M. S. Ioffe, and V. G. Tel'kovskii, Nucl. Fusion Suppl. **3**, 1045 (1962).
[18] D. E. Pritchard, Phys. Rev. Lett. **51**, 1336 (1983).
[19] T. L. Gustavson, A. P. Chikkatur, A. E. Leanhardt, A. Görlitz, S. Gupta, D. E. Pritchard, and W. Ketterle, Phys. Rev. Lett. **88**, 020401 (2002).
[20] A. Görlitz, T. L. Gustavson, A. E. Leanhardt, R. Löw, A. P. Chikkatur, S. Gupta, S. Inouye, D. E. Pritchard, and W. Ketterle, cond-mat/0208385.
[21] A. E. Leanhardt, A. P. Chikkatur, D. Kielpinski, Y. Shin, T. L. Gustavson, W. Ketterle, and D. E. Pritchard, Phys. Rev. Lett. **89**, 040401 (2002).
[22] Y. Castin and R. Dum, Phys. Rev. Lett. **77**, 5315 (1996).
[23] F. Dalfovo, S. Giorgini, L. P. Pitaevskii, and S. Stringari, Rev. Mod. Phys. **71**, 463 (1999).
[24] P. Nozières and D. Pines, *The Theory of Quantum Liquids* (Addison-Wesley Publishing Co., Reading, MA, 1990), Vol. II.

Appendix E

Coreless Vortex Formation in a Spinor Bose-Einstein Condensate

This appendix contains a reprint of Ref. [126]: A.E. Leanhardt, Y. Shin, D. Kielpinski, D.E. Pritchard, and W. Ketterle, *Coreless Vortex Formation in a Spinor Bose-Einstein Condensate*, Phys. Rev. Lett. **90**, 140403 (2003). I am grateful to K. Machida for bringing the spin textured examined in this Letter to my attention and for his hospitality during my subsequent visit to Okayama.

Coreless Vortex Formation in a Spinor Bose-Einstein Condensate

A. E. Leanhardt, Y. Shin, D. Kielpinski, D. E. Pritchard, and W. Ketterle*

Department of Physics, MIT-Harvard Center for Ultracold Atoms, and Research Laboratory of Electronics, Massachusetts Institute of Technology, Cambridge, Massachusetts 02139

(Received 20 December 2002; published 9 April 2003)

Coreless vortices were phase imprinted in a spinor Bose-Einstein condensate. The three-component order parameter of $F = 1$ sodium condensates held in a Ioffe-Pritchard magnetic trap was manipulated by adiabatically reducing the magnetic bias field along the trap axis to zero. This distributed the condensate population across its three spin states and created a spin texture. Each spin state acquired a different phase winding which caused the spin components to separate radially.

DOI: 10.1103/PhysRevLett.90.140403 PACS numbers: 03.75.Lm, 03.65.Vf, 03.75.Mn, 67.57.Fg

Spin textures play a central role in describing the physics of elementary particles [1], liquid ^{3}He-A [2–4], the quantum Hall effect [5], and gaseous Bose-Einstein condensates [6–10]. Topological defects vary between superfluid systems described by scalar and vector order parameters. In spinless or spin-polarized condensates, line defects such as vortices have cores where the density of condensed particles is necessarily zero to keep the order parameter single valued [11–13]. However, in condensates with an internal, spin degree of freedom, coreless vortices exist as spin textures [4,14]. Such structures are referred to as skyrmions (Anderson-Toulouse vortices [3]) or merons (half-skyrmions, Mermin-Ho vortices [2]) depending on the boundary conditions of the system.

In this Letter, we study spin textures in a Bose-Einstein condensate. Coreless vortices were created in $F = 1$ spinor condensates held in a Ioffe-Pritchard magnetic trap by adiabatically reducing the magnetic bias field along the trap axis to zero. This continuously transformed the initially spin-polarized condensate into a coherent superposition of three spin states, each with a different phase winding. The resulting angular momentum per particle varied between spin states and the condensate evolved such that states with more angular momentum per particle circulated around states with less angular momentum per particle. Thus, the condensate had a net axial magnetization that varied with radial position. Previous work on vortices in a two-component system used laser, microwave, and radio frequency fields to spatially and temporally control the interconversion between components [14]. However, without these applied fields the two components evolved independently as distinguishable fluids. In our work, the spin states can freely interconvert at all points in space and time such that the spin texture would continually heal itself even in the presence of state-dependent losses.

In cylindrical coordinates, the spin-F condensate wave function can be written as $|\Psi(r, \phi, z)\rangle = \sqrt{n(r, \phi, z)}|\zeta(r, \phi, z)\rangle$, where n is the atomic number density and the $2F + 1$ component spinor $|\zeta\rangle = \sum_{m_z=-F}^{F} \zeta_{m_z}|F, m_z\rangle$, $|\langle\zeta|\zeta\rangle|^2 = 1$ describes a spin texture. A Ioffe-Pritchard magnetic trap consists of an axial bias field (with curvature) and a two-dimensional quadrupole field in the orthogonal plane [15,16]:

$$\vec{B}(r, \phi, z) = B_z\hat{z} + B'r(\cos(2\phi)\hat{r} - \sin(2\phi)\hat{\phi}), \quad (1)$$

where B' is the radial magnetic field gradient and quadratic terms have been neglected. For a condensate of radial extent R confined in a Ioffe-Pritchard magnetic trap with $B_z \gg B'R > 0$, $|\zeta\rangle = |F, m_z = m_F\rangle$, where m_z and m_F are the projection of the atomic spin along the z axis and local magnetic field direction, respectively. Adiabatically ramping B_z from $B_z \gg B'R > 0$ to zero rotates the atomic spin about the position-dependent axis $\hat{n}(\phi) = \sin\phi\hat{x} + \cos\phi\hat{y}$, and drives the transition $|F, m_z = m_F\rangle \rightarrow \sum_{m_z=-|m_F|}^{|m_F|} \zeta_{m_z} \exp[i(m_z - m_F)\phi]|F, m_z\rangle$ [17,18]. Thus, the condensate population is distributed across $2|m_F| + 1$ spin states with each acquiring a different topological phase factor and angular momentum per particle due to the variation of Berry's phase with magnetic quantum number [19].

The condensate remains in the state $|F, m_F\rangle$ with respect to the local magnetic field provided the local Zeeman energy, $\sim g_F\mu_B[B_z^2 + (B'r)^2]^{1/2}$, dominates the local kinetic energy associated with the spin texture, $\sim\hbar^2/mr^2$, where g_F is the Landé g factor, μ_B is the Bohr magneton, and m is the atomic mass. For $B_z = 0$, atomic spins aligned with the quadrupole magnetic field produce the planar spin texture in Fig. 1(a). However, the infinite kinetic energy associated with the wave function singularity at $r = 0$ creates a nonplanar spin texture over a disk of radius $\sim(\hbar^2/mg_F\mu_B B')^{1/3}$, with higher angular momentum spin states residing outside those with lower angular momentum.

Bose-Einstein condensates containing over 10^7 ^{23}Na atoms were created in the $|1, -1\rangle$ state in a magnetic trap, captured in the focus of an optical tweezers laser beam, and transferred into an auxiliary "science" chamber as described in Ref. [21]. In the science chamber, the condensate was loaded into a microfabricated Ioffe-Pritchard magnetic trap formed by a Z-shaped

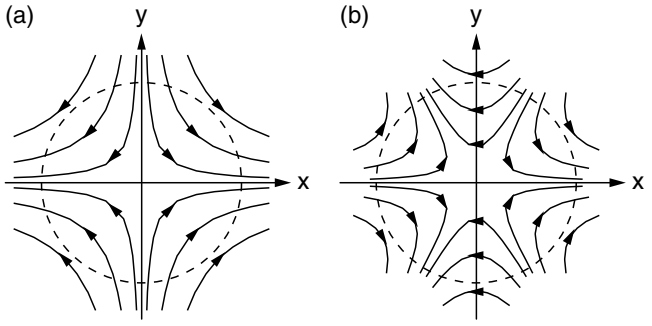

FIG. 1. Planar spin textures. Spins aligned with two-dimensional (a) quadrupole and (b) hexapole magnetic fields produce textures with winding numbers -1 and -2, respectively. Counterclockwise traversal of the dashed contours in (a) and (b) leads to clockwise (negative) spin rotation, with the winding number defined as the integer number of revolutions made by the spin vector while circumnavigating the singularity at the origin [20].

50 μm $\times$ 10 μm electroplated copper wire carrying current I and an external magnetic bias field, $B_\perp$, as described in Ref. [22]. Typical wiretrap parameters were $I = 720$ mA, $B_\perp = 5.3$ G, and $B_z = 1.3$ G, resulting in a radial magnetic field gradient $B' = 180$ G/cm. This produced axial and radial trap frequencies $\omega_z = 2\pi \times 4$ Hz and $\omega_\perp = 2\pi \times 250$ Hz, respectively. Condensates in the wiretrap had $\geq 2 \times 10^6$ atoms, a Thomas-Fermi radius of ≈ 5 μm, and a lifetime ≥ 25 s.

Coreless vortices imprinted onto the condensate wave function by adiabatically ramping $B_z \rightarrow 0$ are shown in Fig. 2. To observe the nature of the spin texture, an axial bias field was switched on nonadiabatically along either the negative [Figs. 2(b)–2(d)] or positive [Figs. 2(e)–2(h)] z axis. Switching the axial bias field on suddenly "froze" the atomic spins and effectively "projected" the condensate wave function onto a basis quantized with respect to the local (axial) magnetic field. This allowed the spin states to be separated by a magnetic field gradient applied during ballistic expansion. Switching the direction of the axial projection field exchanged the roles of the $|1, -1\rangle$ and $|1, +1\rangle$ states. Figures 2(a) and 2(e) show the coreless nature of the vortices, while Figs. 2(b) and 2(f) show the concentric cylinder structure resulting from the competition between the atomic Zeeman energy and the kinetic energy of the rotating spin states. We assume that the two-dimensional ($\omega_z \ll \omega_\perp$) ballistic expansion process simply magnifies the condensate wave function, as it does in the expansion of a single-component condensate with vortices [23,24].

Along the wiretrap axis, the magnetic field was

$$\vec{B}(r = 0, \phi, z) = (B_z + \tfrac{1}{2}B''z^2)\hat{z}, \tag{2}$$

where quadratic terms neglected in Eq. (1) are included. Nonzero axial magnetic field curvature, $B'' \approx 5$ G/cm^2, implies that the spin texture had a slight axial dependence. The axial bias field was ramped linearly from $B_z = 1.3$ G to $B_z \approx 0$ in 10 ms to imprint the coreless vortices. This compressed the condensate radially and increased the condensate chemical potential from $\mu \approx (\mu_B/2) \times 3$ mG to $\mu \approx (\mu_B/2) \times 27$ mG. Ramping $B_z \rightarrow 0$ fast compared to the axial trap period (250 ms), but slow compared to the initial radial trap period (4 ms), guaranteed that the axial magnetic field variation remained constant throughout the experiment at $\Delta B_z \approx 3$ mG, while at $B_z \approx 0$ the radial magnetic field variation was $\Delta B_r \approx 27$ mG. The images shown in Fig. 2 integrated the atomic number density along the z axis and therefore averaged over the minor ($\Delta B_z \ll \Delta B_r$) axial variation to the spin texture.

To project the condensate wave function onto a basis quantized with respect to the local magnetic field, an ≈ 10 G axial bias field was switched on at a rate of $\dot{B}_z = 2 \times 10^5$ G/s along either the negative or the positive z axis. 100 μs later the magnetic trap was switched off allowing the atoms to expand ballistically. For $0 \leq B_r \leq \Delta B_r$, the Landau-Zener nonadiabatic transition probability, $\exp(-\pi\mu_B B_r^2/\hbar\dot{B}_z) \geq 0.9$, was sufficiently close to unity that the atomic spins remained "frozen" during the sudden application of the axial bias field and the spin texture could be accurately diagnosed. While the total condensate density monotonically decreased as a function of radial position [Figs. 2(a) and 2(e)], the density of each spin component peaked at a different radius signifying a variation in the angular momentum per particle between spin states [Figs. 2(b) and 2(f)].

Applying the projection field along the positive z axis generated additional rings of atoms in the $|1, -1\rangle$ and $|1, 0\rangle$ states [Fig. 2(f)]. Ramping $B_z \rightarrow 0$ in 10 ms caused nonadiabatic spin flips for atoms near $r = 0$ resulting in an atom loss of $\approx 50\%$ [18]. If these atoms had not left the condensate before the projection field was applied, they may have contributed to the images displayed in Fig. 2(f). The additional rings of atoms may also correspond to a low energy, radial spin-wave excitation [6,7]. However, we could not identify any asymmetry between applying the projection field along the positive versus negative z axis that would account for the presence of the extra rings in Fig. 2(f), but not in Fig. 2(b).

Engineering topological states in a Bose-Einstein condensate has received much theoretical attention [17,25–30]. The evolution of a condensate confined in a Ioffe-Pritchard magnetic trap while ramping $B_z \rightarrow 0$ is described by a position-dependent spin rotation about the $\hat{n}(\phi)$ axis through an angle $\beta(r)$ [18]

$$|\zeta(r, \phi, z)\rangle = e^{-i(\vec{\mathcal{F}}/\hbar)\cdot\hat{n}(\phi)\beta(r)}|\zeta_0\rangle, \tag{3}$$

where $\vec{\mathcal{F}}$ is the spin operator and $|\zeta_0\rangle = |F, m_z = m_F\rangle$ is a polarized spinor. For $|\zeta_0\rangle = |1, -1\rangle$, Eq. (3) gives the condensate spinor in the laboratory frame as

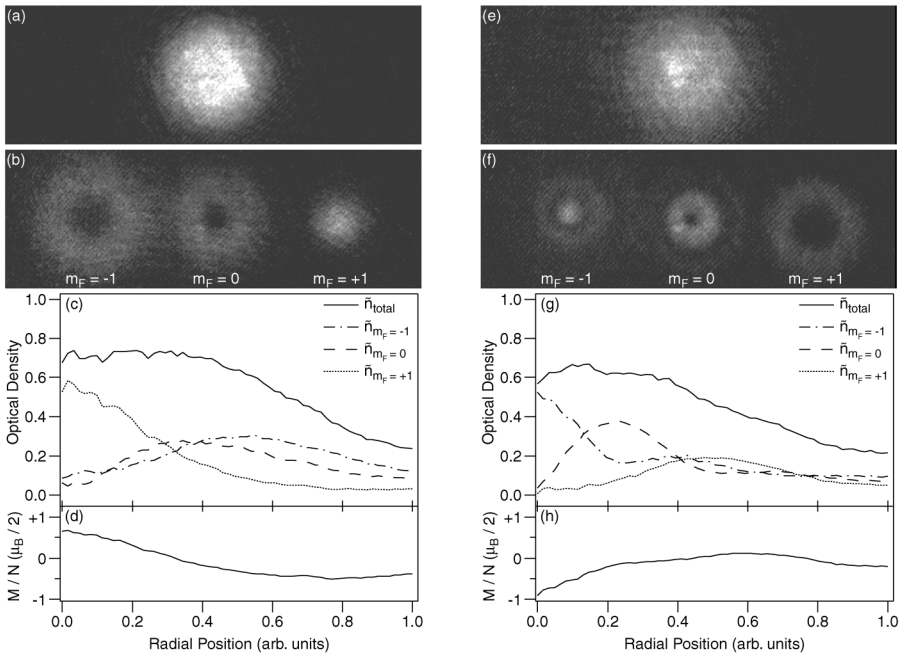

FIG. 2. Coreless vortex formation in a spinor Bose-Einstein condensate. Coreless vortices were imprinted by ramping $B_z \rightarrow 0$ and diagnosed by suddenly switching (a)–(d) $B_z \ll 0$ and (e)–(h) $B_z \gg 0$. Axial absorption images display the optical density of condensates after 20 ms of ballistic expansion (a),(e) without and (b),(f) with a magnetic field gradient applied to separate the different spin states. (c),(g) Azimuthally averaged optical density vs radial position for spin components shown in (b) and (f), respectively. The radial separation of the spin states resulted from their relative phase windings and is a clear signature of the skyrmion/meron wave function [Eq. (4)]. (d),(h) Axial magnetization per particle, $M/N = (\mu_B/2) \times (\tilde{n}_{m_F=+1} - \tilde{n}_{m_F=-1})/\tilde{n}_{\text{total}}$, vs radial position. The absorption imaging light was resonant with the $F = 2 \rightarrow F' = 3$ transition. The atoms were optically pumped into the $F = 2$ hyperfine level with a pulse resonant with the $F = 1 \rightarrow F' = 2$ transition. This provided equal imaging sensitivity to each spin state. The field of view in (a), (b), (e), and (f) is 1.0 mm $\times$ 3.0 mm.

$$|\zeta(r, \phi, z)\rangle = \cos^2[\beta(r)/2]|1, -1\rangle + \frac{-1}{\sqrt{2}}\sin[\beta(r)]e^{i\phi}|1, 0\rangle + \sin^2[\beta(r)/2]e^{i2\phi}|1, +1\rangle. \quad (4)$$

$\beta(0) = 0$ and skyrmions (merons) are described by the boundary condition $\beta(\infty) = \pi$ [$\beta(\infty) = \pi/2$].

The radial dependence of $\beta(r)$ is determined by requiring the Gross-Pitaevskii energy functional,

$$E = \int d^3\vec{r}\, n\left(\frac{\hbar^2}{2m}\langle\nabla\zeta|\nabla\zeta\rangle + V + \left(\frac{c_0}{2} + \frac{c_2}{2}\frac{|\vec{F}|^2}{\hbar^2}\right)n\right), \quad (5)$$

be stationary with respect to variations in β. Equation (5) uses the Thomas-Fermi approximation, and $\langle\nabla\zeta|\nabla\zeta\rangle = \sum_{m_z=-F}^{F}\nabla\zeta_{m_z}^{\dagger}\cdot\nabla\zeta_{m_z}$, $V = -g_F\mu_B\vec{F}\cdot\vec{B}/\hbar$, $\vec{F} = \langle\zeta|\vec{\mathcal{F}}|\zeta\rangle$, $c_0 = 4\pi\hbar^2\bar{a}/m$, and $c_2 = 4\pi\hbar^2\Delta a/m$. Here $\bar{a} = (2a_0 + a_2)/3$ and $\Delta a = (a_2 - a_0)/3$ characterize two-body interactions, where a_0 and a_2 are scattering lengths for collisions with total angular momentum $F = 0$ and $F = 2$, respectively [6]. For $c_2 > 0$, the atomic interactions are antiferromagnetic (polar), as in ^{23}Na [31], while for $c_2 < 0$ they are ferromagnetic, as in ^{87}Rb [32].

Using Eq. (4) as a trial spinor, we find that $\beta(r)$ satisfies the meron boundary conditions and varies from $\beta(0) = 0$, due to the kinetic energy of the spin texture, to $\beta(\infty) = \pi/2$, due to the atomic Zeeman energy, over a characteristic length scale given by the larger of $(\hbar^2/mg_F\mu_B B')^{1/3}$ and $|B_z|/B'$. We observed that the boundary condition $\beta(0) = 0$ was maintained regardless of the sign of B_z, i.e., atomic spins along the trap axis always remained in the initial state. If the atomic spins had simply followed the local magnetic field, $\beta(r)$ would satisfy $\tan\beta(r) = B'r/B_z$. Thus, scanning B_z from slightly positive to slightly negative would instantaneously change the boundary condition at the origin from $\beta(0) = 0$ to $\beta(0) = \pi$ and flip the atomic spins along the trap axis.

The trial spinor in Eq. (4) does not have the most general form since it was derived by rotating a polarized spinor [Eq. (3)] and is inherently ferromagnetic, $|\vec{F}| = \hbar$. Accordingly, the spin-dependent interaction term in Eq. (5) does not vary with β and therefore does not contribute to the determination of $\beta(r)$. This restriction is not severe since the Zeeman energy dominates the spin-dependent interaction energy in our experiment.

In future experiments, it should be possible to overlap the condensate with an optical dipole trap so that, after ramping $B_z \rightarrow 0$, relaxing the radial magnetic field

gradient would allow for the spin-dependent interactions to determine the evolution of the condensate. It is predicted that skyrmions/merons in condensates with antiferromagnetic (ferromagnetic) interactions are unstable (stable) [9,10,33–39]. Presently, excitations created during the field ramping process have prevented a study of the stability of coreless vortices in an antiferromagnetic ^{23}Na condensate. However, we were able to imprint the spin texture in the presence of an optical dipole trap, as well as produce vortices with a 4π phase winding in an optical dipole trap by fully inverting the axial bias field [18]. At zero magnetic field, it may be possible to observe multiply charged vortices in a spinor condensate "unwind" themselves as predicted in Ref. [6]. The unwinding process is precisely the position-dependent spin rotation demonstrated in previous work [18], with the spin texture investigated here as an intermediate state [37].

In conclusion, we have demonstrated a robust technique for creating coreless vortices in a Bose-Einstein condensate. Our technique can be extended to generate spin textures with arbitrary winding number and variable angular momentum per particle by using higher-order, axisymmetric multipole magnetic fields and condensates with different spin. This work opens up the opportunity to study the stability of topological defects in spinor Bose-Einstein condensates.

We are grateful to K. Machida for bringing the spin texture studied here to our attention. We thank T. Pasquini for experimental assistance and J. R. Anglin and M. Crescimanno for valuable discussions. This work was funded by ONR, NSF, ARO, NASA, and the David and Lucile Packard Foundation.

*Electronic address: http://cua.mit.edu/ketterle_group/

[1] T. H. R. Skyrme, Proc. R. Soc. London A **260**, 127 (1961).
[2] N. D. Mermin and T.-L. Ho, Phys. Rev. Lett. **36**, 594 (1976).
[3] P.W. Anderson and G. Toulouse, Phys. Rev. Lett. **38**, 508 (1977).
[4] R. Blaauwgeers, V. B. Eltsov, M. Krusius, J. J. Ruohio, R. Schanen, and G. E. Volovik, Nature (London) **404**, 471 (2000).
[5] D.-H. Lee and C. L. Kane, Phys. Rev. Lett. **64**, 1313 (1990).
[6] T.-L. Ho, Phys. Rev. Lett. **81**, 742 (1998).
[7] T. Ohmi and K. Machida, J. Phys. Soc. Jpn. **67**, 1822 (1998).
[8] S.-K. Yip, Phys. Rev. Lett. **83**, 4677 (1999).
[9] U. A. Khawaja and H. Stoof, Nature (London) **411**, 918 (2001).
[10] U. A. Khawaja and H.T. C. Stoof, Phys. Rev. A **64**, 043612 (2001).
[11] E. J. Yarmchuk, M. J.V. Gordon, and R. E. Packard, Phys. Rev. Lett. **43**, 214 (1979).
[12] K.W. Madison, F. Chevy, W. Wohlleben, and J. Dalibard, Phys. Rev. Lett. **84**, 806 (2000).
[13] J. R. Abo-Shaeer, C. Raman, J. M. Vogels, and W. Ketterle, Science **292**, 476 (2001).
[14] M. R. Matthews, B. P. Anderson, P. C. Haljan, D. S. Hall, C. E. Wieman, and E. A. Cornell, Phys. Rev. Lett. **83**, 2498 (1999).
[15] Y.V. Gott, M. S. Ioffe, and V. G. Tel'kovskii, Nucl. Fusion (Suppl.) **3**, 1045 (1962).
[16] D. E. Pritchard, Phys. Rev. Lett. **51**, 1336 (1983).
[17] T. Isoshima, M. Nakahara, T. Ohmi, and K. Machida, Phys. Rev. A **61**, 063610 (2000).
[18] A. E. Leanhardt, A. Görlitz, A. P. Chikkatur, D. Kielpinski, Y. Shin, D. E. Pritchard, and W. Ketterle, Phys. Rev. Lett. **89**, 190403 (2002).
[19] M.V. Berry, Proc. R. Soc. London A **392**, 45 (1984).
[20] N. D. Mermin, Rev. Mod. Phys. **51**, 591 (1979).
[21] T. L. Gustavson, A. P. Chikkatur, A. E. Leanhardt, A. Görlitz, S. Gupta, D. E. Pritchard, and W. Ketterle, Phys. Rev. Lett. **88**, 020401 (2002).
[22] A. E. Leanhardt, A. P. Chikkatur, D. Kielpinski, Y. Shin, T. L. Gustavson, W. Ketterle, and D. E. Pritchard, Phys. Rev. Lett. **89**, 040401 (2002).
[23] E. Lundh, C. J. Pethick, and H. Smith, Phys. Rev. A **58**, 4816 (1998).
[24] F. Dalfovo and M. Modugno, Phys. Rev. A **61**, 023605 (2000).
[25] J. Williams and M. J. Holland, Nature (London) **401**, 568 (1999).
[26] J. Ruostekoski, Phys. Rev. A **61**, 041603(R) (2000).
[27] K.-P. Marzlin, W. Zhang, and B. C. Sanders, Phys. Rev. A **62**, 013602 (2000).
[28] U. Leonhardt and G. E. Volovik, JETP Lett. **72**, 46 (2000).
[29] J. Ruostekoski and J. R. Anglin, Phys. Rev. Lett. **86**, 3934 (2001).
[30] H. Pu, S. Raghavan, and N. P. Bigelow, Phys. Rev. A **63**, 063603 (2001).
[31] J. Stenger, S. Inouye, D. M. Stamper-Kurn, H.-J. Miesner, A. P. Chikkatur, and W. Ketterle, Nature (London) **396**, 345 (1998).
[32] N. N. Klausen, J. L. Bohn, and C. H. Greene, Phys. Rev. A **64**, 053602 (2001).
[33] R. A. Battye, N. R. Cooper, and P. M. Sutcliffe, Phys. Rev. Lett. **88**, 080401 (2002).
[34] T. Mizushima, K. Machida, and T. Kita, Phys. Rev. Lett. **89**, 030401 (2002).
[35] T. Isoshima and K. Machida, Phys. Rev. A **66**, 023602 (2002).
[36] Y. Zhang, W.-D. Li, L. Li, and H. J.W. Müller-Kirsten, Phys. Rev. A **66**, 043622 (2002).
[37] J.-P. Martikainen, A. Collin, and K.-A. Suominen, Phys. Rev. A **66**, 053604 (2002).
[38] T. Mizushima, K. Machida, and T. Kita, Phys. Rev. A **66**, 053610 (2002).
[39] H. Zhai, W. Chen, Z. Xu, and L. Chang, cond-mat/0210397.

Appendix F

Cooling Bose-Einstein Condensates Below 500 Picokelvin

This appendix contains the galley proofs for Ref. [124]: A.E. Leanhardt, T.A. Pasquini, M. Saba, A. Schirotzek, Y. Shin, D. Kielpinski, D.E. Pritchard, and W. Ketterle, *Cooling Bose-Einstein Condensates Below 500 Picokelvin*, Science in press, (2003). I was allowed to append these proofs with the following disclaimer: Confidential / Embargoed: Not for Release Until 2 pm ET Thursday, Sept. 11, 2003 / Not for Re-distribution.

NO. RE1088827/CJH/PHYSICS

Cooling Bose-Einstein Condensates Below 500 Picokelvin

A. E. Leanhardt,* T. A. Pasquini, M. Saba, A. Schirotzek, Y. Shin, D. Kielpinski, D. E. Pritchard, W. Ketterle

Spin-polarized gaseous Bose-Einstein condensates were confined by a combination of gravitational and magnetic forces. The partially condensed atomic vapors were adiabatically decompressed by weakening the gravito-magnetic trap to a mean frequency of 1 Hz, then evaporatively reduced in size to 2500 atoms. This lowered the peak condensate density to 5×10^{10} atoms/cm^3 and cooled the entire cloud in all three dimensions to a kinetic temperature of 450 ± 80 pK. Such spin-polarized, dilute, and ultracold gases are important for spectroscopy, metrology, and atom optics.

The pursuit of lower temperatures is motivated by the quest to observe phenomena that occur on very low energy scales, in particular, phase transitions to new forms of matter. The achievement of temperatures near 1 K in solids and in liquids led to the discoveries of superconductivity (*1*) and superfluidity (*2*), respectively. The advent of laser cooling resulted in microkelvin temperature atomic vapors (*3*–*5*), subsequently cooled to nanokelvin temperatures by evaporative cooling to form dilute Bose-Einstein condensates (*6*, *7*) and quantum degenerate Fermi gases (*8*). Collectively, these low-temperature systems have a host of applications, including superconducting quantum interference devices (*9*), superfluid gyroscopes (*10*, *11*), and atomic clocks (*12*).

Temperature is a quantity that parameterizes how energy is distributed across the available states of a system, and effective temperatures can be defined for decoupled degrees of freedom or subsets of particles. For example, nuclear spins isolated from the kinetic motion of their respective atoms have been cooled by adiabatic demagnetization to an effective temperature of 280 pK (*13*). Spin ensembles have a finite number of available states, such that a spin-polarized sample, as in our work, would be characterized by zero effective temperature. In contrast, the motion of free particles is subject to a continuum of states, and the kinetic temperature of an ensemble can only asymptotically approach absolute zero.

Effective temperatures in atomic vapors are defined by the widths of velocity distributions, which can be much smaller than the mean velocity of the sample. Raman cooling (*14*, *15*) and velocity-selective coherent population trapping (*16*) have generated velocity distributions with very narrow peaks, corresponding to nanokelvin and picokelvin effective temperatures. However, these temperatures were associated with the motion of only a subset of the atoms in the cloud and/or with atomic motion in only one dimension.

For trapped, partially condensed atomic vapors, the condensate fraction has zero entropy and the kinetic temperature of the sample is determined by the velocity distribution of the thermal (noncondensed) component. When released, the condensate fraction expands more slowly than the thermal component and has been characterized by picokelvin effective temperatures for anisotropic (*17*) and noninteracting (*18*) gases.

Cooling the atomic motion of entire ensembles in all three dimensions has proven difficult. To date, kinetic temperatures of a few hundred nanokelvin have been achieved with adiabatic and optical cooling (*19*, *20*), and evaporative cooling techniques have produced condensates with temperatures of 3 nK (*21*). By adiabatic expansion and subsequent evaporation, we have cooled partially condensed atomic vapors to picokelvin kinetic temperatures.

Our thermometry is calibrated by the Bose-Einstein condensation (BEC) phase transition temperature, T_c, which in the thermodynamic limit for a harmonically trapped ideal Bose gas is (*22*)

$$k_B T_c = \hbar\bar{\omega}\left(\frac{N}{\zeta(3)}\right)^{1/3} \approx 0.94\hbar\bar{\omega}N^{1/3} \qquad (1)$$

where k_B is Boltzmann's constant, $\hbar$ is Planck's constant h divided by 2π, $\zeta(n)$ is the Riemann Zeta function, $\bar{\omega} = (\omega_x\omega_y\omega_z)^{1/3}$ is the geometric mean of the harmonic trap frequencies, and N is the total number of atoms, both condensed and noncondensed. Thus, the atom number and the trap frequencies set an upper limit for the temperature of a confined Bose-Einstein condensate. In our work, adiabatically weakening the trapping potential to a mean frequency of $\bar{\omega} = 2\pi \times (1.12 \pm 0.08)$ Hz guaranteed that partially condensed atomic vapors with $N \leq 8000$ atoms had picokelvin temperatures ($T_c \leq 1$ nK).

Bose-Einstein condensates containing more than 10^7 ^{23}Na atoms were created in the weak field seeking $|F = 1, m_F = -1\rangle$ state in a magnetic trap, captured in the focus of an optical tweezers laser beam, and transferred into an auxiliary "science" chamber as described in (*23*). In the science chamber, condensates containing 2×10^6 to 3×10^6 atoms were transferred from the optical tweezers into a gravito-magnetic trap (Fig. 1A). A small coil carrying current I_S generated a vertical bias field B_z and supported the condensates against gravity with a vertical magnetic field gradient, $B'_z = 2\,mg/\mu_B \approx 8$ G/cm, where m is the atomic mass, g is the

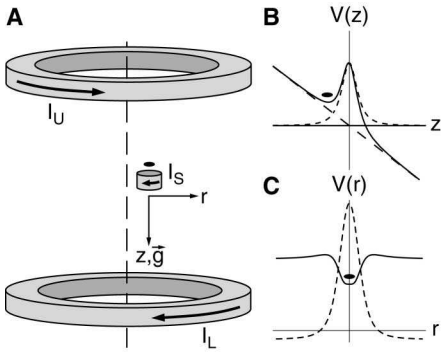

Fig. 1. Gravito-magnetic trap. (**A**) Bose-Einstein condensates were levitated against gravity ~5 mm above a 1-cm diameter, 25-turn coil mounted inside the ultrahigh vacuum chamber running current I_S. Two 10-cm diameter, 20-turn coils were mounted outside the vacuum chamber and were supplied individually with currents I_U and I_L. The vertical separation between the large coils was 10 cm. The 1-cm diameter coil was mounted radially off-axis with respect to the pair of 10-cm diameter coils by ~1 cm. This broke the cylindrical symmetry of the trapping potential. Additional bias fields of ~1 G were applied in the horizontal plane to cancel the radial magnetic fields generated by I_U and I_L on the axis of the small coil and to maintain a stable trapping potential. $\vec{g}$ denotes the direction of gravitational acceleration. (**B**) Magnetic potential due to I_S (short dashed line), gravitation potential (long dashed line), and joint vertical potential of the gravito-magnetic trap (solid line). (**C**) A radially repulsive potential magnetic potential was generated by running I_S alone (dashed line); however, applying a slight antibias field with I_U modified the radial energy profile and created a magnetic field minimum at $r = 0$ (solid line). In (A) to (C), the solid oval denotes the trapped condensate.

Department of Physics, MIT-Harvard Center for Ultracold Atoms, and Research Laboratory of Electronics, Massachusetts Institute of Technology, Cambridge, MA 02139, USA.
*To whom correspondence should be addressed. E-mail: ael@mit.edu

rich4/se-sci/se-sci/se-orig/se1850d03r | byrds | S=8 | 8/25/03 | 22:56 | Art: Fig. 1 - live B&W

gravitational acceleration, and μ_B is the Bohr magneton. Additional control over B_z and B'_z was provided by two external coils carrying independent currents I_U and I_L. Weak curvature, B''_z, to the vertical bias field created stable vertical confinement such that a harmonic restoring force was provided magnetically (gravitationally) for downward (upward) vertical displacements (Fig. 1B). A radial field gradient, $B'_r = \partial B_r / \partial r = -B'_z/2$, was also present and added in quadrature with B_z to provide harmonic radial confinement with a restoring force proportional to $(B'_r)^2/B_z$ (Fig. 1C). The trapping potential does not have fundamental radial asymmetries as do previously demonstrated Ioffe-Pritchard magnetic traps (*17*, *24*, *25*). In principle, stable three-dimensional confinement is possible above a single coil in the presence of gravity without the aid of external bias fields or gradients.

For typical loading parameters—I_S = 340 mA, I_U = 5.5 A, and I_L = 0—the gravito-magnetic trap was spherically symmetric, with trap frequencies $\omega_x \approx \omega_y \approx \omega_z \approx 2\pi \times$ 8 Hz. Condensates loaded into the gravito-magnetic trap from the optical tweezers were held for 5 s to allow for the damping of excitations. The resulting partially condensed clouds had ~5 × 10^5 atoms and a BEC transition temperature T_c = 30 nK. Throughout our work, the atomic vapor maintained a temperature T such that $0.5 < T/T_c < 1$.

Further cooling was accomplished by adiabatically decompressing the trapping potential in two 5 s stages, with a 5 s delay in between to allow excitations to damp. In the first stage, the vertical frequency was reduced to $\omega_z = 2\pi \times (1.81 \pm 0.05)$ Hz by simultaneously raising currents I_L and I_U by identical amounts and lowering the current I_S by a factor of 10. This transferred the dominant source of magnetic field gradient from the small coil to the external coils, with the remaining vertical curvature still due to the reduced I_S. In the second stage, the radial frequencies were reduced to $\omega_x = 2\pi \times (0.65 \pm 0.05)$ Hz and $\omega_y = 2\pi \times (1.2 \pm 0.1)$ Hz by raising I_L and lowering I_U by identical amounts. The vertical magnetic field gradient and curvature remained constant, but the vertical bias field, B_z, increased. This reduced the radial confinement due to the scaling $\omega_r \propto B'_r / B^{1/2}_z$ (*24*, *25*).

For currents I_S = 34 mA, I_U = 14 A, and I_L = 44 A, the final gravito-magnetic trap had a measured mean frequency $\varpi = 2\pi \times (1.12 \pm 0.08)$ Hz and axial bias field B_z = 17 G. The residual anharmonicities of the trapping potential were small, with $\Delta\omega/\omega = 0.1$ for 500 μm displacements from the trap center. Further radial decompression was not possible because of a finite trap depth (Fig. 1C) and sensitivity of trap stability to milligauss level radial bias fields.

After decompression, the partially condensed atomic vapors had ~2 × 10^5 atoms and a BEC transition temperature T_c = 3 nK. T_c was lowered further by reducing the number of atoms in the cloud (Eq. 1), while maintaining a substantial condensate fraction at all times ($0.5 < T/T_c < 1$). The atom number was reduced by holding the atoms in the gravito-magnetic trap for up to 200 s. Often, microwave radiation near the $|1, -1\rangle \rightarrow |2, 0\rangle$ transition was applied to shorten the hold time required to arrive at lower atom number to 10 s. The atom number reduction was accompanied by cooling, during which the elastic collision rate (between thermal atoms and the condensate) dropped from 0.25 Hz to 0.01 Hz. Therefore, a few collisions were sufficient to cause evaporation out of the finite depth trap. This cooling was not efficient in the sense of providing a gain in phase-space density but still was capable of maintaining thermal equilibrium and lowering the absolute temperature of the vapor.

Using this technique, we cooled partial condensed vapors containing up to 30,000 atoms to temperatures below 1 nK (Figs. 2 and 3). Our lowest measured three-dimensional kinetic temperature was 450 ± 80 pK for 2500 atoms at a peak condensate density of 5 × 10^{10} atoms/cm^3. Under these conditions, the peak atom-atom interaction energy was $\mu = k_B \times$ 33 pK, while the zero point energy of the harmonic trapping potential was $(1/2)\hbar\,\varpi\, k_B \times$ 24 pK. Condensates released from the gravito-magnetic trap would expand with energies of this order and therefore could be characterized by effective temperatures ~30 pK.

Additional cooling would require lowering the trap frequencies further or reducing the atom number more. However, weakly confining traps have proven technically difficult to control such that lowering $\varpi/2\pi$ substantially below 1 Hz is challenging. Likewise, because $T_c \propto N^{1/3}$, atom number reduction by an order of magnitude only results in temperature reduction by a factor of two. Furthermore, lower temperatures and lower densities are accompanied by collisional equilibrium times approaching 100 s.

Because $\mu \approx \hbar\varpi$, the condensates in the gravito-magnetic trap were in a density regime intermediate between the Thomas-Fermi ($\mu >> \hbar\,\varpi$) and ideal ($\mu << \hbar\varpi$) gas limits. No simple approximation describes the condensate wave function, but the number of thermal atoms, $N_{th} = \zeta(3) \times (k_B\, T\, \hbar\varpi)^3$, and the width of their distribution, $w_{th} = (2k_B\, T / m\omega^2)^{1/2}$, in any spatial direction can be related to the temperature, provided that the thermal energy is much larger than the trap level spacing, $k_B\, T \gg \hbar\,\varpi$, where ω is the trap frequency for the axis along which w_{th} is measured (*22*). The ratio of atoms in the condensate, N_0, to the total number of atoms, $N = N_0 + N_{th}$, is also related to the temperature through $N_0/N =$

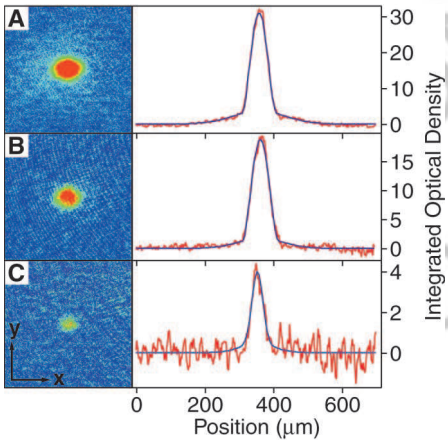

Fig. 2. Picokelvin temperature thermometry. Partially condensed atomic vapors confined in the gravito-magnetic trap with (**A**) 28,000, (**B**) 16,000, and (**C**) 2,500 atoms. The one-dimensional cross sections (red) were obtained by integrating the two-dimensional absorption images of the trapped clouds along the *y* axis. Bimodal fits to Eq. 2 (blue) yielded temperatures of (A) 1.05 ± 0.08 nK, (B) 780 ± 50 pK, and (C) 450 ± 80 pK, where the uncertainty is due to the fit of an individual image. The absorption imaging light was resonant with the $F = 2 \rightarrow F' = 3$ cycling transition for the trapped atoms and was aligned with the vertical (*z*) axis. The atoms were optically pumped into the $F = 2$ hyperfine level with a pulse resonant with the $F = 1 \rightarrow F' = 2$ transition. The field of view for the absorption images in (A) to (C) is 460 μm × 460 μm.

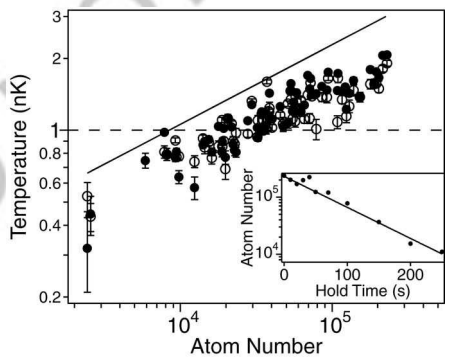

Fig. 3. Bose-Einstein condensates at picokelvin temperatures. The temperature of more than 60 partially condensed atomic vapors is plotted versus total number of condensed and noncondensed atoms. A solid line at the Bose-Einstein condensation phase transition temperature (Eq. 1) and a dashed line at 1 nK are provided as guides. Condensate temperatures were determined from one-dimensional fits to atomic density cross sections integrated along either the *x* (closed circles) or *y* (open circles) axis (Fig. 2). Differences in the two measured temperatures for a single condensate reflect the true uncertainty of the measurement. Plotted error bars represent the statistical uncertainty of the fit. The inset shows that the 1/*e* condensate lifetime in the gravito-magnetic trap was limited by one-body processes to 80 ± 5 s.

$1 - (T/T_c)^3$. N_0, N_{th}, and w_{th} are therefore completely determined by T and N.

The temperature of the atomic vapors was extracted by fitting integrated, one-dimensional atomic density cross sections to a bimodal distribution (Fig. 2)

$$n(x) = N_0\Psi_0^2 + \frac{N_{th}}{\sqrt{\pi}w_{th}} e^{-x^{2/w_{th}^2}}, \quad (2)$$

where Ψ_0^2 is a bell-shaped function with width w_0 that describes the condensate peak [$\Psi_0^2 = (15/16)\, w_0^{-1} \max(1 - x^2/w_0^2, 0)^2$ for a Thomas-Fermi gas and $\Psi_0^2 = w_0^{-1}\pi^{-1/2} \exp(-x^2/w_0^2)$ for an ideal gas]. The fitted parameters were T, N, and w_0. We checked that the fitted temperature did not depend on the exact choice of the condensate wave function (inverted parabola or gaussian) or the application of microwave radiation to reduce atom number.

All atomic vapors represented in Fig. 3 had a clear bimodal density distribution from which a temperature was reproducibly extracted. The temperatures extracted from one-dimensional fits along both radial axes were nominally the same, empirically indicating that the atomic vapors remained close to thermal equilibrium at all times.

In conclusion, we have created long-lived (80 ± 5 s), low-temperature (450 ± 80 pK), and low-density (5×10^{10} atoms/cm^3) partially condensed atomic vapors using a weakly confining [$\varpi = 2\pi \times (1.12 \pm 0.08)$ Hz] gravito-magnetic trap. These samples are characterized by a thermal velocity ~1 mm/s, a speed of sound ~100 μm/s, and a healing length limited by the ~20-μm harmonic oscillator length of the trapping potential. Low-temperature and low-density ensembles are important for spectroscopy, metrology, and atom optics. In addition, they are predicted to experience quantum reflection from material surfaces (*26–28*).

References and Notes

1. H. G. Smith, J. O. Wilhelm, *Rev. Mod. Phys.* **7**, 237 (1935).
2. K. Darrow, *Rev. Mod. Phys.* **12**, 257 (1940).
3. S. Chu, *Rev. Mod. Phys.* **70**, 685 (1998).
4. C. N. Cohen-Tannoudji, *Rev. Mod. Phys.* **70**, 707 (1998).
5. W. D. Phillips, *Rev. Mod. Phys.* **70**, 721 (1998).
6. E. A. Cornell, C. E. Wieman, *Rev. Mod. Phys.* **74**, 875 (2002).
7. W. Ketterle, *Rev. Mod. Phys.* **74**, 1131 (2002).
8. B. DeMarco, D. S. Jin, *Science* **285**, 1703 (1999).
9. A. H. Silver, J. E. Zimmerman, *Phys. Rev. Lett.* **15**, 888 (1965).
10. K. Schwab, N. Bruckner, R. E. Packard, *Nature* **386**, 585 (1997).
11. O. Avenel, P. Hakonen, E. Varoquaux, *Phys. Rev. Lett.* **78**, 3602 (1997).
12. T. Udem, R. Holzwarth, T. W. Hänsch, *Nature* **416**, 233 (2002).
13. A. S. Oja, O. V. Lounasmaa, *Rev. Mod. Phys.* **69**, 1 (1997).
14. M. Kasevich, S. Chu, *Phys. Rev. Lett.* **69**, 1741 (1992).
15. J. Reichel, *et al.*, *Phys. Rev. Lett.* **75**, 4575 (1995).
16. B. Saubaméa, *et al.*, *Phys. Rev. Lett.* **79**, 3146 (1997).
17. M.-O. Mewes, *et al.*, *Phys. Rev. Lett.* **77**, 416 (1996).
18. T. Weber, J. Herbig, M. Mark, H.-C. Nägerl, R. Grimm, *Science* **299**, 232 (2003).
19. A. Kastberg, W. D. Phillips, S. L. Rolston, R. J. C. Spreeuw, *Phys. Rev. Lett.* **74**, 1542 (1995).
20. P. Treutlein, K. Y. Chung, S. Chu, *Phys. Rev. A* **63**, 051401(R) (2001).
21. E. A. Donley, N. R. Claussen, S. T. Thompson, C. E. Wieman, *Nature* **417**, 529 (2002).
22. F. Dalfovo, S. Giorgini, L. P. Pitaeskii, S. Stringari, *Rev. Mod. Phys.* **71**, 463 (1999).
23. T. L. Gustavson, *et al.*, *Phys. Rev. Lett.* **88**, 020401 (2002).
24. Y. V. Gott, M. S. Ioffe, V. G. Tel'kovskii, *Nuc. Fus. Suppl.* **3**, 1045 (1962).
25. D. E. Pritchard, *Phys. Rev. Lett.* **51**, 1336 (1983).
26. A. Anderson *et al.*, *Phys. Rev. A* **34**, 3513 (1986).
27. J. J. Berkhout *et al.*, *Phys. Rev. Lett.* **63**, 1689 (1989).
28. F. Shimizu, *Phys. Rev. Lett.* **86**, 987 (2001).

29. This work was funded by the Army Research Office, NSF, Office of Naval Research, and NASA. We thank C. V. Nielsen for experimental assistance and J. K. Thompson for critical comments on the manuscript. M.S. acknowledges additional support from the Swiss National Science Foundation.

7 July 2003; accepted 12 August 2003

Article is 410 picas

Bibliography

[1] J. R. Abo-Shaeer, C. Raman, J. M. Vogels, and W. Ketterle. Observation of vortex lattices in Bose-Einstein condensates. *Science*, 292:476–479, April 2001.

[2] J. F. Allen and A. D. Misener. Flow of liquid helium II. *Nature*, 141:75, January 1938.

[3] A. Anderson, S. Haroche, E. A. Hinds, W. Jhe, D. Meschede, and L. Moi. Reflection of thermal Cs atoms grazing a polished glass surface. *Phys. Rev. A*, 34:3513–3516, October 1986.

[4] B. P. Anderson, P. C. Haljan, C. A. Regal, D. L. Feder, L. A. Collins, C. W. Clark, and E. A. Cornell. Watching dark solitons decay into vortex rings in a Bose-Einstein condensate. *Phys. Rev. Lett.*, 86:2926–2929, April 2001.

[5] B. P. Anderson and M. A. Kasevich. Macroscopic quantum interference from atomic tunnel arrays. *Science*, 282:1686–1689, November 1998.

[6] M H. Anderson, J. R. Ensher, M. R. Matthews, C. E. Wieman, and E. A. Cornell. Observation of Bose-Einstein condensation in a dilute atomic vapor. *Science*, 269:198–201, July 1995.

[7] P. W. Anderson and G. Toulouse. Phase slippage without vortex cores: Vortex textures in superfluid ^{3}He. *Phys. Rev. Lett.*, 38:508–511, February 1977.

[8] E. Andersson, T. Calarco, R. Folman, M. Andersson, B. Hessmo, and J. Schmiedmayer. Multimode interferometer for guided matter waves. *Phys. Rev. Lett.*, 88:100401, March 2002.

[9] M. R. Andrews, C. G. Townsend, H.-J. Miesner, D. S. Durfee, D. M. Kurn, and W. Ketterle. Observation of interference between two Bose-Einstein condensates. *Science*, 275:637–641, January 1997.

[10] A. Ashkin. Trapping of atoms by resonance radiation pressure. *Phys. Rev. Lett.*, 40:729–732, March 1978.

[11] O. Avenel, P. Hakonen, and E. Varoquaux. Detection of the rotation of the Earth with a superfluid gyroscope. *Phys. Rev. Lett.*, 78:3602–3605, May 1997.

[12] J. Bardeen, L. N. Cooper, and J. R. Schrieffer. Theory of superconductivity. *Phys. Rev.*, 108:1175–1204, December 1957.

[13] R. A. Battye, N. R. Cooper, and P. M. Sutcliffe. Stable skyrmions in two-component Bose-Einstein condensates. *Phys. Rev. Lett.*, 88:080401, February 2002.

[14] J. J. Berkhout, O. J. Luiten, I. D. Setija, T. W. Hijmans, T. Mizusaki, and J. T. M. Walraven. Quantum reflection: Focusing of hydrogen atoms with a concave mirror. *Phys. Rev. Lett.*, 63:1689–1692, October 1989.

[15] P. R. Berman, editor. *Cavity Quantum Electrodynamics*. Academic Press, New York, 1994.

[16] P. R. Berman, editor. *Atom Interferometry*. Academic Press, New York, 1997.

[17] M. V. Berry. Quantal phase factors accompanying adiabatic changes. *Proc. R. Soc. Lond. A*, 392:45–57, March 1984.

[18] R. Blaauwgeers, V. B. Eltsov, M. Krusius, J. J. Ruohio, R. Schanen, and G. E. Volovik. Double-quantum vortex in superfluid ^{3}He-A. *Nature*, 404:471–473, March 2000.

[19] N. N. Bogoliubov. A new method in the theory of superconductivity. I. *Sov. Phys. JETP*, 7:41–46, July 1958.

[20] N. N. Bogoliubov. A new method in the theory of superconductivity. III. *Sov. Phys. JETP*, 7:51–55, July 1958.

[21] C. C. Bradley, C. A. Sackett, and R. G. Hulet. Bose-Einstein condensation of lithium: Observation of limited condensate number. *Phys. Rev. Lett.*, 78:985–989, Februrary 1997.

[22] C. C. Bradley, C. A. Sackett, J. J. Tollett, and R. G. Hulet. Evidence of Bose-Einstein condensation in an atomic gas with attractive interactions. *Phys. Rev. Lett.*, 75:1687–1690, August 1995.

[23] E. N. Bulgakov and A. F. Sadreev. Vortex phase diagram of $F = 1$ spinor Bose-Einstein condensates. *Phys. Rev. Lett.*, 90:200401, May 2003.

[24] S. Burger, F. S. Cataliotti, C. Fort, F. Minardi, M. Inguscio, M. L. Chiofalo, and M. P. Tosi. Superfluid and dissipative dynamics of a Bose-Einstein condensate in a periodic optical potential. *Phys. Rev. Lett.*, 86:4447–4450, May 2001.

[25] E. A. Burt, R. W. Ghrist, C. J. Myatt, M. J. Holland, E. A. Cornell, and C. E. Wieman. Coherence, correlations, and collisions: What one learns about Bose-Einstein condensates from their decay. *Phys. Rev. Lett.*, 79:337–340, July 1997.

[26] O. Carnal and J. Mlynek. Young's double-slit experiment with atoms: A simple atom interferometer. *Phys. Rev. Lett.*, 66:2689–2692, May 1991.

[27] D. Cassettari, B. Hessmo, R. Folman, T. Maier, and J. Schmiedmayer. Beam splitter for guided atoms. *Phys. Rev. Lett.*, 85:5483–5487, December 2000.

[28] Y. Castin and R. Dum. Bose-Einstein condensates in time dependent traps. *Phys. Rev. Lett.*, 77:5315–5319, December 1996.

[29] Y. Castin and R. Dum. Bose-Einstein condensates with vortices in rotating traps. *Euro. Phys. J. D*, 7:399–412, October/November 1999.

[30] F. S. Cataliotti, S. Burger, C. Fort, P. Maddaloni, F. Minardi, A. Trombettoni, A. Smerzi, and M. Inguscio. Josephson junction arrays with Bose-Einstein condensates. *Science*, 293:843–846, August 2001.

[31] M. S. Chapman, T. D. Hammond, A. Lenef, J. Schmiedmayer, R. A. Rubenstein, E. Smith, and D. E. Pritchard. Photon scattering from atoms in an atom interferometer: Coherence lost and regained. *Phys. Rev. Lett.*, 75:3783–3787, November 1995.

[32] F. Chevy, K. W. Madison, and J. Dalibard. Measurement of the angular momentum of a rotating Bose-Einstein condensate. *Phys. Rev. Lett.*, 85:2223–2227, September 2000.

[33] A. P. Chikkatur. *Colliding and Moving Bose-Einstein Condensates: Studies of superfluidity and optical tweezers for condensate transport.* Ph.D. Thesis, Massachusetts Institute of Technology, October 2002.

[34] A. P. Chikkatur, A. Görlitz, D. M. Stamper-Kurn, S. Inouye, S. Gupta, and W. Ketterle. Suppression and enhancement of impurity scattering in a Bose-Einstein condensate. *Phys. Rev. Lett.*, 85:483–486, July 2000.

[35] A. P. Chikkatur, Y. Shin, A. E. Leanhardt, D. Kielpinski, E. Tsikata, T. L. Gustavson, D. E. Pritchard, and W. Ketterle. A continuous source of Bose-Einstein condensed atoms. *Science*, 296:2193–2195, June 2002.

[36] W. W. Chow, J. Gea-Banacloche, L. M. Pedrotti, V. E. Sanders, W. Schleich, and M. O. Scully. The ring laser gyro. *Rev. Mod. Phys.*, 57:61–104, January 1985.

[37] S. Chu. The manipulation of neutral particles. *Rev. Mod. Phys.*, 70:685–706, July 1998.

[38] S. Chu, J. E. Bjorkholm, A. Ashkin, and A. Cable. Experimental observation of optically trapped atoms. *Phys. Rev. Lett.*, 57:314–317, July 1986.

[39] C. N. Cohen-Tannoudji. Manipulating atoms with photons. *Rev. Mod. Phys.*, 70:707–719, July 1998.

[40] E. A. Cornell and C. E. Wieman. Nobel lecture: Bose-Einstein condensation in a dilute gas, the first 70 years and some recent experiments. *Rev. Mod. Phys.*, 74:875–893, July 2002.

[41] S. L. Cornish, N. R. Claussen, J. L. Roberts, E. A. Cornell, and C. E. Wieman. Stable ^{85}Rb Bose-Einstein condensates with widely tunable interactions. *Phys. Rev. Lett.*, 85:1795–1798, August 2000.

[42] F. Dalfovo, S. Giorgini, L. P. Pitaevskii, and S. Stringari. Theory of Bose-Einstein condensation in trapped gases. *Rev. Mod. Phys.*, 71:463–512, April 1998.

[43] F. Dalfovo and M. Modugno. Free expansion of Bose-Einstein condensates with quantized vortices. *Phys. Rev. A*, 61:023605, February 2000.

[44] F. Dalfovo, L. Pitaevskii, and S. Stringari. Order parameter at the boundary of a trapped Bose gas. *Phys. Rev. A*, 54:4213–4217, November 1996.

[45] B. Damski, J. Zakrzewski, L. Santos, P. Zoller, and M. Lewenstein. Atomic Bose and Anderson glasses in optical lattices. *Phys. Rev. Lett.*, 91:080403, August 2003.

[46] K. B. Davis, M.-O. Mewes, M. R. Andrews, N. J. van Druten, D. S. Durfee, D. M. Kurn, and W. Ketterle. Bose-Einstein condensation in a gas of sodium atoms. *Phys. Rev. Lett.*, 75:3969–3973, November 1995.

[47] N. H. Dekker, C. S. Lee, V. Lorent, J. H. Thywissen, S. P. Smith, M. Drndić, R. M. Westervelt, and M. Prentiss. Guiding neutral atoms on a chip. *Phys. Rev. Lett.*, 84:1124–1127, Feburary 2000.

[48] B. DeMarco and D. S. Jin. Onset of Fermi degeneracy in a trapped atomic gas. *Science*, 285:1703–1706, September 1999.

[49] L. Deng, E. W. Hagley, J. Wen, M. Trippenbach, Y. Band, P. S. Julienne, J. E. Simsarian, K. Helmerson, S. L. Rolston, and W. D. Phillips. Four-wave mixing with matter waves. *Nature*, 398:218–220, March 1999.

[50] S. Dettmer, D. Hellweg, P. Ryytty, J. J. Arlt, W. Ertmer, K. Sengstock, D. S. Petrov, G. V. Shlyapnikov, H. Kreutzmann, L. Santos, and M. Lewenstein. Observation of phase fluctuations in elongated Bose-Einstein condensates. *Phys. Rev. Lett.*, 87:160406, October 2001.

[51] E. A. Donley, N. R. Claussen, S. T. Thompson, and C. E. Wieman. Atom-molecule coherence in a Bose-Einstein condensate. *Nature*, 417:529–533, May 2002.

[52] R. Dumke, T. Müther, M. Volk, W. Ertmer, and G. Birkl. Interferometer-type structures for guided atoms. *Phys. Rev. Lett.*, 89:220402, November 2002.

[53] R. Dumke, M. Volk, T. Müther, F. B. J. Buchkremer, G. Birkl, and W. Ertmer. Micro-optical realization of arrays of selectively addressable dipole traps: A scalable configuration of quantum computation with atomic qubits. *Phys. Rev. Lett.*, 89:097903, August 2002.

[54] V. Dunjko, V. Lorent, and M. Olshanii. Bosons in cigar-shaped traps: Thomas-Fermi regime, Tonks-Girardeau regime, and in between. *Phys. Rev. Lett.*, 86:5413–5416, June 2001.

[55] Z. Dutton, M. Budde, C. Slowe, and L. V. Hau. Observation of quantum shock waves created with ultra-compressed slow light pulses in a Bose-Einstein condensate. *Science*, 293:663–668, July 2001.

[56] C. R. Ekstrom, J. Schmiedmayer, M. S. Chapman, T. D. Hammond, and D. E. Pritchard. Measurement of the electric polarizability of sodium with an atom interferometer. *Phys. Rev. A*, 51:3883–3888, May 1995.

[57] P. Engels, I. Coddington, P. C. Haljan, V. Schweikhard, and E. A. Cornell. Observation of long-lived vortex aggregates in rapidly rotating Bose-Einstein condensates. *Phys. Rev. Lett.*, 90:170405, May 2003.

[58] L. Feenstra, L. M. Andersson, and J. Schmiedmayer. Microtraps and atom chips: Toolboxes for cold atom physics. *arXiv:cond-mat/0302059*, February 2003.

[59] M. P. A. Fisher, P. B. Weichman, G. Grinstein, and D. S. Fisher. Boson localization and the superfluid-insulator transition. *Phys. Rev. B*, 40:546–570, July 1989.

[60] R. Folman, P. Krüger, D. Cassettari, B. Hessmo, T. Maier, and J. Schmiedmayer. Controlling cold atoms using nanofabricated surfaces: Atom chips. *Phys. Rev. Lett.*, 84:4749–4752, May 2000.

[61] R. Folman, P. Krüger, J. Schmiedmayer, J. Denschlag, and C. Henkel. Microscopic atom optics: From wires to an atom chip. *Adv. At. Mol. Opt. Phys.*, 48:263–356, 2002.

[62] J. Fortágh, H. Ott, S. Kraft, A. Günther, and C. Zimmermann. Surface effects in magnetic microtraps. *Phys. Rev. A*, 66:041604, October 2002.

[63] D. G. Fried, T. C. Killian, L. Willmann, D. Landhuis, S. C. Moss, D. Kleppner, and T. J. Greytak. Bose-Einstein condensation of atomic hydrogen. *Phys. Rev. Lett.*, 81:3811–3814, November 1998.

[64] T. Giamarchi and H. J. Schulz. Anderson localization and interactions in one-dimensional metals. *Phys. Rev. B*, 37:325–340, January 1988.

[65] M. Girardeau. Relationship between systems of impenetrable Bosons and Fermions in one dimension. *J. Math. Phys.*, 1:516–523, November/December 1960.

[66] A. Görlitz, T. L. Gustavson, A. E. Leanhardt, R. Löw, A. P. Chikkatur, S. Gupta, S. Inouye, D. E. Pritchard, and W. Ketterle. Sodium Bose-Einstein condensates in the $F = 2$ state in a large-volume optical trap. *Phys. Rev. Lett.*, 90:090401, March 2003.

[67] A. Görlitz, J. M. Vogels, A. E. Leanhardt, C. Raman, T. L. Gustavson, J. R. Abo-Shaeer, A. P. Chikkatur, S. Gupta, S. Inouye, T. Rosenband, and W. Ketterle. Realization of Bose-Einstein condensates in lower dimensions. *Phys. Rev. Lett.*, 87:130402, September 2001.

[68] Y. V. Gott, M. S. Ioffe, and V. G. Tel'kovskii. *Nuclear Fusion Supplement*, 3:1045, 1962.

[69] M. Greiner, I. Bloch, O. Mandel, T. W. Hänsch, and T. Esslinger. Exploring phase coherence in a 2D lattice of Bose-Einstein condensates. *Phys. Rev. Lett.*, 87:160405, October 2001.

[70] M. Greiner, O. Mandel, T. Esslinger, T. W. Hänsch, and I. Bloch. Quantum phase transition from a superfluid to a Mott insulator in a gas of ultracold atoms. *Nature*, 415:39–44, January 2002.

[71] S. Gupta, K. Dieckmann, Z. Hadzibabic, and D. E. Pritchard. Contrast interferometry using Bose-Einstein condensates to measure h/m and α. *Phys. Rev. Lett.*, 89:140401, September 2002.

[72] S. Gupta, A. E. Leanhardt, A. D. Cronin, and D. E. Pritchard. Coherent manipulation of atoms with standing light waves. *C. R. Acad. Sci. IV-Phys.*, 2:479–495, April-May 2001.

[73] T. L. Gustavson, P. Bouyer, and M. A. Kasevich. Precision rotation measurements with an atom interferometer gyroscope. *Phys. Rev. Lett.*, 78:2046–2049, March 1997.

[74] T. L. Gustavson, A. P. Chikkatur, A. E. Leanhardt, A. Görlitz, S. Gupta, D. E. Pritchard, and W. Ketterle. Transport of Bose-Einstein condensates with optical tweezers. *Phys. Rev. Lett.*, 88:020401, January 2002.

[75] Z. Hadzibabic, S. Gupta, C. A. Stan, C. H. Schunck, M. W. Zwierlein, K. Dieckmann, and W. Ketterle. Fifty-fold improvement in the number of quantum degenerate fermionic atoms. *arXiv:cond-mat/0306050*, June 2003.

[76] E. W. Hagley, L. Deng, M. Kozuma, M. Trippenbach, Y. B. Band, M. Edwards, M. Doery, P. S. Julienne, K. Helmerson, S. L. Rolston, and W. D. Phillips. Measurement of the coherence of a Bose-Einstein condensate. *Phys. Rev. Lett.*, 83:3112–3115, October 1999.

[77] P. C. Haljan, B. P. Anderson, I. Coddington, and E. A. Cornell. Use of surface-wave spectroscopy to characterize tilt modes of a vortex in a Bose-Einstein condensate. *Phys. Rev. Lett.*, 86:2922–2925, April 2001.

[78] P. C. Haljan, I. Coddington, P. Engels, and E. A. Cornell. Driving Bose-Einstein-condensate vorticity with a rotating normal cloud. *Phys. Rev. Lett.*, 87:210403, November 2001.

[79] D. S. Hall, M. R. Matthews, C. E. Wieman, and E. A. Cornell. Measurements of relative phase in two-component Bose-Einstein condensates. *Phys. Rev. Lett.*, 81:1543–1546, August 1998.

[80] W. Hänsel, P. Hommelhoff, T. W. Hänsch, and J. Reichel. Bose-Einstein condensation on a microelectric chip. *Nature*, 413:498–501, October 2001.

[81] W. Hänsel, J. Reichel, P. Hommelhoff, and T. W. Hänsch. Magnetic conveyor belt for transporting and merging trapped atom clouds. *Phys. Rev. Lett.*, 86:608–611, January 2001.

[82] D. M. Harber, J. M. McGuirk, J. M. Obrecht, and E. A. Cornell. Thermally induced losses in ultra-cold atoms magnetically trapped near room-temperature surfaces. *arXiv:cond-mat/0307546*, July 2003.

[83] D. Hellweg, L. Cacciapuoti, M. Kottke, T. Schulte, K. Sengstock, W. Ertmer, and J. J. Arlt. Measurement of the spatial correlation function of phase fluctuating Bose-Einstein condensates. *Phys. Rev. Lett.*, 91:010406, July 2003.

[84] C. Henkel and S. A. Gardiner. Spatial decoherence of Bose-Einstein condensates in microtraps. *arXiv:cond-mat/0212415*, December 2002.

[85] C. Henkel, P. Krüger, R. Folman, and J. Schmiedmayer. Fundamental limits for coherent manipulation on atom chips. *Appl. Phys. B*, 76:173–182, February 2003.

[86] C. Henkel and S. Pötting. Coherent transport of matter waves. *Appl. Phys. B*, 72:73–80, January 2001.

[87] C. Henkel, S. Pötting, and M. Wilkens. Loss and heating of particles in small and noisy traps. *Appl. Phys. B*, 69:379–387, December 1999.

[88] C. Henkel and M. Wilkins. Heating of trapped atoms near thermal surfaces. *Europhys. Lett.*, 47:414–420, August 1999.

[89] E. A. Hinds and I. G. Hughes. Magnetic atom optics: mirrors, guides, traps, and chips for atoms. *J. Phys. D: Appl. Phys.*, 32:R119–R146, September 1999.

[90] E. A. Hinds, C. J. Vale, and M. G. Boshier. Two-wire waveguide and interferometer for cold atoms. *Phys. Rev. Lett.*, 86:1462–1465, Feburary 2001.

[91] T.-L. Ho. Spinor Bose condensate in optical traps. *Phys. Rev. Lett.*, 81:742–745, July 1998.

[92] E. Hodby, G. Hechenblaikner, S. A. Hopkins, O. M. Maragò, and C. J. Foot. Vortex nulceation in Bose-Einstin condensates in an oblate, purely magnetic potential. *Phys. Rev. Lett.*, 88:010405, January 2002.

[93] E. Hodby, S. A. Hopkins, G. Hechenblaikner, N. L. Smith, and C. J. Foot. Experimental observation of a superfluid gyroscope in a dilute Bose-Einstein condensate. *Phys. Rev. Lett.*, 91:090403, August 2003.

[94] M. Inguscio, S. Stringari, and C. E. Wieman, editors. *Bose-Einstein Condensation in Atomic Gases*. IOS Press, Amsterdam, 1999.

[95] S. Inouye, M. R. Andrews, J. Stenger, H.-J. Miesner, D. M. Stamper-Kurn, and W. Ketterle. Observations of Feshbach resonances in a Bose-Einstein condensate. *Nature*, 392:151–154, March 1998.

[96] S. Inouye, S. Gupta, T. Rosenband, A. P. Chikkatur, A. Görlitz, T. L. Gustavson, A. E. Leanhardt, D. E. Pritchard, and W. Ketterle. Observation of vortex phase singularities in Bose-Einstein condensates. *Phys. Rev. Lett.*, 87:080402, August 2001.

[97] T. Isoshima and K. Machida. Axisymmetric vortices in spinor Bose-Einstein condensates under rotation. *Phys. Rev. A*, 66:023602, August 2002.

[98] T. Isoshima, M. Nakahara, T. Ohmi, and K. Machida. Creation of a persistent current and vortex in a Bose-Einstein condensate of alkali-metal atoms. *Phys. Rev. A*, 61:063610, June 2000.

[99] J. D. Jackson. *Classical Electrodynamics*. Wiley, New York, 3^{rd} edition, 1999.

[100] J. Javanainen and M. Wilkens. Phase and phase diffusion of a split Bose-Einstein condensate. *Phys. Rev. Lett.*, 78:4675–4678, June 1997.

[101] M. P. A. Jones, C. J. Vale, D. Sahagun, B. V. Hall, C. C. Eberlein, B. E. Sauer, K. Furusawa, D. Richardson, and E. A. Hinds. Cold atoms probe the magnetic field near a wire. *arXiv:cond-mat/0308434*, August 2003.

[102] M. P. A. Jones, C. J. Vale, D. Sahagun, B. V. Hall, and E. A. Hinds. Spin coupling between cold atoms and the thermal fluctuations of a metal surface. *Phys. Rev. Lett.*, 91:080401, August 2003.

[103] P. Kapitza. Viscosity of liquid helium below the λ-point. *Nature*, 141:74, January 1938.

[104] K. Kasamatsu, M. Tsubota, and M. Ueda. Vortex phase diagram in rotating two-component Bose-Einstein condensates. *arXiv:cond-mat/0303125*, May 2003.

[105] M. Kasevich and S. Chu. Atomic interferometry using stimulated raman transitions. *Phys. Rev. Lett.*, 67:181–184, July 1991.

[106] M. Kasevich and S. Chu. Laser cooling below a photon recoil with three-level atoms. *Phys. Rev. Lett.*, 69:1741–1744, September 1992.

[107] M. A. Kasevich. Coherence with atoms. *Science*, 298:1363–1368, November 2002.

[108] A. Kastberg, W. D. Phillips, S. L. Rolston, and R. J. C. Spreeuw. Adiabatic cooling of cesium to 700 nK in an optical lattice. *Phys. Rev. Lett.*, 74:1542–1545, February 1995.

[109] D. W. Keith, C. R. Ekstrom, Q. A. Turchette, and D. E. Pritchard. An interferometer for atoms. *Phys. Rev. Lett.*, 66:2693–2696, May 1991.

[110] W. Ketterle. Nobel lecture: When atoms behave as waves: Bose-Einstein condensation and the atom laser. *Rev. Mod. Phys.*, 74:1131–1151, October 2002.

[111] W. Ketterle, K. B. Davis, M. A. Joffe, A. Martin, and D. E. Pritchard. High densities of cold atoms in a *dark* spontaneous-force optical trap. *Phys. Rev. Lett.*, 70:2253–2256, April 1991.

[112] W. Ketterle, D. S. Durfee, and D. M. Stamper-Kurn. Making, probing and understanding Bose-Einstein condensates. In Inguscio et al. [94], pages 67–176.

[113] W. Ketterle and H.-J. Miesner. Coherence properties of Bose-Einstein condensates and atom lasers. *Phys. Rev. A*, 56:3291–3293, October 1997.

[114] U. A. Khawaja and H. Stoof. Skyrmions in a ferromagnetic Bose-Einstein condensate. *Nature*, 411:918–920, June 2001.

[115] U. A. Khawaja and H. T. C. Stoof. Skyrmion physics in Bose-Einstein ferromagnets. *Phys. Rev. A*, 64:043612, October 2001.

[116] T. Kita, T. Mizushima, and K. Machida. Spinor Bose-Einstein condensates with many vortices. *Phys. Rev. A*, 66:061601(R), December 2002.

[117] N. N. Klausen, J. L. Bohn, and C. H. Greene. Nature of spinor Bose-Einstein condensates in rubidium. *Phys. Rev. A*, 64:053602, November 2001.

[118] J. M. Kosterlitz. The critical properties of the two-dimensional xy model. *J. Phys. C: Solid State Phys.*, 7:1046–1060, 1974.

[119] J. M. Kosterlitz and D. J. Thouless. Long range order and metastability in two dimensional solids and superfluids. *J. Phys. C: Solid State Phys.*, 5:L124–L126, 1972.

[120] J. M. Kosterlitz and D. J. Thouless. Ordering, metastability and phase transitions in two-dimensional systems. *J. Phys. C: Solid State Phys.*, 6:1181–1203, 1973.

[121] S. Kraft, A. Günther, H. Ott, D. Wharam, C. Zimmermann, and J. Fortágh. Anomalous longitudinal magnetic field near the surface of copper conductors. *J. Phys. B: At. Mol. Opt. Phys.*, 35:L469–L474, November 2002.

[122] A. E. Leanhardt, A. P. Chikkatur, D. Kielpinski, Y. Shin, T. L. Gustavson, W. Ketterle, and D. E. Pritchard. Propagation of Bose-Einstein condensates in a magnetic waveguide. *Phys. Rev. Lett.*, 89:040401, July 2002.

[123] A. E. Leanhardt, A. Görlitz, A. P. Chikkatur, D. Kielpinski, Y. Shin, D. E. Pritchard, and W. Ketterle. Imprinting vortices in a Bose-Einstein condensate using topological phases. *Phys. Rev. Lett.*, 89:190403, November 2002.

[124] A. E. Leanhardt, T. A. Pasquini, M. Saba, A. Schirotzek, Y. Shin, D. Kielpinski, D. E. Pritchard, and W. Ketterle. Cooling Bose-Einstein condensates below 500 picokelvin. *Science in press*, 2003.

[125] A. E. Leanhardt, Y. Shin, A. P. Chikkatur, D. Kielpinski, W. Ketterle, and D. E. Pritchard. Bose-Einstein condensates near a microfabricated surface. *Phys. Rev. Lett.*, 90:100404, March 2003.

[126] A. E. Leanhardt, Y. Shin, D. Kielpinski, D. E. Pritchard, and W. Ketterle. Coreless vortex formation in a spinor Bose-Einstein condensate. *Phys. Rev. Lett.*, 90:140403, April 2003.

[127] D.-H. Lee and C. L. Kane. Boson-vortex-skyrmion duality, spin singlet fractional quantum hall effect, and spin-$\frac{1}{2}$ anyon superconductivity. *Phys. Rev. Lett.*, 64:1313–1317, March 1990.

[128] A. J. Leggett. Bose-Einstein condensation in the alkali gases: Some fundamental concepts. *Rev. Mod. Phys.*, 73:307–356, April 2001.

[129] A. Lenef, T. D. Hammond, E. T. Smith, M. S. Chapman, R. A. Rubenstein, and D. E. Pritchard. Rotation sensing with an atom interferometer. *Phys. Rev. Lett.*, 78:760–763, February 1997.

[130] U. Leonhardt and G. E. Volovik. How to create an alice string (half-quantum vortex) in a vector Bose-Einstein condensate. *JETP Lett.*, 72:46–48, July 2000.

[131] M. Lewenstein and L. You. Quantum phase diffusion of a Bose-Einstein condensate. *Phys. Rev. Lett.*, 77:3489–3493, October 1996.

[132] Y.-J. Lin, I. Teper, C. Chin, and V. Vuletic. Impact of Casimir-Polder potential on Johnson noise on Bose-Einstein condensate stability near surfaces. *arXiv:cond-mat/0308457*, August 2003.

[133] F. London. The λ-phenomenon of liquid helium and the Bose-Einstein degeneracy. *Nature*, 141:643–644, April 1938.

[134] F. London. On the Bose-Einstein condensation. *Phys. Rev.*, 54:947–954, December 1938.

[135] E. Lundh, C. J. Pethick, and H. Smith. Vortices in Bose-Einstein-condensed atomic clouds. *Phys. Rev. A*, 58:4816, December 1998.

[136] H. Mabuchi and A. C. Doherty. Cavity quantum electrodynamics: Coherence in context. *Science*, 298:1372–1377, November 2002.

[137] K. W. Madison, F. Chevy, W. Wohlleben, and J. Dalibard. Vortex formation in a stirred Bose-Einstein condensate. *Phys. Rev. Lett.*, 84:806–809, January 2000.

[138] O. Mandel, M. Greiner, A. Widera, T. Rom, T. W. Hänsch, and I. Bloch. Coherent transport of neutral atoms in spin-dependent optical lattice potentials. *Phys. Rev. Lett.*, 91:010407, July 2003.

[139] J.-P. Martikainen, A. Collin, and K.-A. Suominen. Coreless vortex ground state of the rotating spinor condensate. *Phys. Rev. A*, 66:053604, November 2002.

[140] K.-P. Marzlin, W. Zhang, and B. C. Sanders. Creation of skyrmions in a spinor Bose-Einstein condensate. *Phys. Rev. A*, 62:013602, July 2000.

[141] M. R. Matthews, B. P. Anderson, P. C. Haljan, D. S. Hall, C. E. Wieman, and E. A. Cornell. Vortices in a Bose-Einstein condensate. *Phys. Rev. Lett.*, 83:2498–2501, September 1999.

[142] J. J. McClelland, R. E. Scholten, E. C. Palm, and R. J. Celotta. Laser-focused atomic deposition. *Science*, 262:877–880, November 1993.

[143] C. Menotti, J. R. Anglin, J. I. Cirac, and P. Zoller. Dynamic splitting of a Bose-Einstein condensate. *Phys. Rev. A*, 63:023601, February 2001.

[144] N. D. Mermin. The topological theory of defects in ordered media. *Rev. Mod. Phys.*, 51:591–648, July 1979.

[145] N. D. Mermin and T.-L. Ho. Circulation and angular momentum in the A phase of superfluid helium-3*. *Phys. Rev. Lett.*, 36:594–597, March 1976.

[146] H. J. Metcalf and P. van der Straten. *Laser Cooling and Trapping*. Springer-Verlag, New York, 1999.

[147] M.-O. Mewes, M. R. Andrews, N. J. van Druten, D. M. Kurn, D. S. Durfee, and W. Ketterle. Bose-Einstin condensation in a tightly confining dc magnetic trap. *Phys. Rev. Lett.*, 77:416–419, July 1996.

[148] A. L. Migdall, J. V. Prodan, W. D. Phillips, T. H. Bergeman, and H. J. Metcalf. First observation of magnetically trapped neutral atoms. *Phys. Rev. Lett.*, 54:2596–2599, June 1985.

[149] T. Mizushima, K. Machida, and T. Kita. Axisymmetric versus nonaxisymmetric vortices in spinor Bose-Einstein condensates. *Phys. Rev. A*, 66:053610, November 2002.

[150] T. Mizushima, K. Machida, and T. Kita. Mermin-Ho vortex in ferromagnetic spinor Bose-Einstein condensates. *Phys. Rev. Lett.*, 89:030401, July 2002.

[151] G. Modugno, G. Ferrari, G. Roati, R. J. Brecha, A. Simoni, and M. Inguscio. Bose-Einstein condensation of potassium atoms by sympathetic cooling. *Science*, 294:1320–1322, November 2001.

[152] M. Möttönen, N. Matsumoto, M. Nakahara, and T. Ohmi. Continuous creation of a vortex in a Bose-Einstein condensate with hyperfine spin $F = 2$. *J. Phys.: Condens. Matter*, 14:13481–13491, December 2002.

[153] M. Möttönen, T. Mizushima, T. Isoshima, M. M. Salomaa, and K. Machida. Splitting of a doubly quantized vortex through intertwining in Bose-Einstein condensates. *Phys. Rev. A*, 68:023611, August 2003.

[154] D. Müller, D. Z. Anderson, R. J. Grow, P. D. D. Schwindt, and E. A. Cornell. Guiding neutral atoms around curves with lithographically patterned current-carrying wires. *Phys. Rev. Lett.*, 83:5194–5197, December 1999.

[155] D. Müller, E. A. Cornell, M. Prevedelli, P. D. D. Schwindi, Y.-J. Wang, and D. Z. Anderson. Magnetic switch for integrated atom optics. *Phys. Rev. A*, 63:041602(R), April 2001.

[156] D. Müller, E. A. Cornell, M. Prevedelli, P. D. D. Schwindt, A. Zozulya, and D. Z. Anderson. Waveguide atom beam splitter for laser-cooled neutral atoms. *Opt. Lett.*, 25:1382–1384, September 2000.

[157] M. Nakahara, T. Isoshima, K. Machida, S.-I. Ogawa, and T. Ohmi. A simple method to create a vortex in a Bose-Einstein condensate of alkali atoms. *Physica B*, 284-288:17–18, July 2000.

[158] P. Nozières and D. Pines. *The Theory of Quantum Liquids*, volume II. Addison-Wesley, Reading, MA, 1990.

[159] S.-I. Ogawa, M. Möttönen, M. Nakahara, T. Ohmi, and H. Shimada. Method to create a vortex in a Bose-Einstein condensate. *Phys. Rev. A*, 66:013617, July 2002.

[160] T. Ohmi and K. Machida. Bose-Einstein condensation with internal degrees of freedom in alkali atom gases. *J. Phys. Soc. Jpn*, 67:1822–1825, June 1998.

[161] A. S. Oja and O. V. Lounasmaa. Nuclear magnetic ordering in simple metals at positive and negative nanokelvin temperatures. *Rev. Mod. Phys.*, 69:1–136, January 1997.

[162] M. Olshanii. Atomic scattering in the presence of an external confinement and a gas of impenetrable Bosons. *Phys. Rev. Lett.*, 81:938–941, August 1998.

[163] R. Onofrio, C. Raman, J. M. Vogels, J. R. Abo-Shaeer, A. P. Chikkatur, and W. Ketterle. Observation of superfluid flow in a Bose-Einstein condensed gas. *Phys. Rev. Lett.*, 85:2228–2231, September 2000.

[164] C. Orzel, A. K. Tuchman, M. L. Fenselau, M. Yasuda, and M. A. Kasevich. Squeezed states in a Bose-Einstein condensate. *Science*, 291:2386–2389, March 2001.

[165] H. Ott, J. Fortagh, G. Schlotterbeck, A. Grossmann, and C. Zimmermann. Bose-Einstein condensation in a surface microtrap. *Phys. Rev. Lett.*, 87:230401, December 2001.

[166] A. S. Parkins and D. F. Walls. The physics of trapped dilute-gas Bose-Einstein condensates. *Phys. Rep.*, 303:1–80, 1997.

[167] F. Pereira Dos Santos, J. Léonard, J. Wang, C. J. Barrelet, F. Perales, E. Rasel, C. S. Unnikrishnin, M. Leduc, and C. Cohen-Tannoudji. Bose-Einstein condensation of metastable helium. *Phys. Rev. Lett.*, 86:3459–3462, April 2001.

[168] A. Peters, K. Y. Chung, B. Young, J. Hensley, and S. Chu. Precision atom interferometry. *Phil. Trans. R. Soc. Lond. A*, 355:2223–2233, 1997.

[169] C. J. Pethick and H. Smith. *Bose-Einstein Condensation in Dilute Gases*. Cambridge University Press, New York, 2002.

[170] D. S. Petrov, M. Holzmann, and G. V. Shlyapnikov. Bose-Einstein condensation in quasi-2D trapped gases. *Phys. Rev. Lett.*, 84:2551–2555, March 2000.

[171] D. S. Petrov, G. V. Shlyapnikov, and J. T. M. Walraven. Regimes of quantum degeneracy in trapped 1D gases. *Phys. Rev. Lett.*, 85:3745–3749, October 2000.

[172] W. D. Phillips. Laser cooling and trapping of neutral atoms. *Rev. Mod. Phys.*, 70:721–741, July 1998.

[173] L. Plaja and L. Santos. Expansion of a Bose-Einstein condensate in an atomic waveguide. *Phys. Rev. A*, 65:035602, March 2002.

[174] D. E. Pritchard. Cooling neutral atoms in a magnetic trap for precision spectroscopy. *Phys. Rev. Lett.*, 51:1336–1339, October 1983.

[175] N. Prokof'ev, O. Ruebenacker, and B. Svistunov. Critical point of a weakly interaction two-dimensional Bose gas. *Phys. Rev. Lett.*, 87:270402, December 2001.

[176] H. Pu, S. Raghavan, and N. P. Bigelow. Creation of topological states in spinor condensates. *Phys. Rev. A.*, 63:063603, June 2001.

[177] E. L. Raab, M. Prentiss, A. Cable, S. Chu, and D. E. Pritchard. Trapping of neutral sodium atoms with radiation pressure. *Phys. Rev. Lett.*, 59:2631–2634, December 1987.

[178] C. Raman, M. Köhl, R. Onofrio, D. S. Durfee, C. E. Kuklewicz, Z. Hadzibabic, and W. Ketterle. Evidence for a critical velocity in a Bose-Einstein condensed gas. *Phys. Rev. Lett.*, 83:2502–2505, September 1999.

[179] J. Reichel, F. Bardou, M. Ben Dahan, E. Peik, S. Rand, C. Salomn, and C. Cohen-Tannoudji. Raman cooling of cesium below 3 nK: New approach inspired by Lévy flight statistics. *Phys. Rev. Lett.*, 75:4575–4578, December 1995.

[180] J. Reichel, W. Hänsel, and T. W. Hänsch. Atomic micromanipulation with magnetic surface traps. *Phys. Rev. Lett.*, 83:3398–3401, October 1999.

[181] S. Richard, F. Gerbier, J. H. Thywissen, M. Hugbart, P. Bouyer, and A. Aspect. Momentum spectroscopy of 1D phase fluctuations in Bose-Einstein condensates. *Phys. Rev. Lett.*, 91:010405, July 2003.

[182] A. Robert, O. Sirjean, A. Browaeys, J. Poupard, S. Nowak, D. Boiron, C. I. Westbrook, and A. Aspect. A Bose-Einstein condensate of metastable atoms. *Science*, 292:461–464, April 2001.

[183] A. Röhrl, M. Naraschewski, A. Schenzle, and H. Wallis. Transition for phase locking to the interference of independent Bose condensates: Theory versus experiment. *Phys. Rev. Lett.*, 78:4143–4146, June 1997.

[184] D. S. Rokhsar. Vortex stability and persistent currents in trapped Bose gases. *Phys. Rev. Lett.*, 79:2164–2167, September 1997.

[185] J. R. Rubbmark, M. M. Kash, M. G. Littman, and D. Kleppner. Dynamical effects at avoided level crossings: A study of the Landau-Zener effect using Rydberg atoms. *Phys. Rev. A*, 23:3107–3117, June 1981.

[186] J. Ruostekoski. Topological phase preparation in a pair of atomic Bose-Einstein condensates. *Phys. Rev. A*, 61:041603(R), April 2000.

[187] J. Ruostekoski and J. R. Anglin. Creating vortex rings and three-dimensional skyrmions in Bose-Einstein condensates. *Phys. Rev. Lett.*, 86:3934, April 2001.

[188] A. I. Safonov, S. A. Vasilyev, I. S. Yasnikov, I. I. Lukashevich, and S. Jaakkola. Observation of quasicondensate in two-dimensional atomic hydrogen. *Phys. Rev. Lett.*, 81:4545–4548, November 1998.

[189] H. Saito and M. Ueda. Split instability of a vortex in an attractive Bose-Einstein condensate. *Phys. Rev. Lett.*, 89:190402, November 2002.

[190] H. Saito and M. Ueda. Split-merge cycle, fragmented collapse, and vortex disintegration in rotating Bose-Einstein condensates with attractive interactions. *arXiv:cond-mat/0306319*, June 2003.

[191] B. Saubaméa, T. W. Hijmans, S. Kulin, E. Rasel, E. Peik, M. Leduc, and C. Cohen-Tannoudji. Direct measurement of the spatial correlation function of ultracold atoms. *Phys. Rev. Lett.*, 79:3146–3149, October 1997.

[192] C. M. Savage and J. Ruostekoski. Energetically stable particlelike skrymions in a trapped Bose-Einstein condensate. *Phys. Rev. Lett.*, 91:010403, July 2003.

[193] H. Schmaljohann, M. Erhard, J. Kronjäger, M. Kottke, S. van Staa, J. J. Arlt, K. Bongs, and K. Sengstock. Dynamics of $F = 2$ spinor Bose-Einstein condensates. *arXiv:cond-mat/0308281*, August 2003.

[194] J. Schmiedmayer. Quantum wires and quantum dots for neutral atoms. *Euro. Phys. J. D*, 4:57–62, October 1998.

[195] A. Schneider, A. Kasper, Ch. vom Hagen, M. Bartenstein, B. Engeser, T. Schumm, I. Bar-Joseph, R. Folman, L. Feenstra, and J. Schmiedmayer. Bose-Einstein condensation in a simple microtrap. *Phys. Rev. A*, 67:023612, Feburary 2003.

[196] F. Schreck, L. Khaykovich, K. L. Corwin, G. Ferrari, T. Bourdel, J. Cubizolles, and C. Salomon. Quasipure Bose-Einstein condensate immersed in a Fermi sea. *Phys. Rev. Lett.*, 87:080403, August 2001.

[197] K. Schwab, N. Bruckner, and R. E. Packard. Detection of the Earth's rotation using superfluid phase coherence. *Nature*, 386:585–587, April 1997.

[198] F. Shimizu. Specular reflection of very slow metastable neon atoms from a solid surface. *Phys. Rev. Lett.*, 86:987–990, Feburary 2001.

[199] Y. Shin, M. Saba, T. A. Pasquini, W. Ketterle, D. E. Pritchard, and A. E. Leanhardt. Atom interferometry with Bose-Einstein condensates in a double-well potential. *arXiv:cond-mat/0306305*, July 2003.

[200] T. H. R. Skyrme. A non-linear field theory. *Proc. R. Soc. London A*, 260:127–138, February 1961.

[201] A. Smerzi, S. Fantoni, S. Giovanazzi, and S. R. Shenoy. Quantum coherent atomic tunneling between two trapped Bose-Einstein condensates. *Phys. Rev. Lett.*, 79:4950–4953, December 1997.

[202] D. M. Stamper-Kurn, M. R. Andrews, A. P. Chikkatur, S. Inouye, H.-J. Miesner, J. Stenger, and W. Ketterle. Optical confinement of a Bose-Einstin condensate. *Phys. Rev. Lett.*, 80:2027–2030, March 1998.

[203] J. Stenger, S. Inouye, A. P. Chikkatur, D. M. Stamper-Kurn, D. E. Pritchard, and W. Ketterle. Bragg spectroscopy of a Bose-Einstein condensate. *Phys. Rev. Lett.*, 82:4569–4573, June 1999.

[204] J. Stenger, S. Inouye, D. M. Stamper-Kurn, H.-J. Miesner, A. P. Chikkatur, and W. Ketterle. Spin domains in ground-state Bose-Einstein condensates. *Nature*, 396:345–348, November 1998.

[205] J. A. Stickney and A. A. Zozulya. Expansion of a Bose-Einstein condensate from a microtrap into a waveguide. *Phys. Rev. A*, 65:053612, May 2002.

[206] J. A. Stickney and A. A. Zozulya. Wave-function recombination instability in cold-atom interferometers. *Phys. Rev. A*, 66:053601, November 2002.

[207] Y. Takasu, K. Maki, K. Komori, T. Takano, K. Honda, M. Kumakura, T. Yabuzaki, and Y. Takahashi. Spin-singlet Bose-Einstein condensation of two-electron atoms. *Phys. Rev. Lett.*, 91:040404, July 2003.

[208] J. H. Thywissen, M. Olshanii, G. Zabow, M. Drndić, K. S. Johnson, R. M. Westervelt, and M. Prentiss. Microfabricated magnetic waveguides for neutral atoms. *Euro. Phys. J. D*, 7:361–367, October-November 1999.

[209] G. Timp, R. E. Behringer, D. M. Tennant, J. E. Cunningham, M. Prentiss, and K. K. Berggren. Using light as a lens for submicron, neutral-atom lithography. *Phys. Rev. Lett.*, 69:1636–1639, September 1992.

[210] L. Tisza. Transport phenomena in helium II. *Nature*, 141:913, May 1938.

[211] L. Tonks. The complete equation of state of one, two and three-dimensional gases of hard elastic spheres. *Phys. Rev.*, 50:955–963, December 1936.

[212] P. Treutlein, K. Y. Chung, and S. Chu. High-brightness source for atomic fountains. *Phys. Rev. A*, 63:051401(R), May 2001.

[213] A. G. Truscott, K. E. Strecker, W. I. McAlexander, G. B. Partridge, and R. G. Hulet. Observation of Fermi pressure in a gas of trapped atoms. *Science*, 291:2570–2572, March 2001.

[214] E. Tsikata. *The Characterization of Bose-Einstein Condensates on an Atom Chip.* B.S. Thesis, Massachusetts Institute of Technology, May 2002.

[215] J. M. Vogels, K. Xu, and W. Ketterle. Generation of macroscopic pair-correlated atomic beams by four-wave mixing in Bose-Einstein condensates. *Phys. Rev. Lett.*, 89:020401, July 2002.

[216] D.-W. Wang, M. D. Lukin, and E. Demler. Disordered Bose-Einstein condensates in quasi one-dimensional magnetic microtraps. *arXiv:cond-mat/0307402*, July 2003.

[217] T. Weber, J. Herbig, M. Mark, H.-C. Nägerl, and R. Grimm. Bose-Einstein condensation of cesium. *Science*, 299:232–235, January 2003.

[218] J. D. Weinstein and K. G. Libbrecht. Microscopic magnetic traps for neutral atoms. *Phys. Rev. A*, 52:4004–4009, November 1995.

[219] D. S. Weiss, B. C. Young, and S. Chu. Precision measurement of the photon recoil of an atom using atomic interferometry. *Phys. Rev. Lett.*, 70:2706–2709, May 1993.

[220] J. E. Williams. Optimal conditions for observing Josephson oscillations in a double-well Bose-Einstein condensate. *Phys. Rev. A*, 64:013610, July 2001.

[221] J. E. Williams and M. J. Holland. Preparing topological states of a Bose-Einstein condensate. *Nature*, 401:568–572, October 1999.

[222] H. M. Wiseman and J. A. Vaccaro. Atom lasers, coherent states, and coherence. I. Physically realizable ensembles of pure states. *Phys. Rev. A*, 65:043605, April 2002.

[223] H. M. Wiseman and J. A. Vaccaro. Atom lasers, coherent states, and coherence. II. Physically realizable ensembles of pure states. *Phys. Rev. A*, 65:043606, April 2002.

[224] E. J. Yarmchuk, M. J. V. Gordon, and R. E. Packard. Observation of stationary vortex arrays in rotating superfluid helium. *Phys. Rev. Lett.*, 43:214–217, July 1979.

[225] S.-K. Yip. Internal vortex structure of a trapped spinor Bose-Einstein condensate. *Phys. Rev. Lett.*, 83:4677–4681, December 1999.

[226] F. Zambelli and S. Stringari. Quantized vortices and collective oscillations of a trapped Bose-Einstein condensate. *Phys. Rev. Lett.*, 81:1754–1757, August 1998.

[227] H. Zhai, W. Chen, Z. Xu, and L. Chang. Skyrmion excitation in two-dimensional spinor Bose-Einstein condensate. *arXiv:cond-mat/0210397*, October 2002.

[228] Y. Zhang, W.-D. Li, L. Li, and H. J. W. Müller-Kirsten. Exact calculation of the skyrmion lifetime in a ferromagnetic Bose-Einstein condensate. *Phys. Rev. A*, 66:043622, October 2002.